Doctoral Dissertation

Study of Label-Free Cell Imaging Using Photonic Crystal Nanolaser Array

(フォトニック結晶ナノレーザアレイを用いた

細胞のラベルフリーイメージング)

Hiroshi Abe

阿部 紘士

Yokohama National University

Department of Physics, Electrical and Computer Engineering

March, 2016

要約

　高齢化社会を迎え，医療の高度化が進んでいる．なかでも癌・アルツハイマー治療，iPS 細胞等の再生医療には細胞観察技術の高度化が重要な課題となっている．現在広く用いられる蛍光顕微観察法では，細胞に標識を修飾する必要があり，その手間が問題となっている．標識を用いない方法では顕微ラマン分光法と表面プラズモン共鳴法があるが，それぞれ信号が微弱で不安定，空間分解能が低いなどの課題がある．この解決に向けて本研究では，半導体薄膜に空孔を配列させたフォトニック結晶ナノレーザを用いた屈折率センシングに着目した．光励起で動作するこのナノレーザは，周囲の屈折率と共に発振波長を変化させるので，波長を読み取ることで屈折率センサとして機能する．1 μm^2 以下という微小面積に対して，屈折率分解能 10^{-5} 以下という高性能が得られている．つまりこのナノレーザを二次元集積し，その上に定着した細胞の屈折率分布をセンシングすることで個々のナノレーザが細胞の一部の屈折率を反映して発振波長が変化する．つまりナノレーザアレイの発振波長を観測するだけで定着している細胞の挙動を観察することが可能になる．ここでは標識の修飾が不要であり，高い空間分解能とレーザ光の直接検出による安定した信号強度をもつ細胞観察能力が得られる．従来の観察法では得られないわずかな変化が観察できるので，医療診断，細胞機構の解明など広い応用が期待できる．本研究では，フォトニック結晶ナノレーザアレイを使用した新しい細胞観察技術の実証を目指し，デバイスや観測システムの開発，性能の検証，改善の段階を経て，実際に細胞を観察した．

　デバイスの準備では，GaInAsP の量子井戸を含むウエハーを加工し，フォトニック結晶ナノレーザアレイを製作した．具体的には，電子線リソグラフィー，誘導結合プラズマエッチングでパターンを量子井戸に転写，不要な層を除去することでフォトニック結晶スラブを形成した．従来のエアブリッジ構造では器械的な脆弱性から面積が 25 μm 角に制限されていた．本研究では，スラブ構造をガラス母材に貼り付けるプロセスを開発することで，この課題を解決し，ヒト細胞の全体を観察可能な 100 μm 角の観測範囲をもつデバイスを製作した．また，ナノレーザ間の結合がナノレーザのイメージングピクセルとしての機能を阻害していた．そこで，初期的に製作したナノレーザアレイにおいて結合の有無や構造パラメータについて詳細に比較した．その結果，フォトニック結晶の円孔径により，共振モードが制御できること，さらにこの共振モードによってナノレーザ間の結合を抑制できることを発見した．またナノレーザの測定では，励起光の集光スポットを走査することで，各ナノレーザを選択的に励起して個別の特性を確認していたが，隣接するナノレーザを同時に励起してしまった場合の信号の混線が問題になって

いた．そこで，H0 共振器を形成するシフト円孔の直径を変化させることで，90 nm の帯域で単調に発振波長が変化することを示し，ナノレーザの発振波長を詳細に制御する方法を開発した．これにより，予め個々のナノレーザの発振波長を把握しておくことで，スペクトルから個々のナノレーザを識別することが可能となった．さらに，このような波長が異なるナノレーザアレイでは，複数のナノレーザを一括に励起し，それぞれの波長を識別することで，イメージングのフレームレートを改善する応用が考えられる．しかし，製作誤差により，上記の設計での波長制御だけでは，完全な識別には至らなかった．そこで，ナノレーザアレイを希塩酸中に浸漬させ，励起光を照射することで選択的にナノレーザの発振波長を変化させるポスト波長トリミングプロセスを開発した．これにより 9 個のナノレーザアレイの発振波長を 2.5 nm 間隔に整列させることに成功した．この数値は経験的な細胞による波長シフトよりも大きい値であり，細胞実験中の波長識別が可能となった．このナノレーザアレイでのフレームレートは~ second / frame とリアルタイム観測に近い速度まで改善された．さらにパルス励起におけるスペクトルの揺らぎの低減に向けて，貼り付け構造において共振器にナノスロット構造を導入したナノスロットナノレーザアレイを製作した．

製作したデバイスの発振特性，センシング特性，イメージング特性を確認した．発振特性の確認では，ナノレーザアレイを水に浸漬し，波長 0.98 mm の励起光を対物レンズで集光して，光励起させ，発振光をスペクトルアナライザーまたは分光器とアレイフォトディテクターで観測した．その結果，$21 \times 21 = 441$ 個集積した通常のナノレーザアレイにおいてアレイ中で発振歩留まり 100%を確認した．また $12 \times 12 = 144$ 個集積したナノスロットナノレーザアレイにおいてもアレイ中で発振歩留まり 100%を確認した．センシング特性の確認では，デバイスを濃度の異なる砂糖水に浸漬させ，各濃度での発振波長と屈折率計での測定値の傾きから，ナノレーザアレイの感度を観測した．通常のナノレーザでの感度は平均 57 nm / RIU，ナノスロットナノレーザでは，97 nm / RIU の傾きで屈折率の変化を波長の変化でセンシングしていた．またここで，感度をアレイデバイスのナノレーザ毎に測定することで，屈折率イメージングにおける，デバイスの感度ばらつきの補正を可能にした．この条件で測定される屈折率の絶対精度を求めたところ，通常のナノレーザで~10^{-2} RIU，ナノスロットナノレーザでは 2.0×10^{-3} RIU とナノスロット構造の導入により分解能を改善した．イメージング特性の確認では，デバイスにレジストを滴下して発振波長を測定し，レジストを洗浄除去してから再度発振波長を測定して，波長の変化をナノレーザの位置に対応させてマッピングし，得られた波長シフトイメージと光学顕微鏡像を比較した．すると波長シフトイメージでの境界と光学顕微鏡像でのレジストパターンの境界が一致し，イメージング特性が実証された．また，これらの大規模化されたナノレーザアレイでの測定，データ処理に要する作業量が膨大になったので，自動処理システムを構築した．具体的には，励起・受光に用いている顕微鏡システムのステージ座標をピエゾアクチュエータで制御し，分光・受光装置の動作を

通信制御し，光軸調整，測定，データ保存の一連の実験シーケンスをプログラムで自動化した．またスペクトルデータから，個々のナノレーザの波長データとその時間変化の導関数を用いて，発振波長を識別，ナノレーザの位置に対応した行列データにまとめるデータ処理を自動化した．

　上記で開発したデバイスやシフテムを実際に細胞イメージングに応用した．実験の手順では，まずナノレーザアレイデバイスを準備し，表面状態を親水化処理，殺菌処理で整えた後，HeLa 細胞を含んだ培養液に浸漬し，インキュベータ中で半日培養することでナノレーザアレイの表面に細胞を定着した．続いて，細胞が定着したナノレーザアレイを PDMS で製作した流路中に固定することで，培養液環境のままで測定系に設置した．ここで必要であれば，ナノレーザアレイの個々の発振波長と座標を詳細な光軸調整を伴うプログラムで測定した．続いて，全てのナノレーザアレイの発振波長を繰り返し測定し，特に細胞の試薬反応を観測する実験では，繰り返し測定の途中で試薬を含んだ培養液に交換して反応を促した．その後，トリプシンを用いてナノレーザアレイから細胞を剥離させ，細胞が定着していない状態の発振波長を測定した．この細胞が無い状態を基準に波長シフトを計算しマッピングすることでイメージを形成，繰り返し測定での連続イメージにより動画化した．得られた波長シフトイメージや連続イメージでは，細胞による屈折率の上昇がレッドシフトとして観測された．ここから提案する手法での細胞観測を実証した．レッドシフトの形状は細胞の光学顕微鏡像での形状と一致するものもあれば一致しないものもあった．これらは，細胞の屈折率だけでなく，細胞の定着状態を反映したためと考えられる．ナノスロットナノレーザを使用した測定では，屈折率変化イメージングを実証した．~10^{-4} RIU の屈折率分解能では，屈折率変化の時間振動が観測され，この振動の頻度が細胞の状態を反映している結果が得られた．また細胞の試薬反応の高フレームレート観測では，アクチノマイシン D という細胞核に選択的に結合する試薬に対して，試薬反応と見られる屈折率の上昇が，~2 second / frame と動的な状態変化として観測された．これらは高い屈折率分解能などを要するために通常の光学顕微鏡では観測できない状態変化であり，提案する観測法でしか観測できない情報であると言える．

　以上の研究により，ラベルフリー，高空間分解能，高強度信号，潜在的に~10^{-5} RIU の屈折率分解能をもつ新しい細胞イメージング手法を提案，実証した．しかし，現状の屈折率分解能は~2×10^{-3} RIU に制限されており，この解消には共振器構造によるレーザモードのさらなる調整や材料的な TO 効果の影響の抑制が必要である．また集積規模や空間分解能でも改良の余地はある．今後，提案した細胞観察手法による細胞イメージング技術への貢献が期待される．

Contents

vi

Chapter 1
Introduction

1. 1 Cell imaging

Cell imaging techniques are used in life sciences, medical diagnosis, and drug development. In the field of cellular biology, cell imaging is a vital tool, for example, in the diagnosis of cancers. Furthermore, cell-based screening has appeared as a new tool for drug development. With increased population aging, the development of advanced medical techniques is in demand; in particular, for the treatment of cancers and Alzheimer's and regenerative medicine using induced pluripotent stem (iPS) cells, advanced cell imaging techniques for future bioscience applications are anticipated. Cell imaging began with optical microscopy in 1665 [1-1] and has since evolved, with the miniaturization of intracellular observation targets. Moreover, electronic microscopy [1-2] has enabled the imaging of biomolecules. Recently, an important target for advanced bioscience and medical diagnoses has been to obtain information about intracellular interactions such as biomolecule properties or protein reactions [1-3]. Unfortunately, electronic microscopy is not suitable for imaging living cells and the observation of such molecular-level behavior with simple optical microscopy is difficult because of the diffraction limit, which is ~200 nm in the visible light bandwidth, and the minute changes in transmittance and refractive index. Various techniques have been used to solve this issue, e.g., fluorescence microscopy [1-5, 6], Raman spectroscopy [1-7 − 11], surface plasmon resonance spectroscopy [1-12 − 20], diffraction grating spectroscopy [1-22 − 24], phase contrast microscopy, differential interference microscopy, and phase holographic microscopy [1-26 − 28]. Of these methods, fluorescence microscopy has been used extensively because of the ease of visualizing the behavior of arbitrary intracellular biomolecules and used in various applications. However, fluorescence microscopy has limitations as described below, and therefore, it might not be suitable for many future bioscience and medical applications.

1. 1. 1 **Methods with labels**

In the context of fluorescence microscopy, labeling methods are a widely used way of linking a label to an object. A fluorescence microscopy setup is shown in Fig. 1.1. Usually, fluorescence, quantum dots, radioisotopes, or quenchers are used as labels, bound to an arbitrary object by an antigen–antibody reaction, DNA hybridization, or cellular synthesis. The emission from a pumped label is identified by a wavelength filter and the near-field pattern from the label is used to visualize the distribution of the labeled object. The success of this method in identifying labels has been widely reported. In the medical diagnosis, labeling methods have been used, e.g. to distinguish between normal and cancer cells. Total internal reflective fluorescence improves the vertical observation resolution limited in the evanescent field to ~100 nm and stimulated emission depletion permits the observation of single fluorescent molecules [1-25]. However, labeling methods do have some limitations. The preparation of the binding labels, using techniques such as gene transfer, electroporation, fixing, and injection by a micropipette or liposome, requires significant expertise and time, which reduces the potential throughput of the methods. These labeling methods may be invasive to the cell. In particular, when using labeling methods, the functionality of an objective protein must not be inhibited by label binding: labeling sensitive objects like iPS cells is difficult because of this invasiveness. Furthermore, cell toxicity can be a problem and photobleaching and photocytotoxic properties must be considered. Furthermore, a quantitative diagnosis of the physical amount of the cell present is difficult because of the indetermination of the binding.
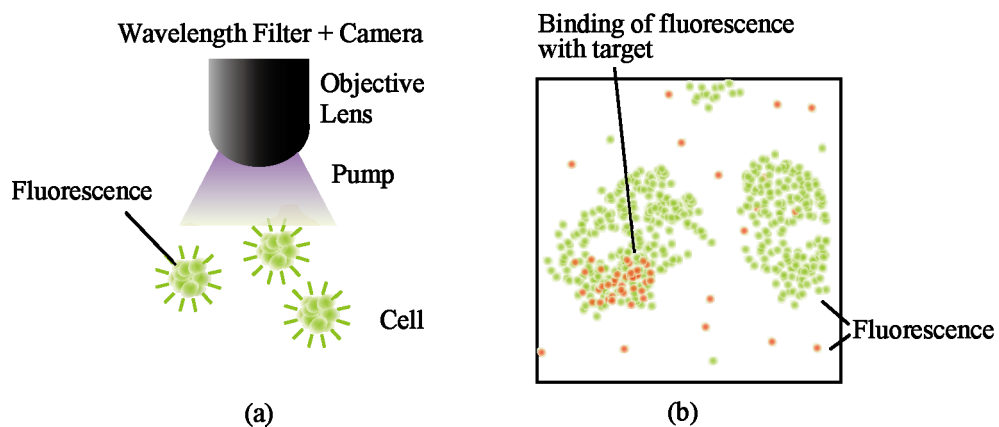
Fig. 1.1. Labeling method. (a) Schematic of fluorescence microscopy. (b) Schematic of the fluorescent image. Each label is binding to different target molecule..

1.1.2 **Label-free methods**

The problems of labeling methods described above can be solved with methods that do not use labels. These methods are described below.

Raman spectroscopy

Fig. 1.2(a) shows a schematic for Raman spectroscopy. Raman scattering is an inelastic scattering that has a different wavelength from that of the light incident on the material being tested. The difference in these wavelengths is called the Raman shift, and is equivalent to the energy between a specific molecular vibrational state and the ground state. Raman scattering can be categorized as Stokes Raman scattering or anti-Stokes Raman scattering. These are defined as a scattering with an energy absorbance or lose, respectively. The resultant image of the Raman shift corresponds to the distribution of the material. This method has a spatial resolution equal to that of an optical microscope and a high throughput, with no preparation requirements. However, the cross-section of Raman scattering is typically 14 orders of magnitude weaker than that of fluorescence [1-10]. This is a problem for phototoxicity. Techniques to inhibit this problem have been developed, such as stimulated Raman scattering
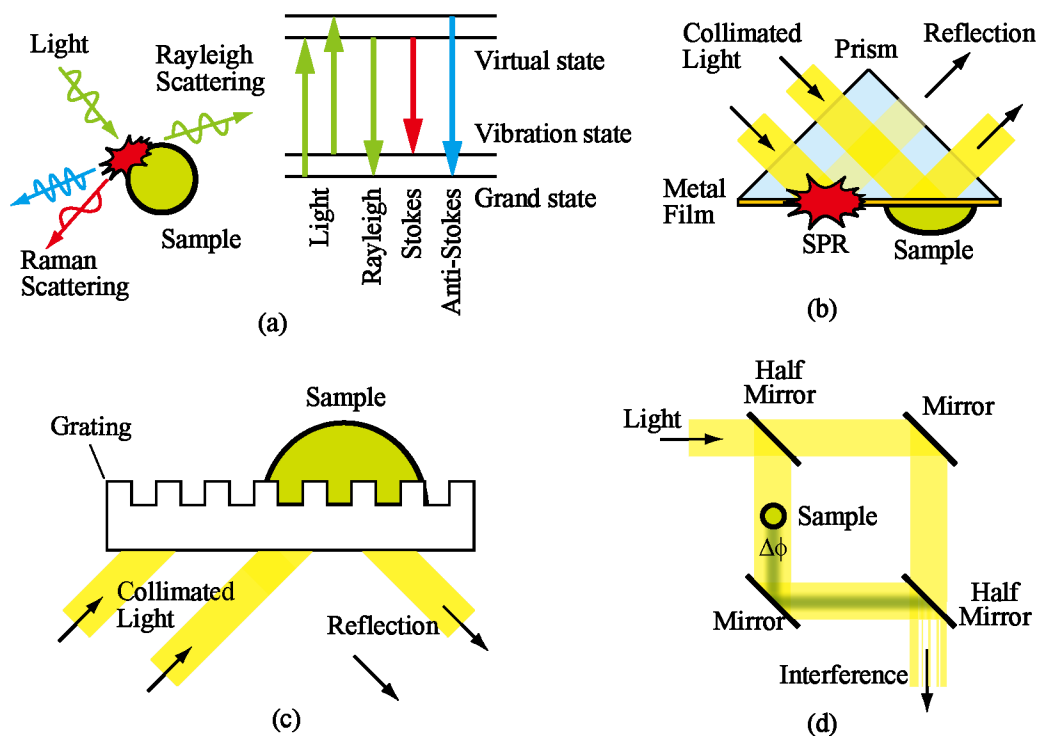
Fig. 1.2. Schematics of existing label-free methods. (a) Raman spectroscopy. Scheme (left), Energy band diagram (right). (b) Surface plasmon resonance. (c) Grating. (d) Phase holographic microscope.

(SRS), coherent anti-Raman scattering (CARS), and surface-enhanced Raman scattering (SERS). SRS uses the enhancement observed when the incident light wavelength is the same as the absorption wavelength of the molecules being tested. The SRS signal is mainly Stokes Raman scattering, because the population of the ground state is greater than a vibrational state according to Boltzmann distribution. In CARS, in which the signal is composed of anti-Stokes Raman scattering, two or more wavelengths of light are used to irradiate the sample simultaneously. They roll the basic scattered light or the support light to enhance the vibrational state of the target molecules. SERS uses local surface plasmon resonance, in which the optical field localized in the metal particles is enhanced. The single-molecule enhancement is 10^6–10^7 times larger than the population-averaged enhancement. However, this method loses some of the merits of the label-free methods, i.e. the direct binding to the target, or the necessary of the labeling.

Surface plasmon resonance

A plasmon is a quantum of plasma oscillation, and surface plasmon resonance (SPR) is the coupling between the oscillation of the propagation of an electron along a metal surface and the wave number in the corresponding direction of light. This coupling condition is sensitive to the refractive index of the material attached to the metal. Thus, the coupling characteristic with the condition of the incident light can be use as a refractive index sensor. Fig. 1.2(b) shows the schematic of the Kletschmann configuration, which is the representative measurement system for plasmon resonance. When the light irradiates with the coupling angle, the reflected light is absorbed by the coupling. In contrast, without the coupling angle, the reflected light is not absorbed by the coupling. The ideal accuracy of the refractive index order (~10^{-8} RIU) required from the sensitivity, the detectable minimum signal change [1-29], and the practical accuracy (10^{-3} RIU) acquired from the absolute accuracy have been reported [1-20, 30]. Subsequently, cells are attached to the metal surface and their refractive index image is acquired from the reflection intensity distribution. The lateral spatial resolution of SPR is influenced by the propagation of plasmon resonance, whereas the image resolution is limited by the diffraction limit. The propagation length is ~7 μm with an Au film at 633 nm [1-19] or ~40 μm with an Ag film at 633 nm [1-16], which are not sufficient given the size of a human cell. The propagation of plasmon can be canceled by the optical system alignment to compensate by an anti-phase adjustment [1-19, 20], but the reported resolution was improved to no greater than 1 μm. Furthermore, this technique requires alignment expertise and is not commercially available.

Grating

The reflection condition of gratings is influenced by the refractive index of the material

attached to the grating. Fig. 1.2(c) shows a schematic for this technique. The critical angle that reflects the lowest intensity is the standard for the change in the angle corresponding to the change in the refractive index. The intensity of the reflected image with all incident angles indicates the refractive index image of the material attached to the grating surface. The spatial resolution is the same as that for optical microscopy and real-time observation is available with this technique. However, the reflection condition with the angle has a gradual curve, e.g., the full width at half maximum is larger than the change in the angle between the cell and the culture fluids [1-21]. This means that signals for minute changes in the refractive index tend to be buried in noise.

Methods using interference

Phase contrast microscopy and differential interference microscopy are simple methods that can be used to emphasize the boundary of a structure that has the same transmittance as its surroundings. In phase contrast microscopy, directly transmitted light is interfered with diffracted light, whereas in differential interference microscopy, the change in the refractive index between two neighboring points is visualized as brightness. Due to the difficulty in evaluating physical quantities, these methods can only observe organelles [1-3]. However, phase holographic microscopy is capable of quantitative evaluation by using the interference between the transmitted light and the reference light, as shown in Fig. 1.2(d) [1-26 − 28]. The target object of this method is a dry mass with a detection limit of the order of ~1 pg, defined as the weight of the cell when water has evaporated and which mainly depends on protein concentration and cell volume. However, this method cannot distinguish spatially to the light incident direction, which makes absolute evaluation from the measured dry mass difficult.

1. 1. 3 **Requirements**

From the existing methods discussed above, the general requirements for label-free cell imaging can be categorized as follows.

1   Label-free with high throughput
2   High accuracy for the detection of cellular behavior
3   Small spatial resolution compared to that of a cell
4   Non-invasive
5   Moving image and high frame rate for real-time observation

As mentioned above, label-free methods are anticipated to be high throughput: if the

throughput quantity of such a method is similar to that of labeling methods, then the relative merits of the label-free method may become diminished. The simplest method for detecting minute cellular behavior is the identification of the target object. If the target object contains an identifying mechanism, e.g., Raman scattering, then the observation of an arbitrary molecule is available. However, such a method requires applying a physical action to the target, which may be invasive to cells. Another way to detect cellular behavior is quantitative evaluation with highly accurate resolution. In such a method, detection regardless of fine spatial resolution is necessary. Thus, accuracy is more important than spatial resolution. Spatial resolution should be small compared to the size of a human cell (tens or a few tens of micrometers), meaning that a resolution of less than a micrometer is required. Cell toxicity caused by the imaging method could inhibit intracellular interaction; therefore, non-invasiveness is desirable. Toxic assessments such as the trypan blue exclusion test are preferred for evidence of this, but cell culturing can be regarded as the easiest test to show this, because of the difficulty of cell culturing under cell toxicity conditions. Real-time observations can acquire data on cellular interactions effectively; to achieve this, the required frame rate is determined by the time scale of the observed cell element, e.g., days for a cell cycle, hours for a protein reaction, and less than seconds for the beat of a heart muscle cell.

1.2 **Photonic crystal nanolaser sensor**

This section introduces a photonic crystal (PC) nanolaser, which can be applied to the sensing of the refractive index n and its sensing applications. In this study, we used this nanolaser for label-free imaging.

1.2.1 **Nanolaser**

Fig. 1.3(a) shows a schematic of the PC nanolaser. The triangular lattice hole patterns of a PC are arranged in a slab composed of an active material. This structure is called the PC slab. The laser cavity consists of a submicron space, which was formed by shifting two adjacent holes (lattice shift-type H0 nanocavity). Fig. 1.3(b) is an example of the photonic band diagram of the PC slab. The blue band indicates the photonic band gap (PBG), which is the forbidden band for the photon [1-31]. The gray region highlights a light cone that does not satisfy the total internal reflection condition for the vertical angle. By designing the resonant wavelength to be in the range of the PBG and outside of the light cone, the cavity can confine light by index contrast for the vertical angle and PBG for the lateral angle. Such strong optical confinement enables the small modal volume. The PBG also works for luminescent processes. This inhibition
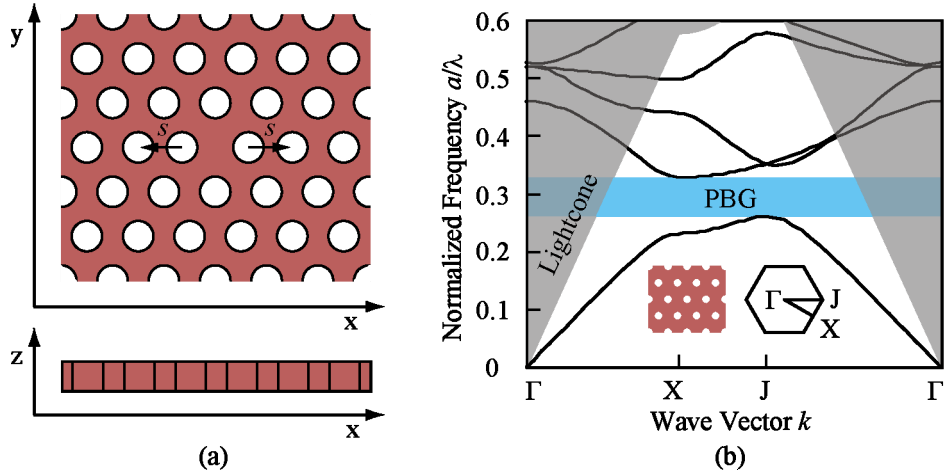
Fig. 1.3. PC nanolaser. (a) Structure. (b) Example of a photonic band diagram of the PC slab.

of unwanted spontaneous emission makes lasing emission easy. The small modal volume increases the spontaneous emission coupling to the lasing mode by the Purcell effect [1-33]. In addition to this setup, PC nanolasers with other types of cavity have been researched widely [1-34 − 44]. We fabricated the PC nanolaser with the H0 nanocavity using a commercially available GaInAsP single-quantum well wafer with a photoluminescence peak of ~1.55 µm. This PC nanolaser functions easily and effectively by photo-pumping at room temperature in an aqueous environment and has a very small modal volume, which is effectively ~0.15 $(\lambda/n)^3$.

1. 2. 2 Nanolaser sensor

The PC nanolaser is a highly accurate sensor for sensing the refractive index n. The mechanisms of such sensors are categorized by their optical micro/nanocavity. When these cavities are exposed to an environment, a resonant wavelength shift $\Delta\lambda$ occurs due to the refractive index change Δn of the environment in the evanescent field. Smaller cavities are more sensitive because of the increase in the ratio of the light path in the evanescent field. Thus, a PC structure with a high index contrast and a large PBG is generally used for strong optical confinement and miniaturization of the cavity. In addition to PC nanolasers, various other types of optical micro/nanocavity structure have been researched, including microspheres, microtoroids, microrings, PC waveguides, and PC passive cavities. Of these structures, the PC nanolaser has the desirable characteristics of having a small modal volume, high density integration, and a simple-functioning optical system. Fig. 1.4 shows the schematics of the spectra for when the device is put into liquids with different n; it shows the red shift of the resonant wavelength λ with the increase in the refractive index n. We obtained a high sensitivity $A \equiv \Delta\lambda/\Delta n$ of 400 nm/RIU, with an index resolution of the order of 10^{-5} RIU for liquids in a.

7
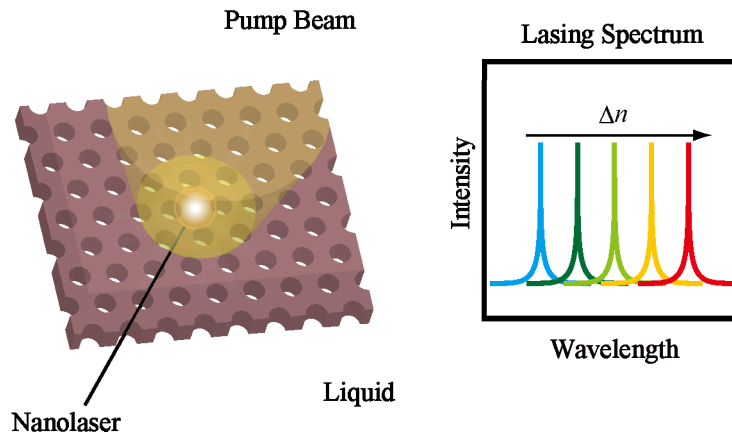
Fig. 1.4. Schematics of the sensing using PC nanolaser. Left panel shows the image of the measurement. Right panel shows the lasing
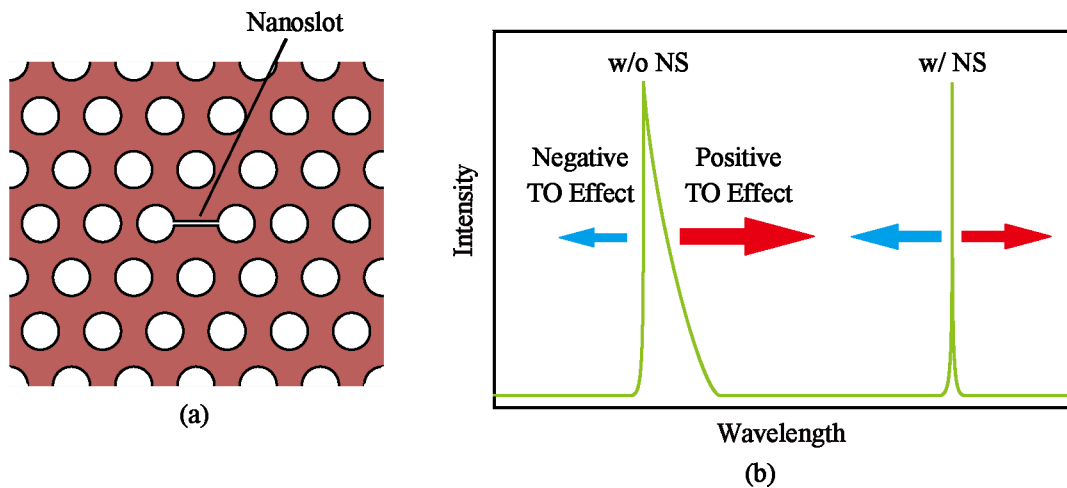
Fig. 1.5 Schematics of NS nanolaser. (a) Structure. (b) Comparison of influence of TO effect to the spectra between with and without NS.

single device [1-35]

Furthermore, the laser sensor has an aptitude for sensing in water. The spectral linewidth is important for the wavelength resolution. Passive cavities generally use Si and SiO_2 to decrease a loss in infrared bandwidth and increase the Q factor of the sharpness of the linewidth. However, in measurements in water, the absorption of water limits the total Q factor and the linewidth plateaus, whereas the active material device can increase this sharpness by stimulated emission. However, the PC nanolaser has a high thermal resistance, which is of the order of 10^6 K/W. The thermo-optic (TO) effect under pulse pumping conditions increases the spectral linewidth up to

a maximum of ~10 nm in air. This problem in the limitation of the resolution of *n* is known as wavelength chirping. We also found that incorporating a nanoslot (NS) into the nanolaser in water localizes the laser mode and balances the positive TO effect in the semiconductor and the negative one in water. Fig. 1.5 shows the Schematics of NS nanolaser. The comparison of spectra with and without NS show spectral narrowing and more stable peak wavelength in NS structure.

1. 2. 3 **Applications**

We used the PC nanolaser sensor for biomolecule sensing with an immunoassay protocol. A schematic for the setup is shown in Fig. 1.6. The PC nanolaser was modified with antibodies and the reference λ was measured in a liquid environment. The corresponding target antigens were injected and bound specifically to the antibodies. The λ was then measured again, and the Δλ before and after the injection reflected the binding of the antigen. Thus, this immunoassay can identify the target antigen due to the specific binding between the antigen and antibody, and can be applied to the sensing of various proteins by choice of the antibody. This assay does not require labeling of the antigen, and is therefore, a label-free method. By using such a protocol, the detection of tens of zM of Streptavidin (a model protein that has specific binding) and 255 fM bovine serum albumin (standard protein) were reported [1-37, 39]. These detection limits are quite low, indicating the potential of using the PC nanolaser as a sensor.

Another application of the PC nanolaser is for spectrometer-free refractive index sensing. The integration of several PC nanolasers was fabricated. These nanolasers have slightly modified structural parameters in order to achieve lasing with different values of λ. Each PC
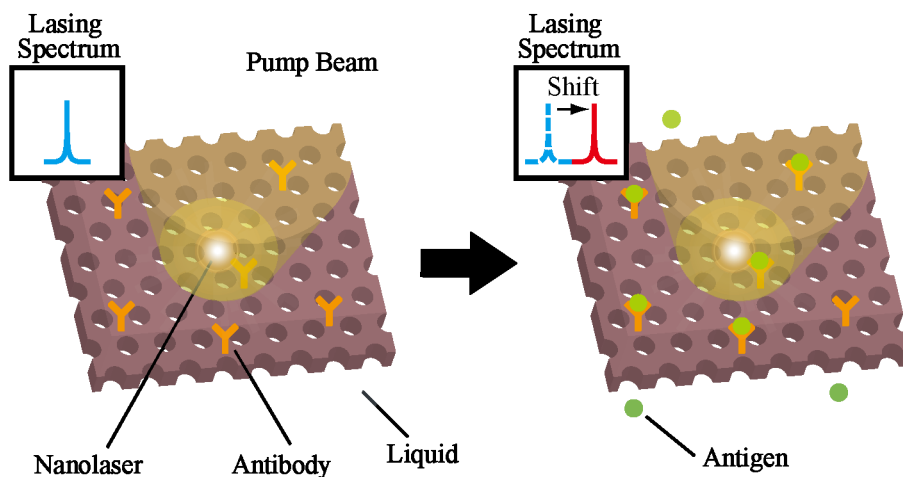
Fig. 1.6. Scheme of immunoassay using PC nanolaser.

9

nanolaser has a different λ to reflect the environment *n*. Through an appropriate wavelength filter, the near-field pattern shows a lack of lasing spots, which reflects the environment *n*. Thus, this system can operate as a spectrometer-free refractive index sensor. This application indicates that integrating multiple PC nanolasers has the potential to provide novel functionality.

The other sensing mechanism is also studied such as the opto-mechanical sensing which observed the variation of the mechanical vibration from using optical signal. In such sensing the suppress of the thermal noise should be important, so that not suitable for an ordinary temperature in cellular environment.

1.3 **Proposal**

As discussed above, label-free methods are anticipated to play a critical role in the future of cell imaging. In particular, PC nanolasers offer excellent label-free sensing, and the potential to integrate PC nanolasers with high density is possible and practical. We therefore posited that an integrated PC nanolaser sensor can be used as a device for imaging cells, because the spatial resolution based on the small modal volume and the high accuracy of the refractive index resolution satisfy the demands for such cell imaging. Thus, we designed a nanolaser array as an image sensor for living cells and demonstrated its preliminary operation. Fig. 1.7 shows the schematic of the proposed imaging method, in which the cells are attached to the PC nanolaser
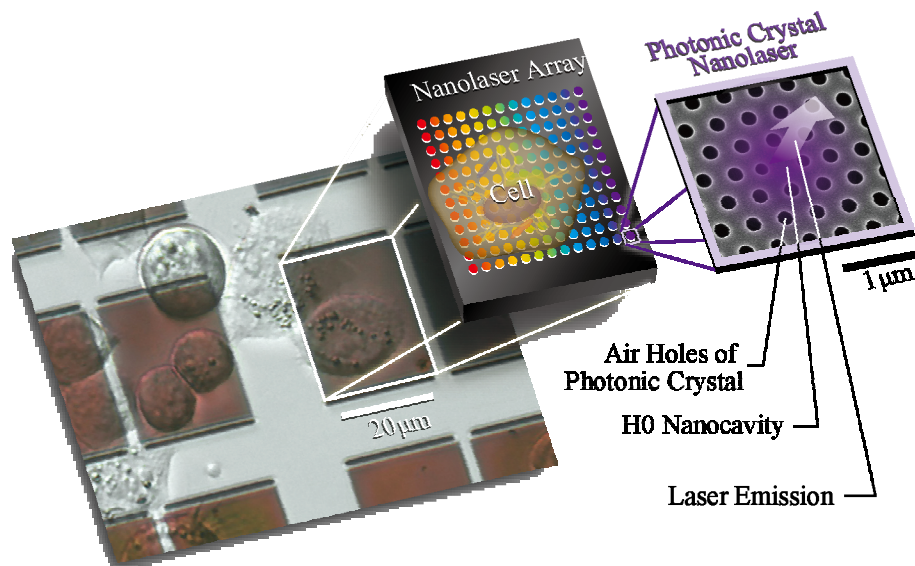
Fig. 1.7. Nanolaser array on which cells are cultured. Left: optical micrograph of nanolaser arrays and HeLa cells. Middle: schematic of a cell on the nanolaser array. Right: scanning electron micrograph of a fabricated H0-type nanolaser. [1-45]

10

array. Each PC nanolaser lasers with a wavelength reflective of the refractive index of the cell within the modal area. In this report, we demonstrate live cell imaging using a PC nanolaser array, establish the system for cell imaging, and outline the key specifications of this imaging method.

1.4 **This study**

1.4.1 **Independent array operation**

In the PC nanolaser, light is confined by the PBG in the periodic structure of the PC, so that the resonant mode is partly spread in the PC region. The distribution range is of several periods of the PC, which corresponds to several micrometers. Fig. 1.8 shows the schematics of modal field distributions of the PC nanolaser with its wide intensity range. The modal distributions of individual nanolasers overlap with each other to give a high-density integration of the PC nanolaser, and thus coupling between the PC nanolasers may occur. However, the independent operation of each nanolaser in the array is necessary for its use as an imaging device. Therefore,
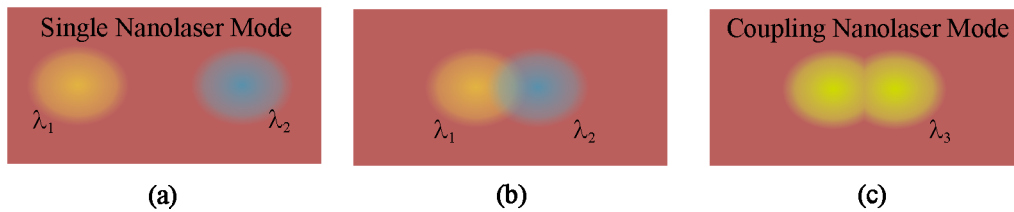
Fig. 1.8. Schematics of modal distribution in high density integration. (a) Single mode operation with a sufficient space between nanolasers. (b), (c) Modal distributions with mode overlap. Independent operation, or coupling operation, respectively.
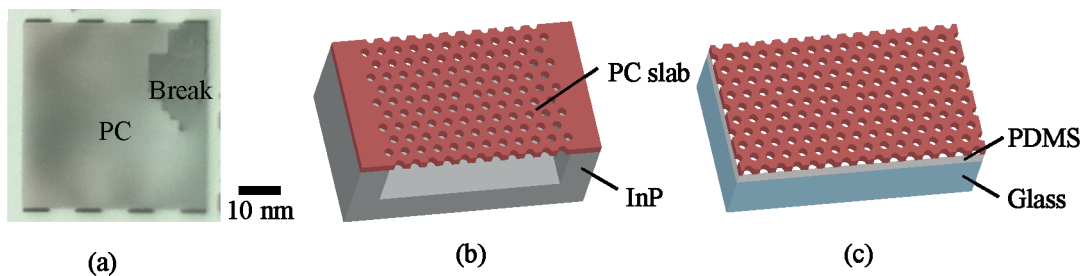
Fig. 1.9 Schematic of problem of, and solution to, the fragility of the PC slab area. (a) Optical micrograph of break in previous air bridge structure. (b) and (c) Air bridge structure and bonding structure, respectively.

11

we examined the nature and extent of the coupling, and ultimately, proposed its inhibition. We fabricated the nanolaser array and observed its operation with and without the coupling. The coupling showed various patterns and was not inhibited simply by the difference between the wavelengths of the individual nanolasers. Additionally, dividing the semiconductor slab between PC nanolasers, like insulation in an antenna, did not inhibit the coupling because this optical coupling does not occur electrically. Furthermore, such modulation produced a defect in the PC, which generated new resonance. By comparing nanolaser arrays with and without the coupling, we discovered that the occurrence of the coupling corresponds to the resonant mode and that the resonant mode can be controlled by the diameter of the hole in the PC. This structural optimization enables the array to operate independently, which is vital for the proposed imaging application.

1. 4. 2 **Fabrication of large-area device**

For the imaging of a human cell, the observation area should be larger than the size of a cell, which is ten to a few tens of micrometer. However, the size of the previous PC nanolaser array was limited to ~25 μm^2 by the fragility of its air bridge structure in which the thickness of the slab was 180 nm. Fig. 1.9(a) shows an optical micrograph of the broken PC. We proposed to solve this problem by using a bonding structure and established a new fabrication process as shown in Fig. 1.9(b) and (c). We focused on using polydimethylsiloxane (PDMS) resin as a bonding layer. PDMS is used in the flow channels of micro total analysis systems and for cell culturing, and therefore, has an aptitude for cell imaging. PDMS has a refractive index of 1.4 RIU and a TO coefficient of −0.5 RIU/K [1-49], and therefore, has an aptitude to be used as a laser cladding material. Two methods are possible to achieve this bonding. One uses a polymerization reaction with a monomer and catalytic substance mixture, and the other uses the adhesive property of the polymer surface. In this study, the polymerization method was used to achieve a flatter bonding surface. We solved the fragility of the initial array by bonding the GaInAsP slab onto a glass substrate. Additionally, we developed a process to prevent the PDMS from covering the cavity surface, which would make sensing impossible. As a result of these developments, we succeeded in fabricating a 21 × 21 = 441 nanolaser array in an area of 100 μm^2 with 100% lasing yield.

1. 4. 3 **Using the system for imaging**

To use this system for imaging, it was first necessary to obtain the spectral data for each nanolaser within the array. The optical system we used was basically the same as the previous

setup [1-34 − 41]. The spectrum of each nanolaser in the array was measured by scanning a small spot of pumping light. However, the collection of these data was inhibited by the spectra of neighboring nanolasers being observed simultaneously, due to the hysteresis of the piezometer for the scanning and the size of the pumping light spot. Thus, we adjusted the wavelength of each nanolaser to differ from its surroundings, and proposed the development of identification system using wavelength in the case of a mixed spectra. In a previous report, the wavelength of each nanolaser was controlled by the amount of shift in the H0 cavity. However, the ability to control these wavelengths is limited by the counter change from the proximity effect in electron-beam (EB) lithography. Therefore, in this study, we controlled the wavelengths by tuning the diameter of the shifted holes, and permitted monotonic increase control with ~160 nm bandwidth. In this way, identification by wavelength was possible. Another problem we encountered was the intensification of data processing work required, with respect to the obtained spectra and the coordinate control in the measurements made, which increases with the integration scale of the nanolaser array. Therefore, we established automated systems for the piezoelectric micrometer in the mirror body of the microscope, the optical spectrum analyzer, the diffractive grating, and the array photodetector, all of which were controlled by computer. Furthermore, we developed an automated program for the scanning of a pumping spot in the array. We also automated the data processing of the identification of an arbitrary nanolaser λ from the measured spectral data and the mapping of the $\Delta\lambda$ of each nanolaser corresponding to the nanolaser array arrangement.

1.4.4 **Demonstration of refractive index imaging**

To confirm the discrimination of the distribution for a test pattern, we first prepared a nanolaser array, formed a resist pattern onto the device, and measured λ for all nanolasers. The resist pattern was washed out, and the λ values were measured again. The figure that maps $\Delta\lambda$ between these measurements corresponds to the boundary of the resist pattern in an optical micrograph. The image based on the index change $\Delta n \equiv \Delta\lambda/A$ is more valuable for evaluating cellular behavior. As mentioned, the most attractive feature of this nanolaser sensor is its high index resolution, of the order of 10^{-5} RIU, which should be effective for detecting, for example, the emission of secretory proteins from cells. However, when nonuniformity in the sensitivity A between the nanolasers is larger than this value, the Δn image distorts. To guarantee the correspondence between the Δn image and the actual Δn profile, the nonuniformity must be calibrated. Therefore, we calibrated the nonuniformity in Δn by evaluating the sensitivity A of each nanolaser in advance. For this evaluation, we measured λ of all nanolasers in sugar water with various concentrations, whose refractive indices were also measured independently by a

refractometer. *A* for the liquid index was obtained from $\Delta\lambda/\Delta n$ for all nanolasers. Subsequently, Δn was obtained from $\Delta\lambda/A$ for each nanolaser, and the measured nonuniformity in *A* was found to be ~10%. As a result, we demonstrated the imaging of Δn for cell imaging.

1. 4. 5 **Improvement of refractive index resolution**

Although various refractive index sensors have been reported, the discussion of their refractive index resolutions has been limited mostly to the ideal case, as calculated by a sensitivity and minimum detectable change in a signal. However, the measured *n* may be affected by fluctuations, and the real refractive index resolution may be far from the ideal case. In contrast, in this study, we provide a more comprehensive discussion of the refractive index resolution by accounting for errors in the measurement of *n* caused by fluctuations. In a nanolaser, the main cause of error in *n* is fluctuations in the spectra and sensitivity. With respect to the fluctuation in sensitivity, we calculated the effect of the asymmetry that results from only one side of the PC slab detecting the Δn. From the nonlinearity in the equivalent *n* and the wavelength resolution in the spectroscope, the accuracy is $\sim10^{-5}$ RIU. With respect to fluctuation in the spectra, the absolute accuracy of Δn was defined as the difference between the Δn obtained in the above manner and the value directly measured by the refractometer. Our simple PC nanolaser showed an absolute accuracy of $\sim10^{-2}$ RIU. We then tried to suppress the fluctuations in the laser spectrum that are mainly caused by TO chirping. In a previous study, we reported that TO chirping broadens the laser spectrum and causes fluctuations in the peak wavelength, particularly under the pulsed pumping condition [1-36] that was employed in this study to avoid severe heating. We also showed that incorporating an NS into a nanolaser in water localizes the laser mode and balances the positive TO effect in the semiconductor and the negative one in water, which we confirmed from the observed spectral narrowing and more stable peak wavelength. We expect similar cancellations to occur, even in the device bonded onto PDMS, because the PDMS on the reverse of the device has a negative TO coefficient of -0.5 RIU/K, which is similar to that of water, and the front side is exposed to water just as for the previous case. We fabricated the NS nanolaser array and measured the absolute accuracy. We observed that the NS narrowed the spectrum and reduced the scattering range of absolute accuracy to 2×10^{-3} RIU.

1. 4. 6 **Improvement in the measurement frame rate**

Within our method, the frame rate is determined by the time taken for the measurement of the spectra of all nanolasers in the array. At first, we intended to measure the spectra of the

nanolaser array one by one by scanning them with a pumping light spot. However, using this method, the frame rate increases when the scale of integration is large; for example, in the 441 nanolaser array, the frame rate was 12 min/frame, which means that real-time observation would be impossible However, parallel measurement of nanolasers can reduce this frame rate and the number of nanolasers lasing simultaneously can be controlled by the size of the pumping spot. We proposed to integrate the PC nanolaser with different λ values close to each other, and pump them simultaneously with a large spot of pumping light. However, the problem with this was that the way the array was fabricated made identification by λ impossible. Instead, we tried to develop a method to control the λ with a post-processing step, by trimming them via light pumping in a dilute hydrochloric acid solution. By using this trimming method, we fabricated a $3 \times 3 = 9$ nanolaser array with a wavelength interval of 2.5 nm, which was larger than the standard $\Delta\lambda$ obtained by cellular attachment. By simultaneous pumping and measurement, the frame rate was improved to ~2 s/frame.

1.4.7 Demonstration of cell imaging

First, we developed a measurement system appropriate for cells by preparing a flow channel composed of PDMS to avoid evaporation of the culture fluids, enable the injection of the reagent, and control the temperature and pH. The culturing of HeLa cells in the flow channel was demonstrated, and then, HeLa cells were attached to the nanolaser array for incubation for half a day. The nanolaser array with the cells was then set as the measurement system within the culture fluid environment. The λ of the array were then measured repeatedly. After the measurement, the cells were removed by *trypsin* and the reference λ were measured again. We successfully acquired the cell image by mapping the $\Delta\lambda$, the difference in λ with and without the cells, relative to the positions of the nanolaser array. The regions with attached cells gave a $\Delta\lambda$ signal. We also acquired the time evolution of the $\Delta\lambda$ image and cellular reaction for the reagent, and demonstrated a Δn observation by using an NS nanolaser array and a high frame rate observation via the post-processing trimming method outlined.

1.5 This thesis

This thesis is organized into five thematic chapters, namely "Introduction", "Principle", "Device", "Fundamental Operation", and "Cell Imaging". The content of this study is categorized into the proposition of the novel method, the demonstration of the method, the development of the demonstration, and the imaging properties. In Chap. 2 Principle, a description of the content of the proposition and a discussion of the imaging properties is given.

In Chap. 3 Device, details of the fabrication and system development are given. In Chap. 4 Cell imaging, a description of the demonstration of cell imaging using the proposed method is given. Table 1.1 shows the correspondence between the contents and chapters. The definition of and improvement in the refractive index resolution, the structure for improvement, and the actual properties of the refractive index resolution are described in Chaps. 2, 3, and 4, respectively. The improvement in the measurement frame rate, the mechanism, the fabrication process, and the properties are also described in Chaps. 2, 3, and 4, respectively. The details of the demonstration of proposed cell imaging method are described in Chap. 5.

Table 1.1 Overview of this thesis.

Contents of this study	Principle	Device	Fundamental operation	Cell imaging
Proposition of this cell imaging method	✓			
Structural optimization for independent array operation		✓		
Fabrication of large area device		✓		
Establishment of system to imaging			✓	
Demonstration of refractive index imaging			✓	
Definition and improvement of refractive index resolution	✓	✓	✓	
Improvement of measurement frame rate	✓	✓	✓	
Demonstration of cell imaging				✓

Reference

[1-1] H. Robert, "Micrographia: or some physiological descriptions of minute bodies made by magnifying glasses with observations and inquiries thereupon", *Royal Society*, 1667.

[1-2] B. Böttcher, S. A. Wynne, and R. A. Crowther, "Determination of the fold of the core protein of hepatitis B virus by electron cryomicroscopy", *Nature*, vol. 386, pp. 88-91, 1997.

[1-3] B. Alberts, A. Johnson, J. Lewis, M. Raff, K. Roberts, and P. Walter "Molecular biology of the cell (5th ed.)", *Newton Press*, 2010.

[1-4] P. N. Prasad, "Introduction to biophotonics", *Johin & Sons Inc.*, 2003.

[1-5]   J. Liou, M. Fivaz, T. Inoue and T. Meyer, "Live-cell imaging reveals sequential oligomerization and local plasma membrane targeting of stromalinteraction molecule 1 after Ca^{2+} store depletion", *Proc. Natl. Acad. Sci.*, vol. 104, no. 22, pp. 9301-9306, 2007.

[1-6]   C. T. Jones, M. T. Catanese, L. M. J. Law, S. R. Khetani, A. J. Syder, A. Ploss, T. S. Oh, J. W. Schoggins, M. R. MacDonald, S. N. Bhatia, and C. M. Rice, "Real-time imaging of hepatitis C virus infection using a fluorescent cell-based reporter system", *Nature Biotechnology*, vol. 28, no. 2, pp. 167–171, 2010.

[1-7]   H. Wang, Y. Fu, P. Zickmund, R. Shi, and J. Cheng, "Coherent anti-Stokes Raman scattering imaging of axonal myelin in live spinal tissues", *Biophysical J.*, vol. 89, no. 1, pp. 581-591, 2005.

[1-8]   E. M. A. Ali, H. G. M. Edwards, and I. J. Scowen, "*In-situ* detection of single particles of explosive on clothing with confocal Raman microscopy", *Talanta*, vol. 78, no. 3, pp. 1201-1203, 2009.

[1-9]   C. L. Evans, E. O. Potma, M. Puoris'haag, D. Cote, C. P. Lin, and X. S. Xie, "Chemical imaging of tissue in vivo with video-rate coherent anti-Stokes Raman scattering microscopy", *Proc. Natl. Acad. Sci.*, vol. 102, no. 46, pp. 16807-16812, 2005.

[1-10] C. L. Haynes, A. D. McFarl, and R. P. V. Duyne, "Surface-enhanced Raman spectroscopy", *Anal. Chem.*, vol. 77, no. 17, pp.338 A-346 A, 2005

[1-11] C. W. Freudiger, W. Min, B. G. Saar, S. Lu, G. R. Holtom, C. He, J. C. Tsai, J. X. Kang, and X. S. Xie, "Label-free biomedical imaging with high sensitivity by stimulated raman scattering microscopy", *Science*, vol. 322, no. 5909, pp. 1857–1861, 2008.

[1-12] Y. Yanase, T. Hiragun, S. Kaneko, H. J. Gould, M. W. Greeaves, and M. Hide, "Detection of refractive index changes in individual living cells by means of surface plasmon resonance imaging", *Biosens. Bioelectron.*, vol. 26, no. 11, pp. 674-681, 2010.

[1-13] Y. Yanase, H. Suzuki, T. Tsutsui, T. Hiragun,Y. Kameyoshi, and M. Hide, "The SPR signal in living cells reflects changes other than the area of adhesion and the formation of cell constructions", *Biosens. Bioelectron.*, vol. 22, no. 6, pp. 1081-1086, 2007.

[1-14] Y. Yanase, A. Araki, H. Suzuki, T. Tsutsui, T. K. Kimura, K. Okamoto, T. Nakatani, T. Hiragun, and M. Hide, "Development of an optical fiber SPR sensor for living cell activation", *Biosens. Bioelectron.*, vol. 25, no. 5, pp. 1244-1247, 2010.

[1-15] R. Y. He, C. Y. Lin, Y. D. Su, K. C. Chiu, N. S. Chang, H. L. Wu, and S. J. Chen, "Imaging live cell membranes via surface plasmon-enhanced fluorescence and phase microscopy", *Opt. Express*, vol. 18, no. 4, pp. 3649-3659, 2010.

[1-16] K. F. Giebel, C. Bechinger, S. Herminghaus, M. Riedel, P. Leiderer, U. Weiland, and M. Bastmeyer, "Imaging of cell/substrate contacts of living cells with surface plasmon resonance microscopy", *Biophysical J.*, vol. 76, pp. 509–516, 1999.

[1-17] R. Ziblat, V. Lirtsman, D. Davidov, and B. Aroeti, "Infrared surface plasmon resonance: a novel tool for real time sensing of variations in living cells", *Biophysical J.*, vol. 90, pp. 2592-2599, 2006.

[1-18] J. G. Quinn, S. O'Neill, A. Doyle, C. McAtamney, D. Diamond, B. D. MacCraith, and R. O'Kennedy, "Development and application of surface plasmon resonance-based biosensors for the detection of cell±ligand interactions", *Analytical Biochemistry*, vol. 281, pp.135-143, 2000.

[1-19] G. Stabler, M. G. Somekh, and C. W. See, "High-resolution wide-field surface plasmon microscopy", *journal of Microscopy*, vol. 214, pp. 328–333, 2004.

[1-20] K. J. Moh, X. C. Yuan, J. Bu, S. W. Zhu, and B. Z. Gao, "Surface plasmon resonance imaging of cell substrate contacts with radially polarized beams", *Opt. Express*, vol. 16, no. 25, pp. 20754–20741, 2008.

[1-21] E. A. Lidstone, V. Chaudhery, A. Kohl, V. Chan, T. W. Jensen, L. B. Schook, R. Bashir, and B. T. Cunningham, "Label-free imaging of cell attachment with photonic crystal enhanced microscopy", *analyst*, vol. 136, no. 18, pp.3608-3615, 2011.

[1-22] Y. Fang, A. M. Ferrie, N. H. Fontaine, J. Mauro, and J. Balakrishnan, "Resonant waveguide grating biosensor for living cell sensing", *Biophys. J.*, vol. 91, no. 5, pp. 1925–1940, 2006.

[1-23] L. L. Chan, S. L. Gosangari, K. L. Watkin, and B. T. Cunningham, "A label-free photonic crystal biosensor imaging method for detection of cancer cell cytotoxicity and proliferation", *Apoptosis*, vol. 12, no. 6, pp. 1061–1068, 2007.

[1-24] Y. Fang, "Non-invasive optical biosensor for probing cell signaling", *Sensors,* vol. 7, no. 10, pp. 2316–2329, 2007.

[1-25] K. I. Willig, S. O. Rizzoli, V. Westphal, R. Jahn and S. W. Hell," STED microscopy reveals that synaptotagmin remains clustered after synaptic vesicle exocytosis", *Nature,* vol. 440, pp. 935-939, 2006.

[1-26] B. Rappaz; E. Cano; T. Colomb; J. Kühn; C. Depeursinge; V. Simanis; P. J. Magistretti; and P. Marquet, "Noninvasive characterization of the fission yeast cell cycle by monitoring dry mass with digital holographic microscopy", *J. of Biomedical Opt.*, vol. 14, no. 3, pp. 034049, 2009.

[1-27] M. Mir, A. Bergamaschi, B. S. Katzenellenbogen, and G. Popescu, "Highly sensitive quantitative imaging for monitoring single cancer cell growth kinetics and drug response", *PLOS ONE*, vol. 9, no. 2, pp. 1-9, 2014.

[1-28] Z. Wang, L. Millet, M. Mir, H. Ding, S. Unarunotai, J. Rogers, M. U. Gillette, and G. Popescu1, "Spatial light interference microscopy (SLIM)", *Optics Express*, vol. 19, no. 2, pp. 1016-1026, 2011.

[1-29] A. V. Kabashin, and P. I. Nikitin, "Surface plasmon resonance interferometer for bio- and chemical-sensors", *Opt. Commun.*, vol. 150, pp. 5-8, 1998.

[1-30] K. A. Tetz, L. Pang, and Y. Fainman, High-resolution surface plasmon resonance sensor based on linewidth-optimized nanohole array transmittance", *Opt. Lett.*, vol. 31, no. 10, pp. 1528-1530, 2006.

[1-31] E. Yablonovitch, and T. J. Gmitter, "Photonic band structure: the face-centered-cubic case," *Phys. Rev. Lett.*, vol. 63, pp. 1950-1953, 1989.

[1-32] E. Yablonovitch, "Inhibited spontaneous emission in solid-state physics and electronics," *Phys.Rev. Lett.*, vol. 58, pp. 2059-2062, 1987.

[1-33] E. M. Purcell, "Spontaneous emission probabilities at radio frequencies," *Phys. Rev.*, vol. 69, p.681, 1946.

[1-34] K. Nozaki, S. Kita and T. Baba, "Room temperature continuous wave operation and controlled spontaneous emission in ultrasmall photonic crystal nanolaser", *Opt. Express*, vol. 15, no. 12, pp. 7506-7514, 2007.

[1-35] S. Kita, K. Nozaki and T. Baba, "Refractive index sensing utilizing a cw photonic crystal nanolaser and its array configuration", *Opt. Express*, vol. 16, no. 11, pp. 8174-8180, 2008.

[1-36] S. Kita, K. Nozaki, S. Hachuda, H. Watanabe, Y. Saito, S. Otsuka, T. Nakada, Y. Arita, and T. Baba, "Photonic crystal point-shift nanolaser with and without nanoslots --- design, fabrication, lasing and sensing characteristics", *IEEE J. Sel. Top. Quantum Electron*, vol. 17, no. 6, pp. 1632–1647, 2011.

[1-37] S. Hachuda, S. Otsuka, S. Kita, T. Isono, M. Narimatsu, K. Watanabe, Y. Goshima and T. Baba, "Selective detection of sub-atto-molar streptavidin in 1013-fold impure sample using photonic crystal nanolaser sensors," *Opt. Express*, vol. 21, no. 10, pp. 12815–12821, 2013.

[1-38] K. Nozaki, S. Kita, Y. Arita and T. Baba, "Resonantly photopumped lasing and its switching behavior in a photonic crystal nanolaser", *Appl. Phys. Lett.*, vol. 92, no. 2, pp. 021501, 2008.

[1-39] S. Kita, S. Hachuda, K. Nozaki and T. Baba, "Nanoslot laser", *Appl. Phys. Lett.*, vol. 97, no. 16, pp. 161108, 2010.

[1-40] S. Kita, S. Otsuka, S. Hachuda, T. Endo, Y. Imai, Y. Nishijima, H. Misawa and T. Baba, "Super-sensitivity in label-free protein sensing using nanoslot nanolaser", *Opt. Express*, vol. 19, no. 18, pp. 17683-17690, 2011.

[1-41] S. Kita, S. Otsuka, S. Hachuda, T. Endo, Y. Imai, Y. Nishijima, H. Misawa and T. Baba, "Photonic crystal nanolaser bio-sensors", *IEICE Trans. Electron.*, vol. E95-C, no. 2, pp. 188-198, 2012.

[1-42] M. Nomura, S. Iwamoto, K. Watanabe, N. Kumagai, Y. Nakata, S. Ishida, and Y. Arakawa, "Room temperature continuous-wave lasing in photonic crystal nanocavity", *Opt. Express*, vol. 14, no. 13, pp. 6308-6315, 2006.

[1-43] O. Painter, R. K. Lee, A. Scherer, A. Yariv, J. D. O'Brien, and P. D. Dapkus, "Two-dimensional photonic band-gap defect mode laser", *Science*, vol. 284, 1819–1821,1999.

[1-44] H. Altug and J. Vučković, "Photonic crystal nanocavity array laser," *Opt. Express,* vol. 13, no. 22, 8819–8828, 2005.

[1-45] H. Abe, M. Narimatsu, T. Watanabe, T. Furumoto, Y. Yokouchi, Y. Nishijima, S. Kita, A. Tomitaka, S. Ota, Y. Takemura and T. Baba, "Living-cell imaging using a photonic crystal nanolaser array," *Opt. Express*, vol. 23, no. 13, pp. 17056-17066, 2015.

[1-46] T. Watanabe, H. Abe, Y. Nishijima and T. Baba, "Array integration of thousands of photonic crystal nanolasers," *Appl. Phys. Lett.*, vol. 104, no. 12, pp. 121108, 2014.

[1-47] M. Christiansen, J. M. Lopacinska, M. H. Jakobsen, N. A. Mortensen, M. Dufva, and A. Kristensen, "Polymer photonic crystal dye lasers as Optofluidic Cell Sensors", *Opt. Express*, vol. 17, no. 4, pp. 2722-2730, 2009.

[1-48] S. Zlatanovic, L. W. Mirkarimi, M. M. Sigalas, M. A. Bynum, E. Chowa, K. M. Robotti, G. W. Burr, S. Esener, and A. Grot, "Photonic crystal microcavity sensor for ultracompact monitoring of reaction kinetics and protein concentration", *Sensors and Actuatous B: Chemical*, vol. 141, no. 1, pp. 13-19, 2009.

[1-49] W. F. Yeung, and A. R. Johnston, "Effect of temperature on optical fiber transmission", *Applied Optics*, vol. 17, no. 23, pp. 3703–3705, 1978.

[1-50] A. Cetin, A. F. Coskun, B. C. Galarreta1, M. Huang, D. Herman, A. Ozcan, and H. Altug, "Handheld high-throughput plasmonic biosensor using computational on-chip imaging", *Light: Sci. Appl.*, vol. 3, pp. e122, 2014.

[1-51] A. F. Coskun, A. E. Cetin, B. C. Galarreta, D. A. Alvarez, H. Altug, and A. Ozcan,” Lensfree optofluidic plasmonic sensor for real-time and label-free monitoring of molecular binding events over a wide field-of-view”, *Sci. Rep.*, vol. 4, no. 6789, 2014.

Chapter 2
Principle

2.1 **Concept**

Fig. 1.7 indicates the scheme of the proposed imaging method. The nanolasers are aligned into a two-dimensional square lattice with a pitch large enough to prevent mutual mode coupling, and the cells are cultured on this array. Each nanolaser exhibits a λ value according to n induced by the cell. In principle, the absolute value of n can be acquired from λ. However, the culture fluid contains various foreign substances such as proteins, amino acids, and glucose, which may also attach and produce additional Δn and cause noise in the measurement of n. Such additional attachment is thought to be based on strong physical adsorption, such that the additional shift is assumed to be the drift in λ in a continuous measurement. Additionally, the environment around the cell is filled with culture fluid, the observation of the relative n from which is actually useful. Therefore, we ultimately acquire $\Delta \lambda$ in each nanolaser according to Δn induced by the cell attachment. The measurement conditions are categorized for the case without a cell, the case with a cell, and the case with a cell containing some changes. Fig. 2.1 shows the schematics of the λ and $\Delta \lambda$ images for each cell condition. The $\Delta \lambda$ image should be composed of red shift because the refractive index of a protein is larger than that of the culture fluids. The amplitude of $\Delta \lambda$ should reflect a change in the cell. The evaluation of Δn can be acquired by translation from $\Delta \lambda$. In addition, the controllability of λ contributes to the property of the identification of the nanolaser in an array. Fig. 2.2 shows the identification scheme using the wavelength of a nanolaser array. The different λ values in the nanolaser array can be integrated. Using a large spot of pumping light, the spectra from different nanolasers that fall under the spot are measured simultaneously. The spectra of each nanolaser can be identified from the measured spectra by the unique λ. These features provide distinct advantages to the proposed method, namely that they prevent noise from surrounding nanolasers, make optical alignment easy, and exhibit improved frame rates because of the parallel measurement.
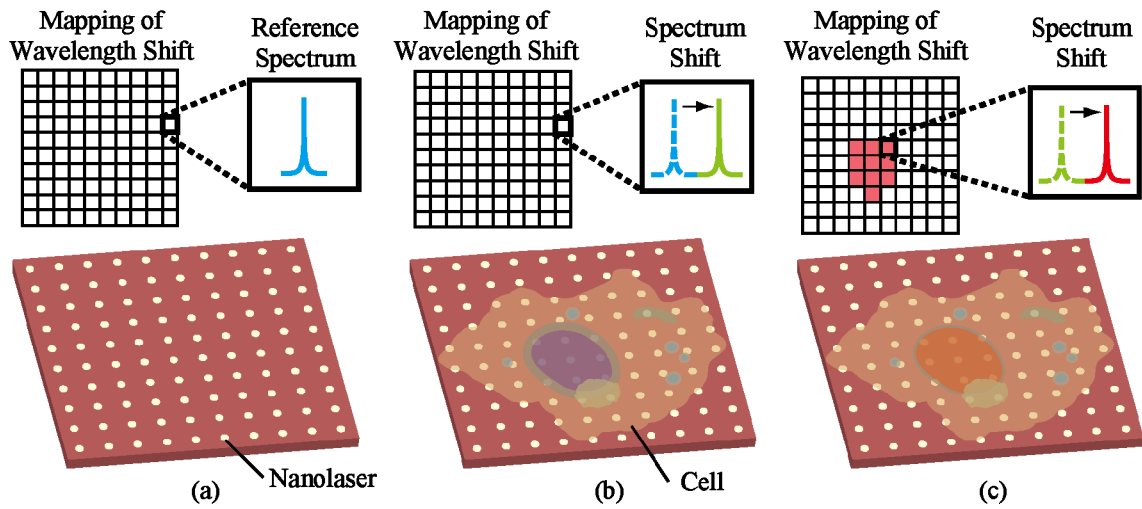
Fig. 2.1. Scheme of $\Delta\lambda$ image and the condition of the nanolaser array. (a) Without cell. (b) With cell. (c) With cell containing some changes. For each graph, the lower image shows the state of the cell, and the upper image shows the image of the $\Delta\lambda$ array, in which the color indicates the amplitude of $\Delta\lambda$.
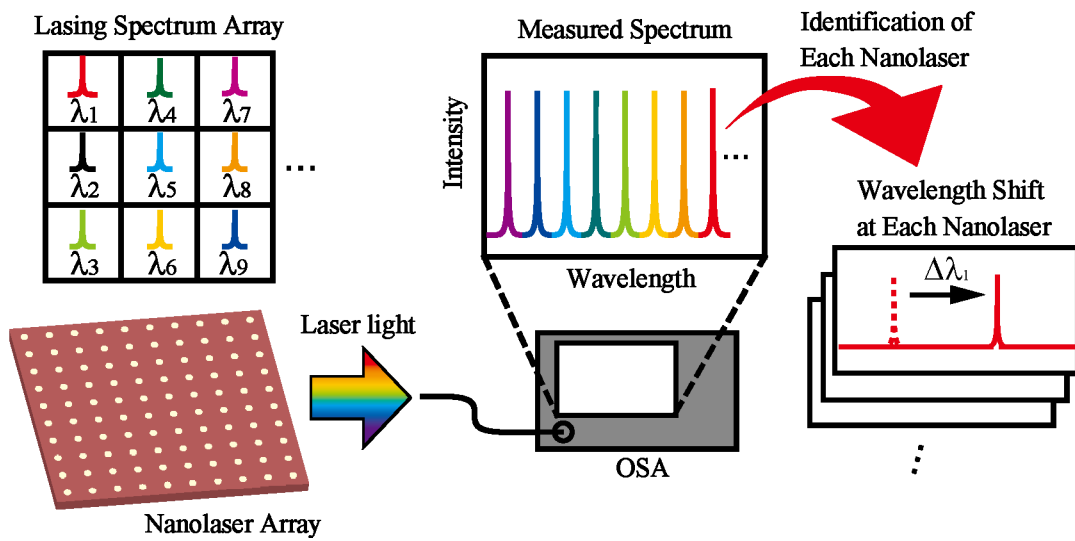
Fig. 2.2. Scheme of the identification method from the spectra measured simultaneously using a nanolaser array, by integrating different λ values.

2.2 **Features**

In this section, we show the features of the proposed method along with the requirements for cell imaging discussed in section 1.1.3. We also compare it with other methods. Table 2.1 shows the summary of this section.

Table. 2.1. Comparison of the features among cell imaging methods.

Mechanism	Target	Throughput	Accuracy	Spatial Resolution	Invasiveness	Frame Rate
Label	Molecule	Low		D. L.	Middle	Very High
SPR	Index	High	$\sim 10^{-3}$ RIU	~ 10 μm	Low	Very High
Raman Scattering	Molecule	Very High		D. L.	High	Low
Grating	Index	High	Low	D. L.	Low	Very High
Interference	Drymass	Very High	~ 1 pg	D. L.	Low	Very High
This Method	Index	High	$\sim 10^{-5}$ RIU	<1 μm	Low	High

Label-free with high throughput

As mentioned previously, this method can acquire images without the use of labels. The only preparation required is the attachment of the cell to the nanolaser array device, such that, if preliminary attachment is allowed, the initiation of measurements can be very prompt. For example, in Chap. 5, we describe the attachment of HeLa cells to the device, for which the time for attachment was half a day. In comparison, methods that use SPR and grating also require cell attachment of a similar time period, whereas methods that use Raman spectroscopy and phase holographic microscopy only require the setup of the optical system. In conclusion, the throughput of this method is fast compared to that of labeling methods, which require successive culturing of cells for several generations to confirm the gene injection.

Accuracy

As mentioned in Chap. 1, the PC nanolaser had been applied to sensing liquids and biomolecules, for which an index resolution of the order of 10^{-5} RIU for liquids in a single device was obtained. In this study, the basic structure of the PC nanolaser is the same as that for the previous report, so the same refractive index resolution should, theoretically, be achieved. The refractive index resolution of the device used in this study is discussed in section 2.3. The other method to quantitatively evaluate n is to use SPR, for which the resolution of the refractive index is of the order of 10^{-3} RIU [2-30, 2]. We calculated the value of the refractive index resolution required for cellular behavior as being of the order of 10^{-4} RIU. The difference between cytoplasm and an organelle is $\sim 10^{-2}$ RIU, e.g., the RIU of cytoplasm is ~ 1.37, of a nucleus is ~ 1.39, of mitochondria is ~ 1.4, and of a lysosome is ~ 1.6 [2-3]. The change in the refractive index during the interphase in a cell cycle is of the order of 10^{-4} RIU, which is calculated from the change in the dry mass of a yeast cell of ~ 0.1 pg/μm^2 [2-4], the depth of the yeast cell of ~ 5 μm, the density of the amino acid of ~ 0.2 ml/g, and the volume ratio within the evanescent field of ~ 0.1. The concentration of protein in cells is also equivalent to $3 \times 10^{-5} - 1 \times$

10^{-3} RIU.

Small spatial resolution compared to a cell

The size of the observation area of a single PC nanolaser is determined by the modal distribution for the planar direction and the evanescent field for the vertical direction, which are less than 1 μm^2 and ~120 nm, respectively [2-7]. The lateral resolution is sufficient for quantitative evaluation, given the size of a cell of ten or a few tens of micrometer, and superior to the propagation length of plasmon resonance of ~7 μm with a Au film at 633 nm [2-9] or ~40 μm with a Ag film at 633 nm [2-10]. However, the vertical resolution limits the observed area near membranes given typical sizes of, for example, a membrane of ~10 nm, fibronectin (the main cell adhesion protein) of >100 nm, and a transmembrane protein of ~20 nm [2-8]. The resolution of the image is determined by the pitch of the nanolaser array, which is limited by the coupling between each nanolaser in the array. Independent operation for a pitch size of 2.5 μm has been confirmed experimentally. The pitch size of 2.5 μm is the smallest for the pumping spot we used, and the ideal pitch should be limited by the formation of the PBG structure, which may be ~2 μm. This value is lower than the diffractive limit in an optical microscope. For the improvement in the observation area of a single nanolaser and the resolution of the image, a lower lattice constant in the PC is necessary. This requires the development of a nanolaser composed of other materials for operation with shorter wavelengths. Furthermore, the vertical resolution requires a change in the refractive index of the slab.

Non-invasiveness

In contrast to labeling methods, the influence of the specific molecule is not accounted for in this study. The attachment of the PC slab and heating by lasing could introduce cell toxicity. As evidence of non-invasiveness, given the difficulty of culturing cells under such conditions, cell culturing can be regarded as an easy test for cell toxicity. In this study, we used cell culturing in the measurement setup to confirm non-invasiveness. These details are given in Chap. 6. The results showed cell culturing for one day without cell death and with cell division. Furthermore, with respect to phototoxicity, this method has the advantage of producing an easily detectable signal compared to Raman methods. The operation of the pumping and lasing light with infrared discourages phototoxicity, and any thermal influence caused by lasing may be ignored because of the pulse operation of the laser that we used.

Moving images and high frame rates for real-time observations

In this method, a moving image can be acquired by continuous measurement of λ. The frame rate is determined by the detection of the λ of each nanolaser and the scanning of the

array. The practical frame rate is described in section 2.3.8, which is ~1 s in the low integration condition. The dynamics of cellular interaction are mediated by a complex system, and the period of these dynamics are dependent on the system under observation [2-8]. The frame rate in this method is sufficient to observe some types of protein reactions [2-11]. Considering the frame rate in principle, the scanning of the array can be ignored by a fan-in/fan-out system, and the frame rate should be limited by the exposure time for the detection of the spectrum. This time is generally determined by the signal intensity. Thus, this method may be faster than the Raman method and slower than SPR, grating, and digital holographic microscopy.

Based on the above, our proposed method is characterized by its high throughput, high accuracy, low invasiveness, adequate spatial resolution, and frame rates that give access to quasi-real-time observations.

2. 3 **Specifications**

This section describes the basic imaging specifications of the proposed method, and highlights the theoretical limitations and practical results of this study. Before describing these, a calculation method often used in optical simulations, 3-Dimentional (3D) finite-difference time domain (FDTD), is introduced.

FDTD simulation

In this simulation, the electrical permittivity and magnetic permeability were set for the finite divided cells, and an electric field and a magnetic field were calculated by Maxwell's equations for each divided time step between cells. For accurate simulation of equations for each divided time step between cells. For accurate simulation of electromagnetic waves, the cell
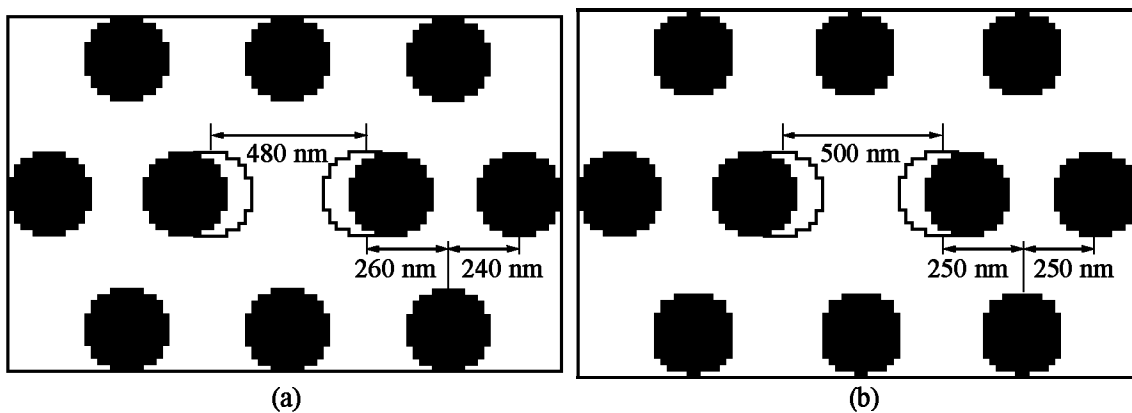
Fig. 2.3. Comparison of the alignment mechanism for the FDTD model. The mechanism of (a) a previous study and (b) this study. Black and white regions are exposed and not exposed, respectively.
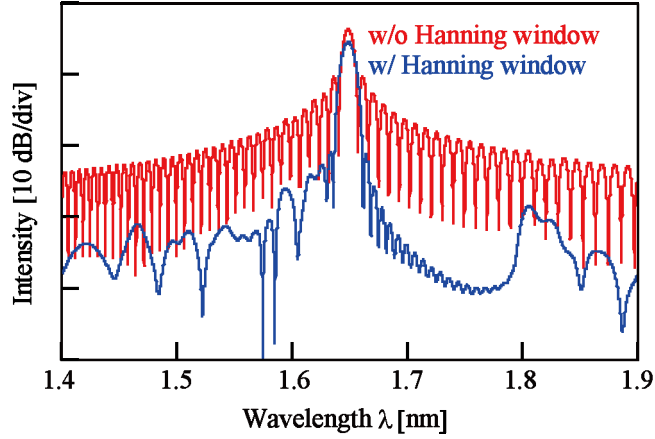
Fig. 2.4. Resonant spectra calculated by FFT. The Hanning window is applied to the electromagnetic component's time evolution before FFT.

Table. 2.2. FDTD simulation parameters.

Parameter	This study (Broadband/Specific mode)	Fullwave (RSoft)
Cell size	20 nm	20 nm
Size of calculation model	$465 \times 482 \times 120$ cell	$250 \times 238 \times 30$ cell
Unit time step	0.035 fs	0.036 fs
Number of calculation steps	$4 \times 10^4 / 7 \times 10^4$ step	2×10^{17} step
Absorption boundary	Mur 2nd-order	Perfect matched layer
Number of cluster nodes	5	1
Typical calculation time	6 h	4 h
Excitation	Spectral width: $1/e^2$ ($\sigma = 0.3/0.01 - 0.006$) Peak wavelength : 1.5 μm/modal peak	Impulse

size and unit step time were limited to less than $\lambda/10n$ and the Courant condition, respectively. The absorbing boundary was set at the boundary of the model. With these conditions defined, the propagation of the electromagnetic wave could be simulated. In the model of a PC cavity, when light is excited with a broadband wavelength element, the element without the resonant wavelength is scattered and absorbed gradually. Thus, the discrete Fourier transform of the energy remaining after the calculated step has been run indicates the resonant wavelength of the model cavity. The mode profile and the Q factor are calculated by the excitation of the specific λ element. In this study, we used the program written to this study, with parameters that were largely the same as those for previous reports [2-12, −14], and Fullwave software. Table 2.2

indicates the basic parameter of the simulation. Note that the written program settings differ from those reports in the following way. In the modeling, the real structure is get sampling due to the discrete presentation with the cell size. In previous reports, the centers of the holes corresponded to those of the cells for the refined structure of the hole model, which contained a lattice constant error in some places. In this report, the correct lattice constant was used, and the distorted hole was designed to be at the outside of the cavity center, as shown in Fig. 2.3. In Fig. 2.3 (b), the error in the centering lattice constant is resolved where the critical position of the mode should be. In the Fullwave simulation, the cell at the boundary of the holes was automatically set to the modified n. Moreover, before the discrete Fourier transform was applied, the Hanning window was introduced to reduce the noise from the hopping in the periodic function. Fig. 2.4 shows fast Fourier transform (FFT) spectra with and without the Hanning window. This shows the single-digit reduction in noise. With these adjustments, the correct calculation of λ was expected.

2. 3. 1 **Observation area**

Although the schematic of the observation area was discussed in section 2.2, the extent of the discussion for the model with the cell and culture fluid was not sufficient. In particular, further discussion on the resolution of the vertical direction and its influence on $\Delta\lambda$ is necessary because of the effects of the cellular tensional force on the cell membrane. Using a 3D FDTD written simulation, we calculated λ when the distance of the cell with the slab surface was changed. The sensing area can be calculated with this simulation as the change of λ. Here, the simple H0-type cavity with the bonding structure was used with the model of the PC nanolaser. Table 2.3. gives the calculation parameters. For the values of the cellular parameters, refer to [2-3]. Fig. 2.5 shows $\Delta\lambda$ for different attachment conditions using the FDTD written simulation.

Table. 2.3. Parameters of simulated model.

n (active layer)	3.4
n (PDMS)	1.4
n (water)	1.3321
n (culture fluids)	1.337
n (cell)	1.355
Active layer thickness	180 nm
Lattice constant a	500 nm
Hole diameter $2r$	260 nm
Shift of H0 cavity s_x	80 nm
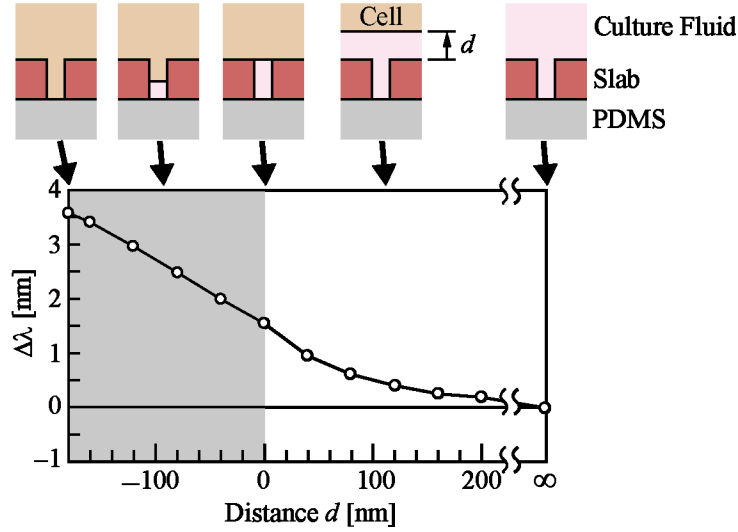
Fig. 2.5. FDTD calculation of wavelength shift for the distance between the nanolaser and cell. The distance is set to zero when the cell is attached to the top surface of the nanolaser. The negative distance means that the cell partially penetrates into the nanolaser holes. [2-18]

Here, the distance d between the nanolaser and the cell is changed and the culture fluid is assumed to be in between them. $\Delta\lambda$ is set to zero in the absence of the cell. As d is decreases, $\Delta\lambda$ increases, particularly at $d < 100$ nm, which is within the penetration depth of the laser mode. $\Delta\lambda$ is calculated to be 1.5 nm at $d = 0$, where the cell is uniformly attached to the top surface of the nanolaser. It is further increased when the cell partially penetrates into the holes of the photonic crystal slab. These calculations well explain the experimental $\Delta\lambda$ in the cell area ranging from 0.5 to 2.0 nm. We also calculated the lateral distribution of the bonding structure. Fig. 2.6 shows the modal distributions of the electromagnetic field by the excitation of the specific mode.

These results show only one polarized wave excitation in which the electric field oscillation is transverse to the PC structure. The other polarized wave can be ignored in a PC nanolaser, because in that case, the PBG does not arise. This shows that the electromagnetic field is mainly confined to the space by the shift in the H0 cavity. In this sensor, λ is reflected by the dielectric constant within the evanescent field of the electric field and the lateral spatial resolution is less than 1 μm.

2. 3. 2 Spatial resolution

As mentioned above, in this method, the spatial resolution is equal to the pitch of the nanolaser array. This pitch is limited, in principle, by the coupling between nanolasers, but
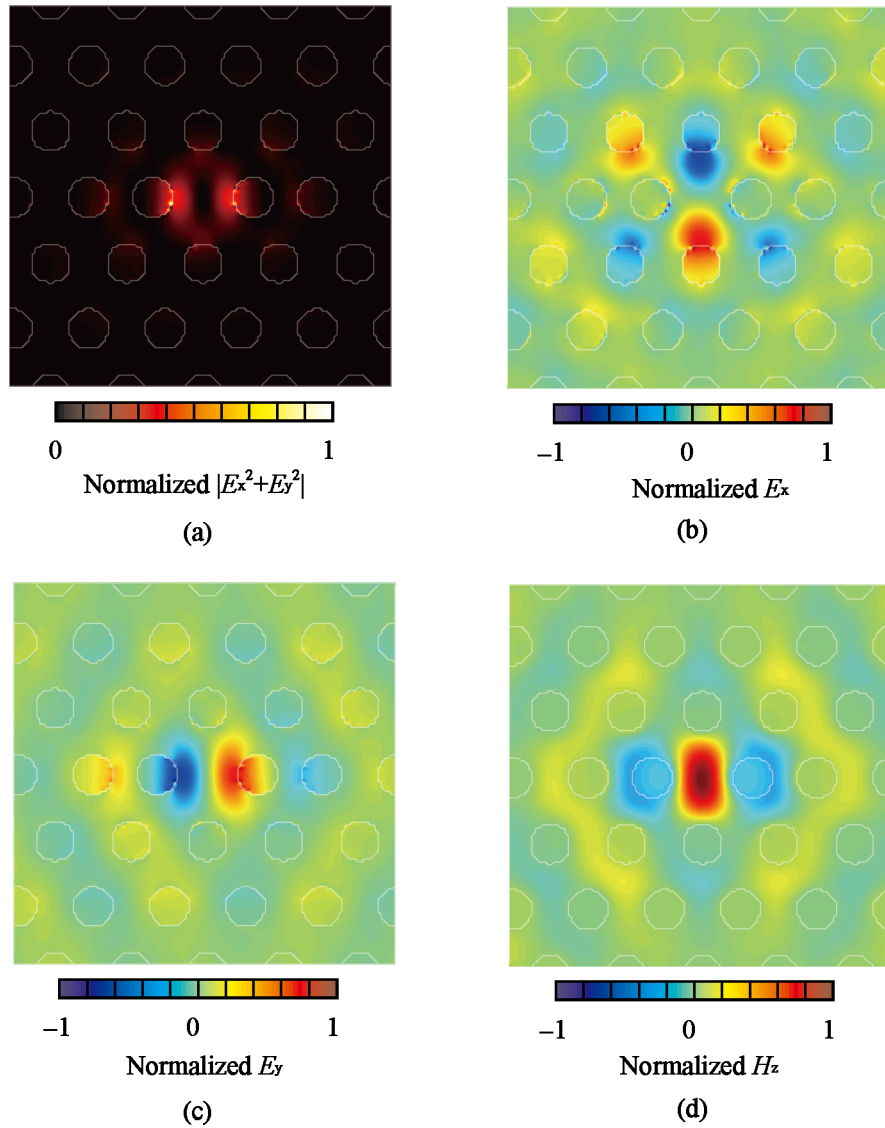
Fig. 2.6. Calculated modal distribution in the bonding model. (a), (b), (c), and (d) show the fields for $|E^2|$, E_x, E_x, and H_z, respectively.

should be 1.5−2.5 μm, because the form of the periodic structure in the PC becomes impossible. Importantly, the consensus from the established practice is that the confirmation of the λ of each nanolaser in an array requires the measurement of each single nanolaser operation by pumping a small spot of light onto it. However, this limitation can be resolved by making the control of λ larger than the fabrication error. Unfortunately, because of the quantity of the work required and the fabrication yield, we used the measurement confirmation in this study. Considering the spot size of the pumping light and the accuracy of the piezoelectric micrometer, excessively small pitches are impracticable, but we did confirm the minimum practical pitch size. Fig. 2.7(a) shows the Scanning electron microscopy (SEM) image of the 5 × 5 nanolaser array with a 2.5
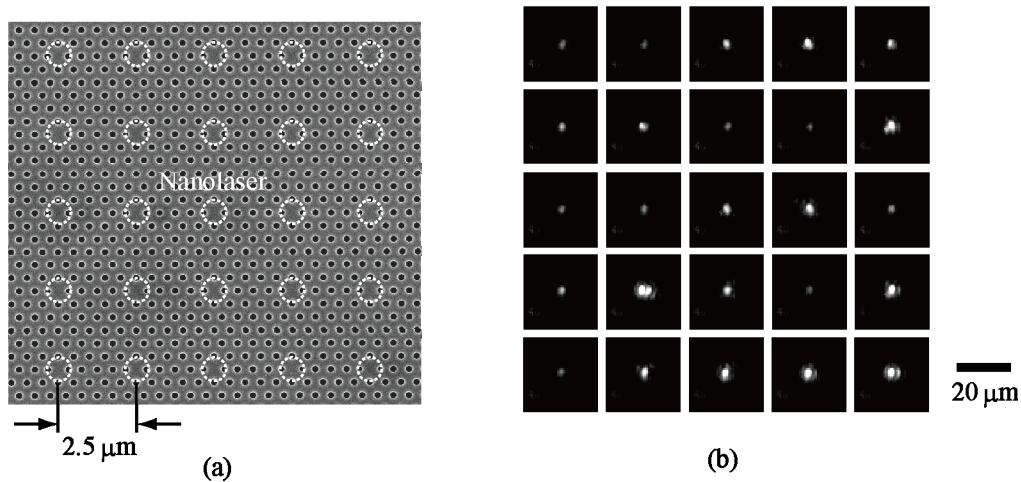
Fig. 2.7. Individual measurement in 2.5 μm pitch array. (a) SEM image of the fabricated device. (b) Near-field pattern of laser emission for 5 × 5 = 25 points.

μm pitch. Each nanolaser was individually pumped with the smallest spot (~3 μm) manipulated by a hand-operated micrometer, as shown in Fig. 2.7(b). The minimum pitch with hand-operation, or with automatic operation, is limited by the spot size or the accuracy of the piezoelectric micrometer—2.5 μm or 4.5 μm, respectively. In particular, with the nanolaser with the additional NS structure, a large pumping spot area is required for emission compared to the nanolaser without the NS. For the measurement confirmation with the larger spot size (~20 μm), the practical minimum pitch was found to be ~10 μm.

2.3.3 **Number of pixels**

In this method, the number of pixels is determined by the pitch of the nanolaser array and the integration area. The pitch is theoretically of the micrometer scale and the theoretical limitation of the area in an bonding structure is the preparable wafer size. The near-field pattern from the maximum number of nanolasers integrated in this work, which was more than 400 was shown in Chap. 4. This is first time ever that a number of that scale of nanolasers has been integrated. From a practical view, this large-scale integration degrades the frame rate, and the area over the exposure field of the EB exposure system requires the stitching of many fields. This stitching reduces the yield of a nanolaser array. However, the size of the single field of the EB exposure system of 150 μm × 150 μm is sufficient for the observation of something the size of a human cell (a few tens of micrometer). In this study, we used a 100 μm × 100 μm area for the observation of the whole cell. With a pitch size of ~5 μm, the practical number of pixels is 21 × 21 = 441 array.
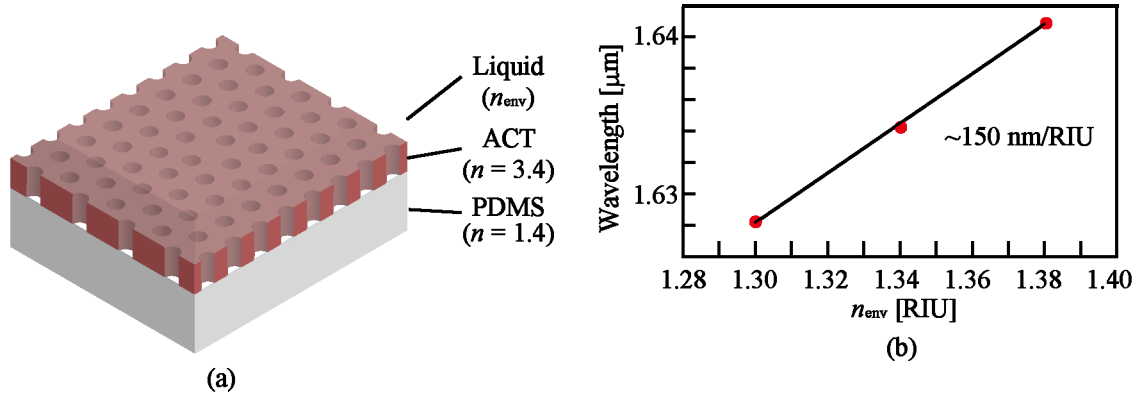
Fig. 2.8. Calculated sensitivity in the bonding structure. (a) Scheme of the model. (b) Wavelength shift for n_{env}.

2. 3. 4 **Sensitivity**

A can be acquired from dividing Δn by $\Delta\lambda$. Fig. 2.8 indicates the change in λ for the environmental n with the bonding structure, which is calculated by 3D FDTD written simulation. This simulation model is shown in Fig. 2.8(a). A red shift is observed along with the increase in n. A is calculated to be ~150 nm/RIU. This value is low compared to the previous air bridge structure, because one side of the slab does not contribute to the sensing. Additionally, the practical value of A is thought to be lower than the theoretical value due to the penetration of PDMS into the PC holes. However, the NS structure increases A by the modal confinement into the NS.

2. 3. 5 **Dynamic range**

The modal hopping of Δn is posited as the cause that limits the dynamic range. The Δn between the culture fluid and attached cell was found experimentally, and from references, to be around 0.02 RIU. This value is quite small compared to the index contrast of ~2 RIU between the active layer and the environment. Thus, the influence on the mode from Δn of a cell can be ignored. Fig. 2.9 shows the experimental spectra of 16 nanolasers for n_{env} in the range 1.30–1.38. These show monotonic $\Delta\lambda$ with the same mode, despite the Δn being larger than that for the cellular attachment. Furthermore, despite the broader range of Δn than that for a cell, modal instability does not arise. In one sense, if a structurally modified nanolaser has natural modal instability, then the Δn of a cell may exhibit modal hopping. However, the modal tolerance range for the structure is still large. For example, the wavelength bandwidth in the same mode when the diameter of the shifted holes forming the H0 cavity is changed is ~100 nm, whereas
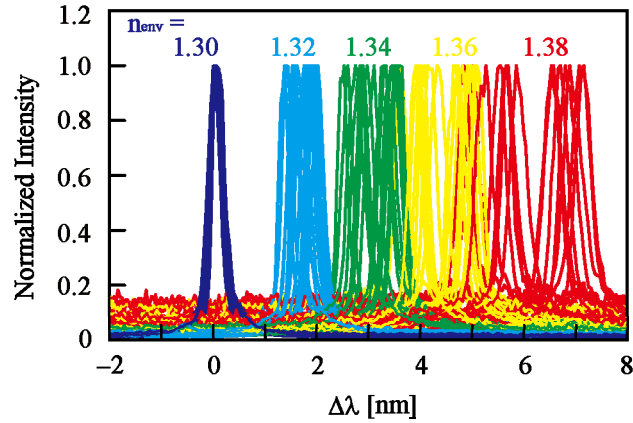
Fig. 2.9. Spectral shift for different n_{env} in 16 NS nanolasers. The environment is index liquid. The plot color indicates n_{env}.

the $\Delta\lambda$ from the Δn of the cell is ~2 nm. Thus, we can easily adjust the structure to the modally stable range, and the dynamic range of this method is sufficient for a cell imaging application.

2.3.6 **Noise**

In contrast to general optical microscopy, the method presented here senses only from λ information. Therefore, background noise can be ignored because the laser spectrum has a high intensity and a sharp linewidth in λ. However, the pumping operation is required to reduce the thermal invasiveness to the cell and the fluctuation in λ occurs from the TO effect with the pulse operation, which becomes the main source of noise in this method. Fortunately, in a cell imaging environment, the base of the culture fluids and cells is water. Because water has the inverse TO coefficient (-10^{-4} RIU/K) to one of the active layers (10^{-4} RIU/K), the cell imaging
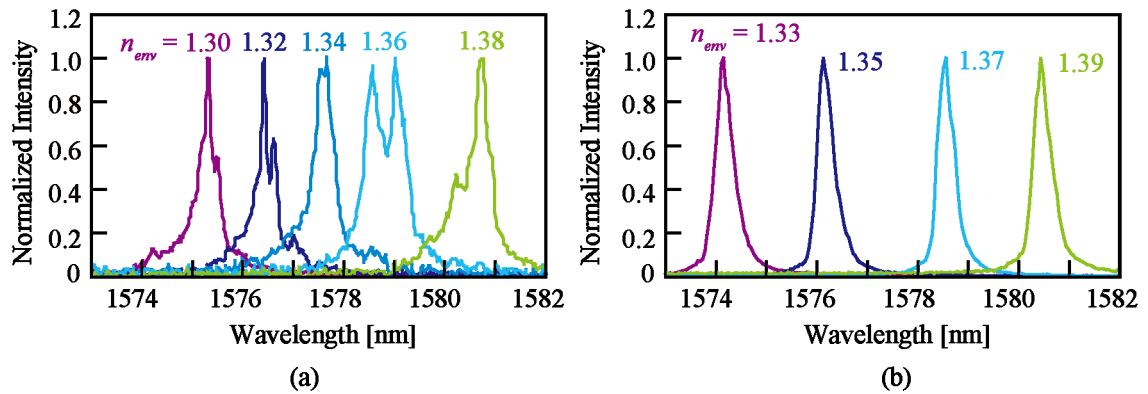
Fig. 2.10. Comparison of the spectra in index liquid and sugar water. (a) Index liquid. (b) Sugar water. The plot color indicates n_{env}.

noise is comparatively low. This noise is evaluated by the measured spectral line width. In this study, the experimental linewidth is of the order of less than a nanometer and is improved by introducing the NS structure, which balances the positive and negative TO effects. These details are described in Chap. 4. Similarly, the balancing of the TO effect reduces the fluctuation in λ. Further improvements, such as introducing another balancing structure or tuning the TO coefficient of the PDMS resin, are possible. Also note that the TO effect is important not only to the imaging but also to the measurement of the fundamental operation of the method. Fig. 2.10 indicates the spectra of different *n* solutions with an index liquid or sugar water. In the index liquid, there occurs a large TO effect, and a fluctuation in λ arises. If *A* is calculated from such a measurement, it will obviously be distorted. However, in the sugar water, sharp spectra are observed and an accurate *A* is expected. Thus, the measurement of the fundamental properties was conducted in the sugar water environment.

2. 3. 7 **Accuracy**

Δn was calculated from $\Delta\lambda$ and *A* in this method, as shown in equation 2.1. By introducing a fluctuation term for each variable, i.e., δn, $\delta\lambda$, and δA, we get equation 2.2. Here, δn is thought to not only be the fluctuation in the index shift but to also indicate the accuracy of this method. The absolute accuracy δn is then defined as equation 2.3.

$$\Delta n = \Delta\lambda \,/\, A \tag{2.1}$$

$$\Delta n + \delta n = (\Delta\lambda + \delta\lambda) \,/\, (A + \delta A) \tag{2.2}$$

$$\delta n = (\Delta\lambda + \delta\lambda) \,/\, (A + \delta A) - \Delta n \tag{2.3}$$

Here, $\Delta n + \delta n$ is the index shift acquired by this method, $\Delta\lambda + \delta\lambda$ is the measured wavelength shift, $\Delta A + \delta A$ is the measured sensitivity, and Δn is the index shift acquired from another method. With these, we can acquire the absolute accuracy of the measurements. The experimental results for these equations are described in Chap. 4. We calculated the theoretical δn for $\delta\lambda$ and δA. First, the influence of $\delta\lambda$ is discussed. The $\delta\lambda$ caused by the TO effect with the pulse pumping operation should be considered. However, the influence from the TO effect was not treated in this work due to its complexity, and left to actual experiment. Considering this, the spectral resolution of the spectroscopy (0.139 nm) became the main element in $\delta\lambda$. δn was calculated by $\delta\lambda$ (0.139 nm)/A (calculated value 150 nm/RIU) = ~10^{-4} RIU.

Second, the influence of δA is discussed. As mentioned with respect to the dynamic range, the optical mode has a strong stability. Thus, the stability of *A* is guaranteed, and δA can be

considered to be generally small. However, if Δn is large, nonlinearity arises from the fact that only one side of the slab contributes to the sensing. We calculated the equivalent index of the model of the three-layer asymmetric slab waveguide [2-19]. The parameter V of this model is defined as

$$V = k_0 \, n_{act} \, d \, \sqrt{\frac{n_{act}^2 - n_{pdms}^2}{n_{act}^2}} \qquad (2.4)$$

where k_0 is the propagation coefficient in vacuum, n_{act} is the index of the active layer, n_{pdms} is the index of the PDMS layer, and d is the thickness of the active layer. Assuming $k_0 = 2\pi/\lambda = 2\pi/(1.55 \times 10^{-4})$ rad/m, $n_{act} = 3.4$, $n_{pdms} = 1.4$, and $d = 180$ nm, V is calculated to be 2.26. The parameter b is numerically calculated with Eq. (2.5).

$$V = \frac{1}{\sqrt{1-b}} \left\{ \tan^{-1}\left(\frac{1}{\sqrt{1-b}}\right) + \tan^{-1}\left(\frac{\sqrt{b-a'}}{\sqrt{1-b}}\right) + N\pi \right\} \qquad (2.5)$$

$$a' = \frac{n_{pdms}^2 - n_{env}^2}{n_{act}^2 - n_{pdms}^2}$$

In Eq. (2.5), n_{env} is the index of the environment, a' is the term for the asymmetric nature, and $N\pi$ is the term for the multimodal nature. Assuming single-mode operation, b becomes a function of n_{env}. The equivalent index n_{eq} is calculated from Eq. (2.6) and (2.7) through the propagation coefficient β.

$$\beta = k_0 \sqrt{b \, (n_{act}^2 - n_{pdms}^2) \; + n_{pdms}^2} \qquad (2.6)$$

$$n_{eq} = \frac{\beta}{k_0} \qquad (2.7)$$

Because the measured index in this method is assumed to correspond to n_{eq}, the theoretically measured index n_{th} is defined as

$$n_{th} = n_{eq}\,(n_0) + (n_{env} - n_0) \left\{ \frac{n_{eq}\,(n_{max}) - n_{eq}\,(n_{min})}{n_{max} - n_{min}} \right\} \qquad (2.8)$$

where n_0 is the reference index, and n_{max} and n_{min} are the limits of the n used in the calculation of the sensitivity of n_{eq} to n_{env}. The right term presents the slope of n_{eq} to n_{env}, whereas $n_{eq} - n_0$ presents the theoretical error of the nonlinearity in A. Assuming the experimental range, $n_0 = 1.33$, $n_{min} = 1.33$, and $n_{max} = 1.39$, $n_{eq} - n_0$ is calculated as shown in Fig. 2.11. The maximum error from the nonlinearity in A is $\sim 4 \times 10^{-5}$ RIU in the experimental range. This error is thought to be resolved by treating A as a nonlinear term. From the discussion above, it is clear that the main cause limiting the accuracy of this method is $\delta\lambda$.
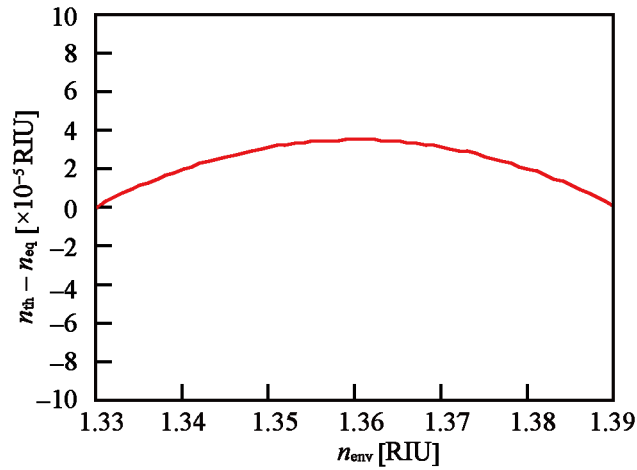
Fig. 2.11. Calculated error of the monitored index in this method. The error is caused by the asymmetry of the bonding structure.

2.3.8 **Frame rate**

To acquire a one-frame image requires the observation of all λ values in an array. The simplest way to do this is a measurement that involves an individual excitation and the scanning of the spot of the pumping light. The frame rate of this simple method is the product of the time for the single measurement and the scale of the integrated array. As mentioned above, another method involves simultaneous excitation and no scanning but rather identification from the λ of the individual nanolasers. In this way, the frame rate is improved because it is only dependent on the time taken for a single measurement. The time for a single measurement is divided into the exposure time in the detector, the data translation time, and the time it takes to save the data. The exposure time depends on the worst lasing intensity of an array and is practically set to 0.5–2.0 s with a spectrometer Roper SP2760-3, and an InGaAs array detector Roper OMA-V1024. The time for data translation and saving is ~0.7 s. Therefore, the total time for a single measurement is ~1 s or more. Because the exposure time can be potentially shortened to < 0.1 s for a nanolaser with good properties, and the data translation is performed using a slow USB port, the theoretical frame rate is thought to be suitable for real time observations. In this thesis, simultaneous measurement was achieved by controlling λ, which is described in detail in Chap. 3, and the automatic measurement and data processing systems, which are described in detail in Chap. 4.

Reference

[2-1] K. A. Tetz, L. Pang, and Y. Fainman, "High-resolution surface plasmon resonance sensor based on linewidth-optimized nanohole array transmittance", *Opt. Lett.*, vol. 31, no. 10, pp. 1528-1530, 2006.

[2-2] K. J. Moh, X. C. Yuan, J. Bu, S. W. Zhu and B. Z. Gao, "Surface plasmon resonance imaging of cell substrate contacts with radially polarized beams", *Opt. Express*, vol. 16, no. 25, pp. 20754–20741, 2008.

[2-3] S. Bassnett, "On the mechanism of organelle degradation in the vertebrate lens", *Experimental Eye Research*, vol. 88, no. 2, pp. 133–139, 2009.

[2-4] Y. Fang, "Non-invasive optical biosensor for probing cell signaling", *Sensors*, vol. 7, no. 10, pp. 2316–2329, 2007.

[2-5] H. Zhao, P. H. Brown, and P. Schuck, "On the distribution of protein refractive index increments", *Biophysical J.*, vol. 100, no. 9, pp.2309–2317, 2011.

[2-6] T. Strother, "Protein concentration prediction in cell cultures: the next stage in NIR bioprocess analysis", *Spectroscopy Europe*, vol. 23, no. 3, pp.18-21, 2011.

[2-7] K. Nozaki, S. Kita and T. Baba, "Room temperature continuous wave operation and controlled spontaneous emission in ultrasmall photonic crystal nanolaser", *Opt. Express*, vol. 15, no. 12, pp. 7506-7514, 2007.

[2-8] B. Alberts, A. Johnson, J. Lewis, M. Raff, K. Roberts, and P. Walter "Molecular biology of the cell (5th ed.)", *Newton Press*, 2010.

[2-9] G. Stabler, M. G. Somekh, and C. W. See, "High-resolution wide-field surface plasmon microscopy", *Journal of Microscopy*, vol. 214, pp. 328–333, 2004.

[2-10] K.F. Giebel, C. Bechinger, S. Herminghaus, M. Riedel,P. Leiderer, U. Weiland, and M. Bastmeyer, "Imaging of cell/substrate contacts of living cells with surface plasmon resonance microscopy", *Biophysical J.*, vol. 76, pp. 509–516, 1999.

[2-11] I. H. Goldverg, M. Rabinowitz, and E. Reichi, "Basis of actinomycin action, I. DNA binding and inhibition of RNA-polymerase synthetic reactions by actionomycin", *Biochemistry*, vol. 48, no. 12 , 2094–2101, 1962.

[2-12] M. Narimatsu, S. Kita, H. Abe and T. Baba, Enhancement of vertical emission in photonic crystal nanolasers," *Appl. Phys. Lett.*, vol. 100, no. 12, pp. 121117, 2012.

[2-13] S. Kita, S. Otsuka, S. Hachuda, T. Endo, Y. Imai, Y. Nishijima, H. Misawa and T. Baba, "Photonic crystal nanolaser bio-sensors", *IEICE Trans. Electron.*, vol. E95-C, no. 2, pp. 188-198, 2012.

[2-14] K. Nozaki, S. Kita and T. Baba, "Room temperature continuous wave operation and controlled spontaneous emission in ultrasmall photonic crystal nanolaser", *Opt. Express*, vol. 15, no. 12, pp. 7506-7514, 2007.

[2-15] S. Kita, S. Otsuka, S. Hachuda, T. Endo, Y. Imai, Y. Nishijima, H. Misawa, and T. Baba, "Super-sensitivity in label-free protein sensing using nanoslot nanolaser", *Opt. Exp*ress*, vol. 19, no. 18, pp.17683–17690, 2011.

[2-16] S. Hachuda, S. Otsuka, S. Kita, T. Isono, M. Narimatsu, K. Watanabe, Y. Goshima and T. Baba, "Selective detection of sub-atto-molar streptavidin in 1013-fold impure sample using photonic crystal nanolaser sensors," *Opt. Express*, vol. 21, no. 10, pp. 12815–12821,2013.

[2-17] T. Watanabe, H. Abe, Y. Nishijima and T. Baba, "Array integration of thousands of photonic crystal nanolasers," *Appl. Phys. Lett.,* vol. 104, no. 12, pp. 121108, 2014.

[2-18] H. Abe, M. Narimatsu, T. Watanabe, T. Furumoto, Y. Yokouchi, Y. Nishijima, S. Kita, A. Tomitaka, S. Ota, Y. Takemura and T. Baba, "Living-cell imaging using a photonic crystal nanolaser array," *Opt. Express*, vol. 23, no. 13, pp. 17056-17066, 2015.

[2-19] Y. Kokubu, "Lightwave engineering", *CRC Press*, 2012.

Chapter 3
Nanolaser Device

3. 1 **Design**

We fabricated the nanolaser device by transcribing its pattern onto a GaInAsP semiconductor slab with EB lithography. It is well-known that such lithography patterns can control the optical confinement of the PBG, the Q factor, the resonant wavelength, the angle of the emission light, and the TO effect. In this study, we followed the pattern design principles of previous publications [3-35, -6], but improved them for the array application by accounting for the following:

1. Independent operation of nanolasers.
2. Control of the resonant wavelength.
3. Single-mode operation.
4. Lasing yield in the array.
5. Inhibition of wavelength instability with the TO effect in the new structure nanolaser.

Incorporation of these features is necessary for the intended imaging applications. The EB exposure system offers two scanning methods, namely vector and raster. The vector method was primarily employed because of the superior accuracy of its exposure time and figures and its higher throughput. We prepared the computer aided design (CAD) data for the vector scanning method using a script we wrote specifically for this work script.

3. 1. 1 **Nanolaser**

Fig. 3.1 shows a schematic of the CAD image of a single nanolaser. The x-direction shift s_x forms an H0-type cavity [3-4]. The triangle shift $s_{triangle}$ orients the laser emission toward the vertical direction, which improves the signal intensity. Table 3.1 indicates the parameters used for the nanolaser CAD. The ratio between the diameter of holes $2r$ and lattice constant a was adjusted to form a fiber Bragg grating (FBG). a and s_x were set to calibrate the band of the FBG

Fig. 3.1. CAD layout of PC nanolaser, in which the black region is exposed.
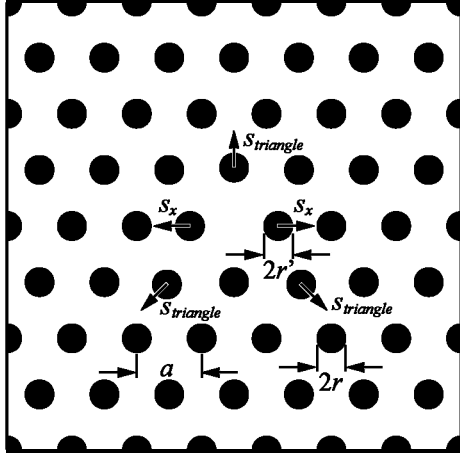
Table 3.1 CAD parameters for the PC nanolaser.

a [nm]	500
$2r$ [nm]	250
s_x [nm]	80
$s_{triangle}$ [nm]	20
$2r$' [nm]	$2r - 55 \sim 2r + 20$

(a)

(b)
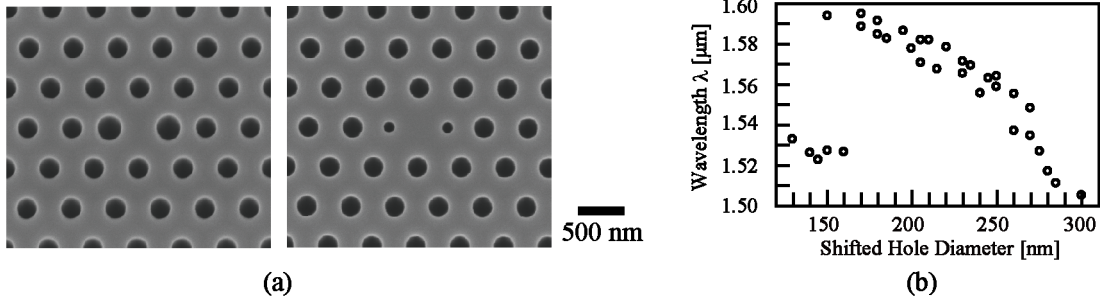
Fig. 3.2. Control of resonant wavelength using changes in the shifted hole diameters. (a) SEM images of the fabricated devices. (b) Spectral peak λ for various shifted hole diameters. [3-15]

at the emission band of the active material and to maximize the Q factor, respectively. λ was controlled by the varying $2r$. The $s_{triangle}$ value had to account for a trade-off between the signal intensity and the multi-mode emission, and was set in a range to achieve stable emission for single-mode operation. These parameters were for operation in an aqueous environment. However, the fabricated figure did not correspond exactly to the CAD design parameters because of the optical proximity effect (OPE); e.g., the hole of diameter 230 nm in the design became 250 nm in practice. In the PC nanolaser, changes in $2r$ affect λ and the emission mode. The target value of $2r$ for independent operation, which is explained below, the operation wavelength, and single-mode operation was 250 nm. We fabricated the nanolaser with a range of $2r$ in CAD with a range of dose time for compensate fabrication error, and used the device which good lasing property in experiments.

As discussed above, controlling λ of a nanolaser adds important imaging features. However,

with previous control methods, the OPE prevented the monotonic change in λ. We tried exerting control over this by using the diameter of the shifted holes, 2*r'*. With this method, because the OPE enhances the change in λ, a monotonic change was expected. Fig. 3.2 shows the dependence of λ on 2*r'*. Neglecting the modal hopping at 2*r'* < 160 nm, λ changes monotonically from 1.59 to 1.51 μm with increasing 2*r'*. Thus, we can tune the λ in an array by designing 2*r'* to have a wide range. However, for conditions close to the modal hopping region, the single-mode operation became unstable, such that these conditions were not suitable for identification by λ. Fig. 3.3 indicates the spectra of the nanolaser array for the controlled 2*r'* when the area of the pumping light spot was changed. The data for the smaller 2*r'* condition, as shown in Fig. 3.3(a) and (b), indicate the match of the spectra between the large area excitation and the small area excitation. In contrast, the data for the larger 2*r'* condition, as shown in Fig. 3.3(c) and (d), indicate the mismatch of the boundary and the occurrence of modal hopping for different sizes of the pumping light spot. In such unstable conditions, the identification of each nanolaser from the multi-peak spectra is difficult because of the mismatch with the reference λ obtained by individual measurement. Evaluating the stability of these conditions should require
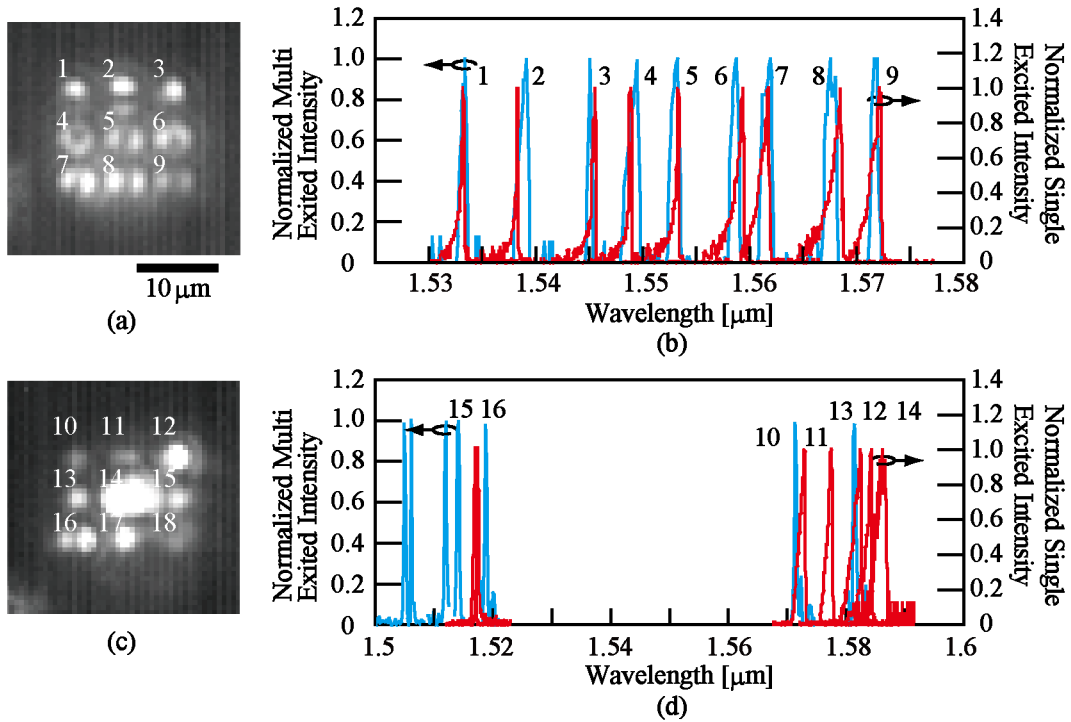
Fig. 3.3.   Spectra for different 2*r'* and sizes of the pumping light spot. (a), (c) Near-field pattern of the emission from nine nanolasers. (b), (d) Spectra. The color of the spectra indicates the spot size; blue is ~20 μm and red is ~3 μm. Numbers 1–18 indicate 2*r'* for 2*r* + 60 ~ 2*r* − 110 nm (in steps of 10 nm).
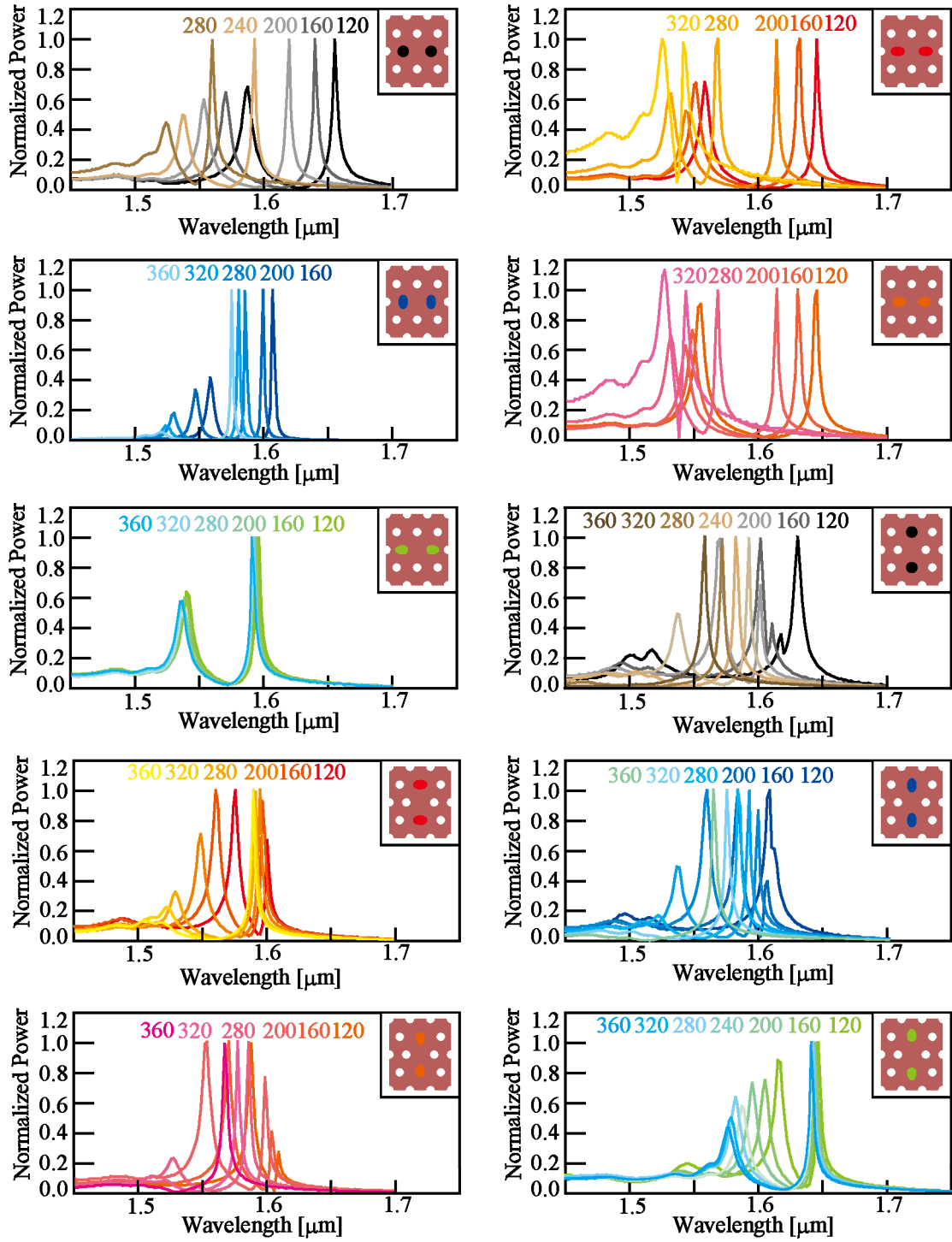
Fig. 3.4. Calculated spectra for the transformations of the four central holes with Fullwave. The top right panel in each graph shows the transformed hole, and the color of the holes indicates the changed radius in four directions: black, red, blue, orange, and green indicate all directions, horizontal, vertical, inside of the cavity, and outside of the cavity, respectively.
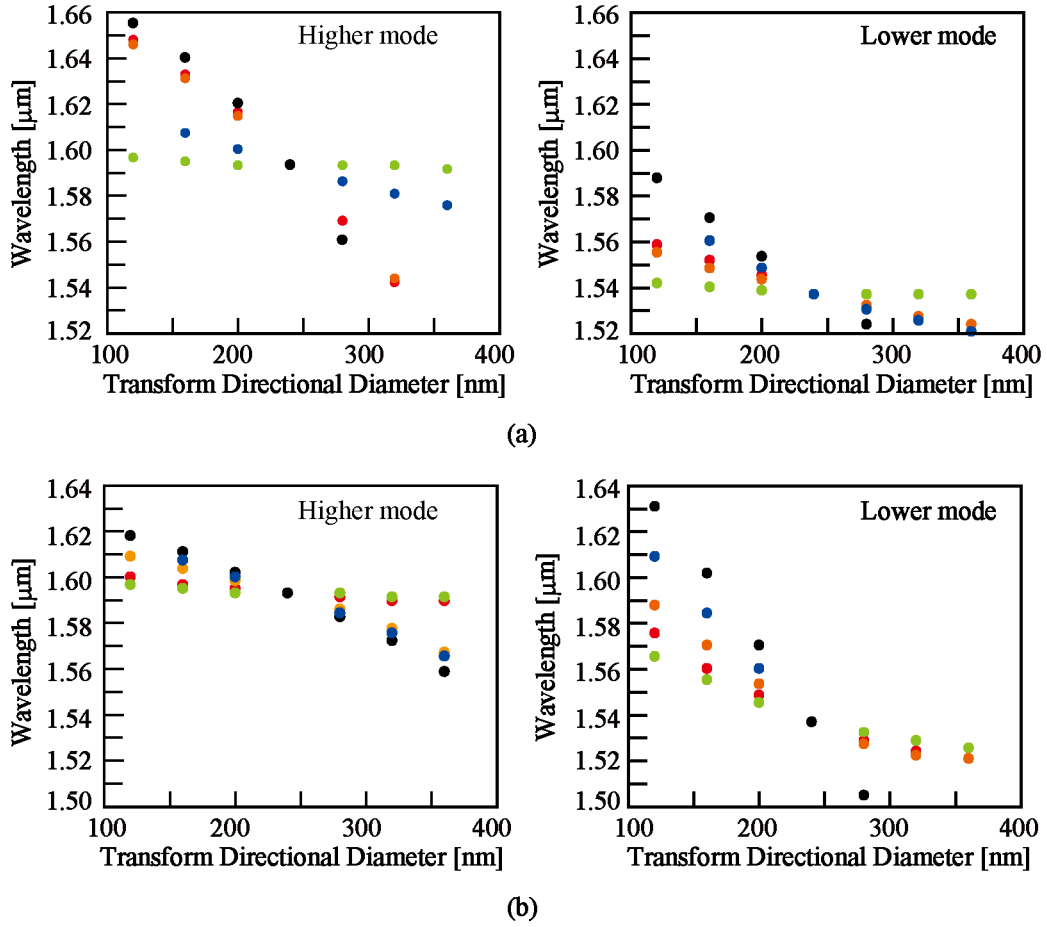
Fig. 3.5. Wavelengths of the spectral peaks in Fig. 3.4. The color of the plots indicates the changed radius in the four directions, which are the same as for Fig. 3.4. (a) Data for the shifted holes. (b) Data for the non-shifted holes.

the rate equation for each mode and consider the overlap between the pumping light spot and the modal distribution. However, such complex calculation requires considerable work and the limited controllability of λ is still good enough to distinguishing each nanolaser from its neighbors. Therefore, the experimentally stable condition $2r' > 2r - 25$ nm was mainly used in this study.

For the advanced control of λ and stability of the single-mode operation, we calculated the spectra for various transformations of the four central holes in the H0 cavity. Fig. 3.4 shows the resonant spectra for these as calculated by FDTD simulations with Fullwave. These spectra indicate two resonant modes. The higher wavelength mode is the one primarily desired, whereas the lower mode is the unwanted one, for which modal hopping or the multi-mode operation occurs. These basic parameters, such as the Q factor and the modal distribution, have been reported previously [3-5]. Here, we searched for an effective position for the four holes for

controlling λ while maintaining modal stability. The shifted holes forming the H0 cavity are more effective for changing the higher mode than the non-shifted holes, whereas the non-shifted holes are effective for changing the lower resonant mode. Fig. 3.5 shows the spectral peaks in Fig. 3.4. These show that the effects for the radius change inside of the cavity were larger than those for the other directions (namely, horizontal, vertical, and outside of the cavity). From these results, in this study, the figures and coordinates of the non-shifted holes were fixed to stabilize the single-mode operation. We also tried to control the ellipse holes, but the fabrication error (~10 nm in λ) obscured the change in the ellipse hole sizes. Thus, only $2r'$ was used for the control in this study. With respect to the resolution in the CAD design, if only modest control was needed, we used an additional exposure of slightly smaller holes and controlled them with the exposure conditions of the additional holes.

3. 1. 2 **Nanoslot nanolaser**

We fabricated an NS nanolaser to reduce the fluctuation in λ caused by the TO effect of the pulse operation used. The structure of the NS was basically the same as that in previous reports [3-5]. Because the PDMS has the same order of TO coefficient (-0.5×10^{-4} RIU/K) as water (-1×10^{-4} RIU/K), a similar improvement was expected. The modification points included the removal of the vertical direction shift s_y [3-5] for single-mode operation and the additional exposure of the NS pattern for improvement in an array. Fig. 3.6 shows the designed CAD image of the NS nanolaser, and Table 3.2 shows the parameters of the NS structure. $2r$ was set to stabilize the emission from the experimental feedback. S_x was set to be optimized to the
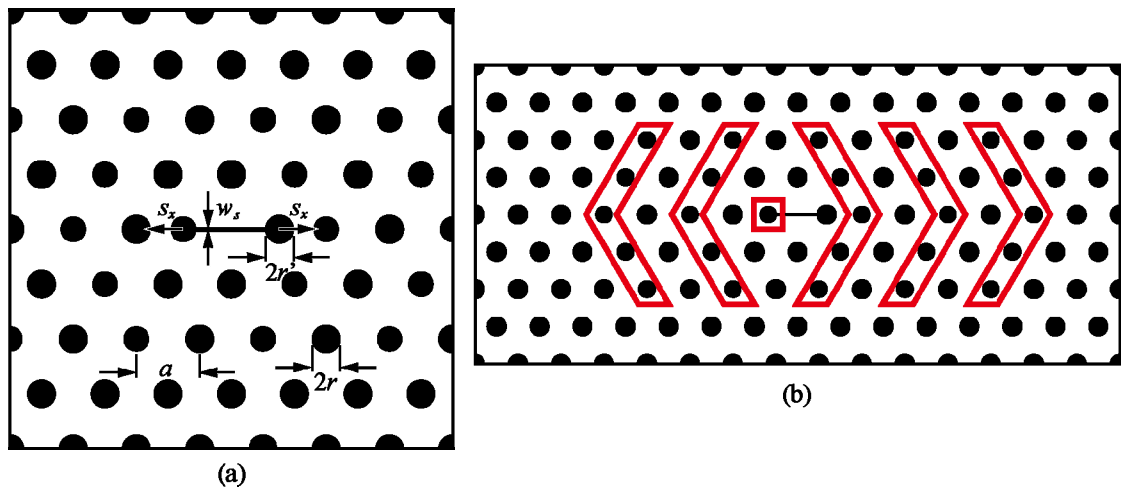
Fig. 3.6. CAD layout of the NS nanolaser. (a) The cavity. (b) The distribution of the modifications to orient the laser emission toward the vertical direction.

44

Table 3.2. CAD parameters for the NS nanolaser.

a [nm]	500
$2r$ [nm]	$200 \sim 230$
s_x [nm]	120
E_y modulation [nm]	-30
$2r'$ [nm]	$2r - 25 \sim 2r$
w_s [nm]	$30 + 10$ (adding)

maximum Q factor. The width of the NS, W_s, was set to fabricate a narrow NS with the NS yield in an array. Because the narrowness of the NS increases the optical confinement in the NS, a narrower width is desired; however, the yield of the NS is influenced by the instability of the OPE. Thus, choosing W_s involves a trade-off between the narrowness and the yield. To improve the NS yield, the additional exposure of the slot pattern was designed with a width of 10 nm and a dose time of 0.1 μs. The diameter of the holes with modal E_y distribution were modified to orient the laser emission toward the vertical direction. These modified holes are shown in Fig. 3.6(b) [3-9].

3. 1. 3 Nanolaser array

3. 1. 3. 1 Layout

Figure 3.7 shows the CAD layout of the whole pattern in a single field in the exposure system. In the bonding structure, shown in Fig. 3.7(a), the PC and an identifying code are aligned. The nanolaser array is formed in a uniform PC. The cavity is aligned into a 2D square lattice. The pitch of the PC nanolasers was determined by the experimental results. For the large-scale integration, the pitch was 5 μm because of the limitations of the accuracy of the piezoelectric micrometer for automatic measurement. For the NS nanolasers, the pitch was 10 μm because of the large distribution of the weak component in the NS mode. For handy calibration of the light alignment, the pitch was 2.5 μm because of the size of the pumping light spot. The margin of the PC was aligned to create the PBG at the four sides of the cavities. The margin length was 10 μm in the simple nanolaser, or 20 μm in the S_x direction and 10 μm in the other direction in the NS nanolaser. In the air bridge structure shown in Fig. 3.7(c), the PC, the identifying code, and the trench pattern are aligned. The trench helps the penetration of the etchant in the wet etching, and acts as a dummy pattern to make the OPE uniform. The trench
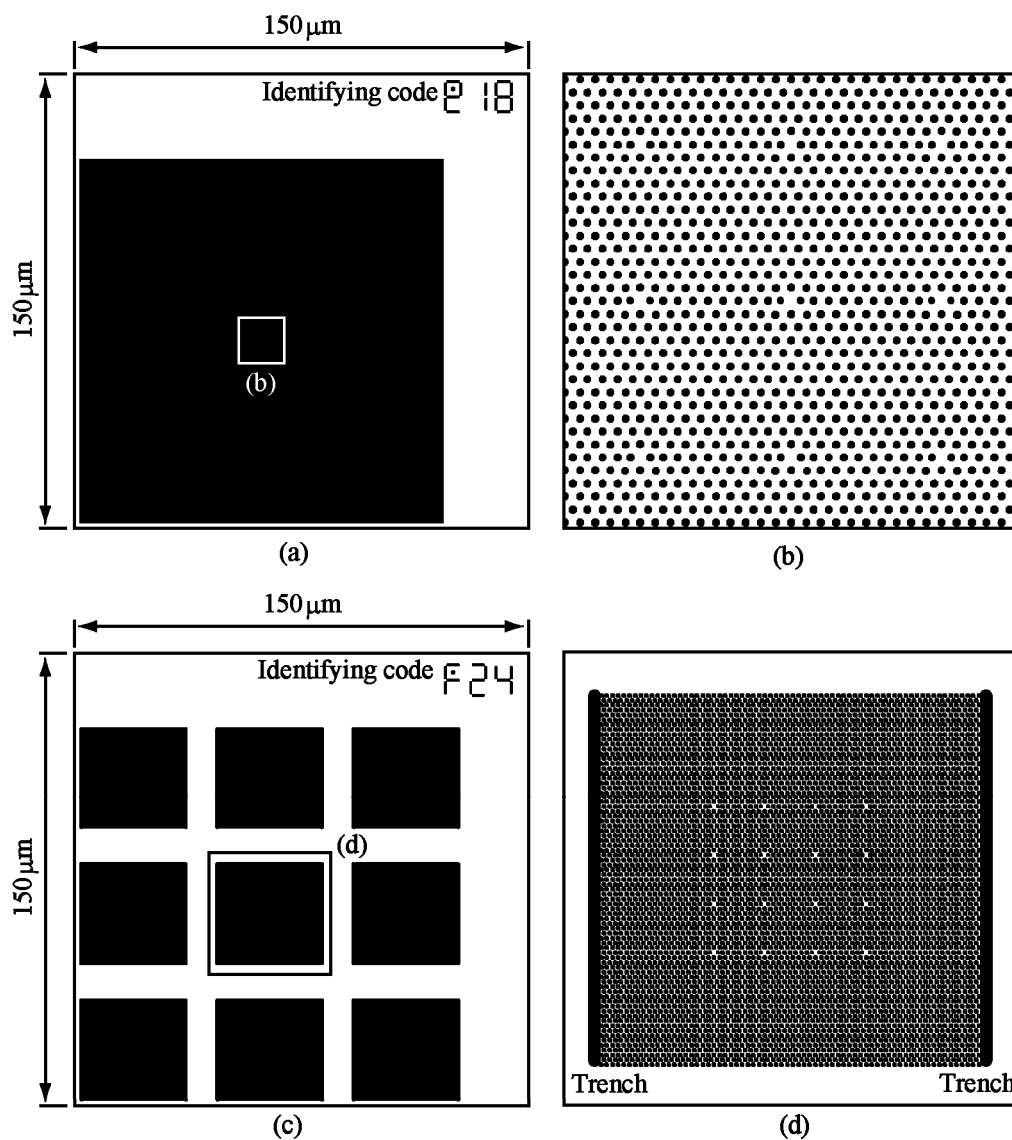
Fig. 3.7. CAD layout of the array. (a) Bonding structure. (b) Magnified image of (a). (c) Air bridge structure. (d) Magnified image of (c).

pattern was also aligned in the bonding structure in the early steps of this study to suppress the distortion of the slab caused by unsteady bonding.

3. 1. 3. 2 **Isolation of individual nanolasers**

Initially, when fabricating the nanolaser array, coupling between the individual nanolasers arose, which restricted the devices' ability to image pixel. Various coupling patterns were observed, including one that involved the matching of λ between nanolasers and another that involved one-way coupling from a longer λ to a shorter λ. We tried dividing the λ between the

nanolasers for a given layout and using a pitch large enough to avoid overlap of the modal distributions, but these techniques did not suppress the coupling. Therefore, we carefully compared the emission properties with the condition of the nanolaser array and discovered that modal selection by the diameter of the PC holes could suppress the coupling. Fig. 3.8 shows the dependence of λ on $2r$ and gives examples of the spectra with and without the coupling. Fig. 3.8(a) and (b) show emission of 9 nanolasers and 9 spectral peaks, while Fig. 3.8(c) and (d) show the emission of 9 nanolasers but only 1 spectral peak. When $2r$ is changed, a clear
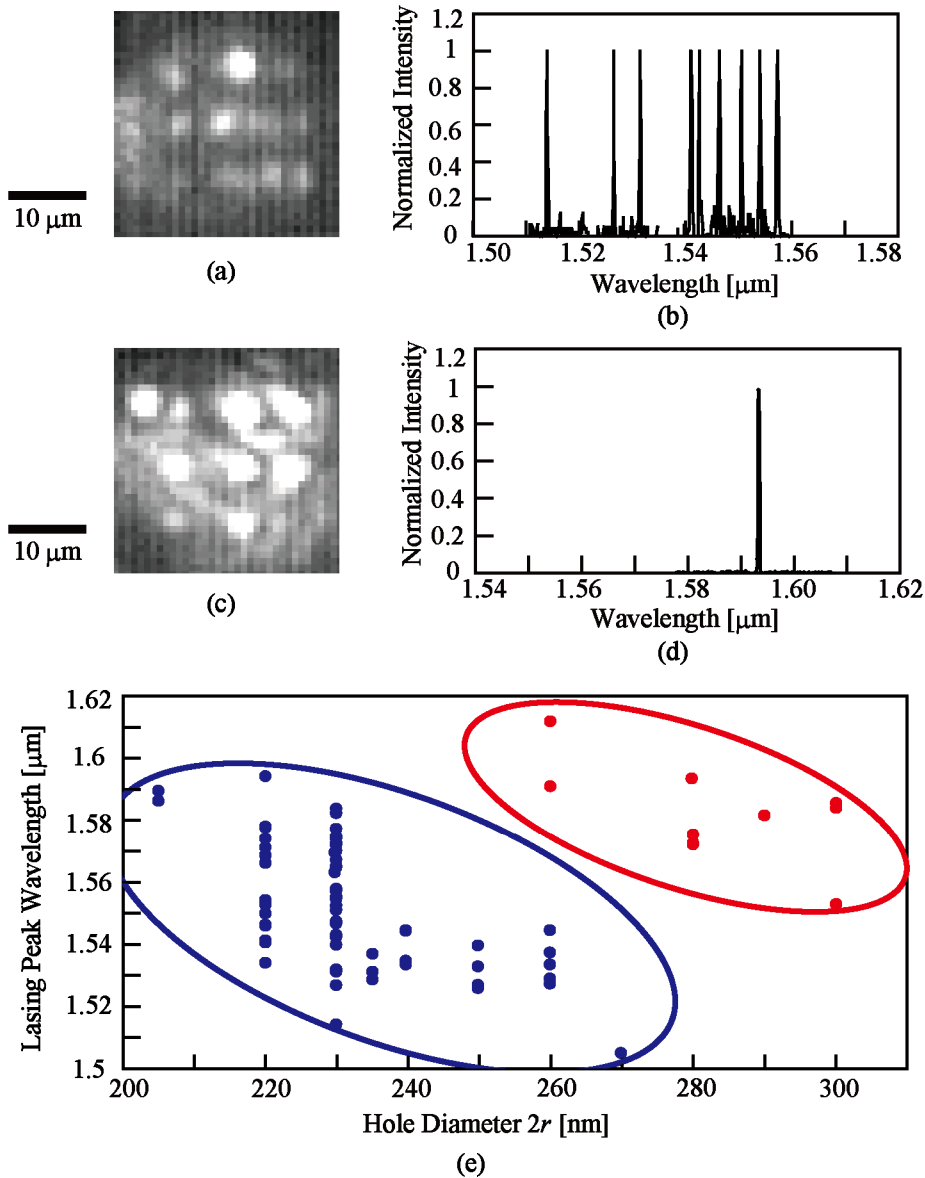
Fig. 3.8. Nanolaser coupling control using $2r$. (a), (b) Near-field pattern and spectra for 9 nanolasers with $2r$ = 230 nm. (c), (d) Near-field pattern and spectra for 9 nanolasers with $2r$ = 280 nm. (e) Dependence of λ on $2r$: multi-peak operation is shown in blue, and single in red.

difference with or without the coupling is apparent. Fig. 3.8(e) shows that λ shifts to shorter wavelengths with an increase in $2r$, and that mode hopping occurs at $2r = 260$ nm. The difference in coupling corresponds to the mode; the samples in blue indicate multi-peak operation as per Fig. 3.8(a) and (b), whereas the ones in red indicate single-peak operation as per Fig. 3.8(c) and (d). Therefore, we concluded that we can suppress the unwanted coupling by controlling the size of $2r$.

3.2 **Fabrication**

3.2.1 **Overview**

Fig. 3.9 shows the fabrication process workflow. We used two workflows to make the bonding device (α) and the air bridge device (β). Each structure was made with high-throughput fabrication over a large area. For both processes, the resist mask was first coated onto the 1.55-μm-bandwidth GaInAsP/InP wafer. The CAD pattern was then transcribed by EB lithography and hydrogen-iodide (HI) inductive coupled plasma (ICP) dry etching. For the air bridge device, the InP sacrifice layer was then removed by HCl wet etching to complete the process. In contrast, for the bonding device, the holes were then filled with silica, the surface InP layer removed by HCl wet etching, the GaInAsP layer with PC patterns bonded, and finally, the InP layer removed. We also used a trimming process to tune the wavelength of the arbitrary nanolaser. By pumping in a dilute HCl environment, the nanolaser holes were finally revealed. The technical details of each process are described below. In this study, the air bridge fabrication process corresponds closely to the work described in previous reports [3-35, −6], but our bonding process and our post-process trimming are considerably different.

3.2.2 **Laser wafer**

We prepared a commercially available GaInAsP/InP single quantum well (SQW) wafer with a photoluminescence peak of around 1.55 μm. The wafer was epitaxially grown with metal organic chemical vapor deposition by the Furukawa Elec. Co. We used two types of wafer, a #1: F1207380 and M8-11111. Fig. 3.10(a) and (b) shows the composition of the wafers. The InP capping layer and the GaInAsP contact layer were removed in the preparation process. The InP cladding layer functions as the sacrificed layer in the ICP etching process and forms the mold for the embedded silica. The GaInAsP quantum well was used as the active material in the laser. Fig. 3.10(c) shows the band structure of the active layer. This double hetero structure was set to confine light into the layer and to ensure that the carriers generated in the SCH layer moved into
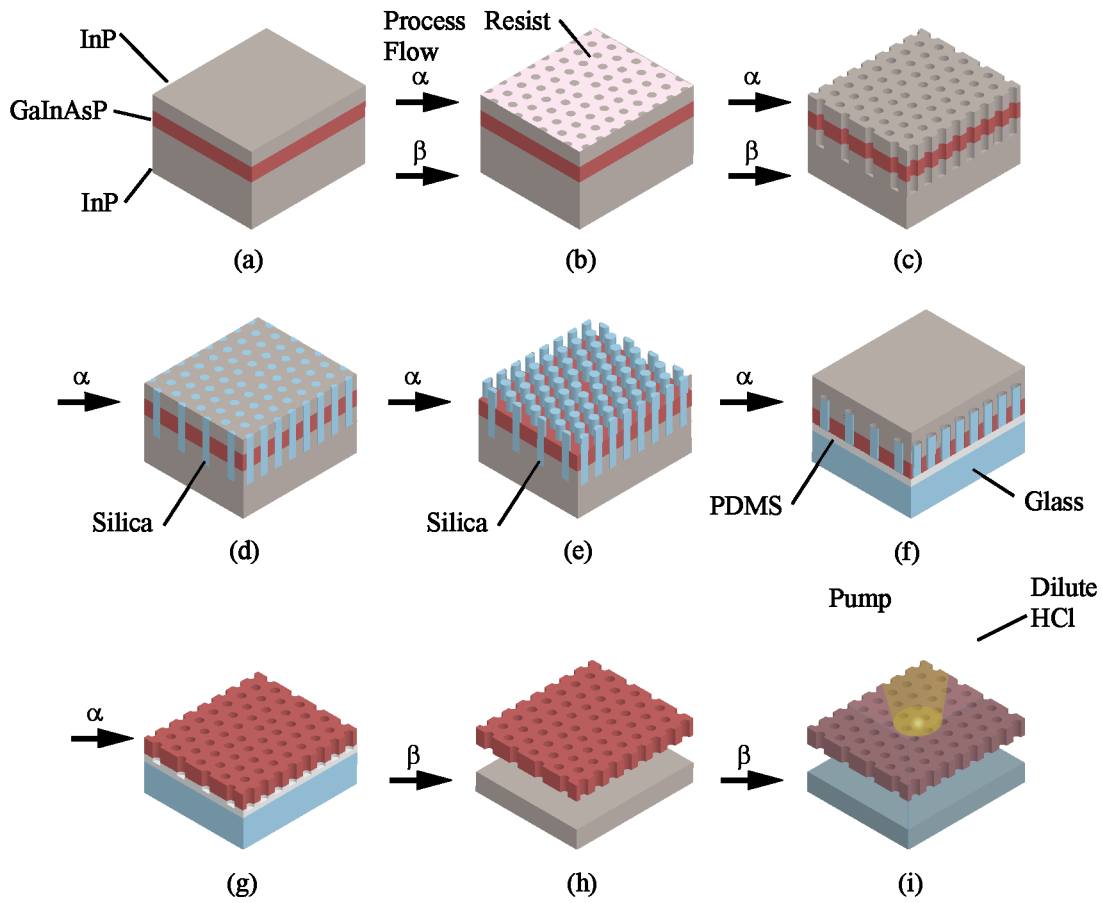
Fig. 3.9. Fabrication process workflow. (a) GaInAsP/InP wafer. (b) EB lithography. (c) HI ICP etching. (d) Silica deposition into holes. (e) HCl wet etching. (f) Bonding using PDMS resin. (g) HCl and HF wet etching. (h) HCl wet etching. (g) HCl trimming. α indicates steps for the bonding device, whereas β indicates steps for the air bridge device.
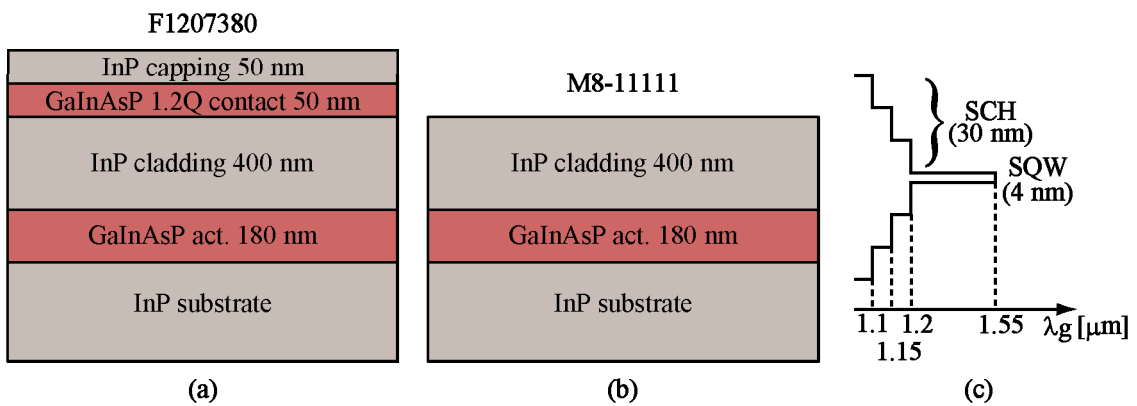
Fig. 3.10. Composition of GaInAsP/InP wafer; (a), (b) are the wafer structures, and (c) is the band structure of the active layer.

the SQW faster than the saturation time of the carrier by stimulated emission. With respect to cell compatibility, the infrared bandwidth had low invasiveness due to the reduction of the absorption of the cellular component. GaInAsP is not used in cell experiments, generally; thus, there was a possibility of its cellular toxicity being important. However, we confirmed that cells could be cultured and attached directly onto the GaInAsP, so the cell toxicity for this device is thought to be low enough for it to be used for cell imaging.

3. 2. 3 EB lithography

Removal of unwanted layers of the wafer

In the F1207380 wafer, the InP capping layer and the GaInAsP contact layer were not required. Therefore, the InP layer was removed by HCl wet etching for 10 s, with an etching rate of ~1 μm/min, and the GaInAsP layer was removed by exposing to Piranha solution for 2 min, with an etching rate of 100 nm/min. Table 3.3 shows the etching conditions for each removal. In the air bridge device fabrication process, to improve the vertical etching in the HI ICP etching step, the InP cladding layer was thinned by HCl wet etching for ~10 s. In the bonding device process, because the cladding layer functions as a mold for silica deposition, this thinning was not performed. For the entire wet etching process described below, the etchant was prepared with a measuring cylinder and the process took place in a dedicated beaker. For the HCl wet etching, the temperature of the etchant was controlled by a thermometer and iced water. After each rinse, any water drops on the wafer were blown off by a blower and evaporated by a halogen heater.

Table 3.3. Wet etching conditions.

Subject material	InP	GaInAsP
Etchant	$HCl : H_2O = 4 : 1$	$H_2SO4 : H_2O_2 : H_2O = 3 : 1 : 1$
Temperature	3°C	20°C
Rinse	Ultrapure water 10 s + 1 min	Ultrapure water 1 min + 1 min

Treatment of the wafer surface

Before coating the resist onto the wafer, any extraneous matter was cleaned and the wafer surface was treated to attach the resist. In previous research, we developed a method for this treatment, so that a hydrophobized surface could be attached to the resist. When the surface condition was good enough to attach to, the wafer was boiled in methylene chloride for 20 min at 130 °C, after which the beaker with the wafer was washed with acetone and then methanol, three times. Then, the wafer was boiled in methanol and dried under halogen light. If the upper

surface of the wafer flipped the resist, the wafer was briefly dipped into HCl etchant under the same conditions that are given in Table 3.2.1. The dipping was repeated until the wafer surface was fully hydrophobized and flipped a water droplet. After each treatment, subsequent processes were carried out immediately to prevent excrescences or variation in the surface condition.

Resist coating onto the wafer

The positive EB resist ZEP 520A (Zeon) was coated onto the wafer using a spin coater. The coating settings were 1000 rpm, 4 s and 2800 rpm, 40 s. The resist was heated by a hotplate at 180° for 3 min as a pre-bake.

EB exposure

We used two EB pattern exposure systems (ELS-7500 and ELS-7500EX, ELIONIX). The exposure settings are listed in Table 3.4. Two scanning methods were used. The CAD data for the vector scanning and raster scanning were created from a script program or conversion of illustration data, respectively. While raster scanning was employed for easy preparation of CAD data, vector scanning was employed for the fine grid partition and the controllability of the dose time for each single structure, such as a circle or square. The range of the dose time was set to deal with the instability of the EB and the change in the radius of the holes by the OPE. The probe current was set with respect to the range of the dose time.

Table 3.4. EB exposure settings.

Scanning method	Vector	Raster
Grid partition	60000×60000 dot^2	20000×20000 dot^2
Field size	$150 \ \mu m^2$	
Accelaration voltage	$50 \ kV$	
Probe current	$15 \ pA$	$50 \ pA$
Dose Time	$0.3 - 0.7 \ \mu s$	$0.8 - 2.4 \ \mu s$

Development

The resist with the wafer was immersed into a beaker of ZED-N50 (Zeon) developer for 1 min, and then a beaker of ZMD-B (Zeon) rinse for 15 s + 1 min. During the development, the wafer was carefully manipulated with tweezers. To dry off the rinsing solution, any droplets attached to the reverse of the wafer were absorbed by a pressed filter paper. Subsequently, the resist was heated in an oven at 130 °C for 1 h, as a post-bake.

3. 2. 4 **ICP etching**

The resist pattern was transcribed to the GaInAsP active layer using an ICP system, RIE-200ip (Samco). Before etching, any matter remaining from the previous etching in the chamber was removed by O_2 plasma ashing, and the etching recipe was executed without the wafer to stabilize the HI plasma condition. The wafer was set onto the InP stage in contact with vacuum grease. Then, the HI plasma etched the InP and GaInAsP layers along with the developed resist mask pattern. After transcription, the remaining resist and reaction products were removed by O_2 plasma ashing using another ICP system, RIE-10ip (Samco). The ICP etching settings are listed in Table 3.5. Fig 3.11 shows SEM images of the fabricated devices. This shows the transpiration of CAD pattern.

3. 2. 5 **Surface treatment and air bridge formation**

This section describes the air bridge device fabrication process following ICP etching. The wafer was treated to remove the reaction product, and an air bridge structure was formed. This procedure was as follows:

(1) Immersion in methylene chloride for 20 min at 130 °C; substitution of acetone and methanol, three times in each.

(2) Immersion in 2.4% ammonium sulfide solution for 30 min at room temperature; rinsing in ultrapure water, 20 times.

(3) Immersion in H_2SO_4 for 5 min at room temperature; rinsing in ultrapure water for 1 min + 1 min.

(4) O_2 plasma ashing under the conditions listed in Table 3.5 #4.

(5) Immersion in HF solution for 10 min at room temperature; rinsing in ultrapure water for 15 s + 1 min.

(6) Cleavage to divide each patterned area for disposability.

(7) HCl etching using the conditions listed in Table 3.3 for 20 min to form an air bridge structure. If this etching was not sufficient, the etching time was increased by 5 min.

(8) Oxidization of the wafer surface by heating in an oven for 1 h at 180 °C.

3. 2. 6 **Silica embedding**

This section describes the bonding device fabrication process following ICP etching. The wafer was treated to remove the reaction product, and the holes were filled with silica. The

silica was formed by a sol-gel process using tetraethyl orthosilicate (TEOS). This procedure was as follows:

Table 3.5. ICP etching settings.

Procedure		Temperature [°C]	Bias power [W]	ICP power [W]	Gas pressure [Pa]	Gas flow [sccm]	Time [min]
#1	O₂ ashing	70	0	500	5	100	10
#2	HI etching (w/o wafer)	70	300	100	0.28	0.2	5
#3	HI etching (w wafer)	70	300	100	0.28	0.2	10
#4	O₂ ashing	-	300	100	30	50	1

(a) 10 μm   (b) 10 μm

(c) 500 nm   (d) 500 nm
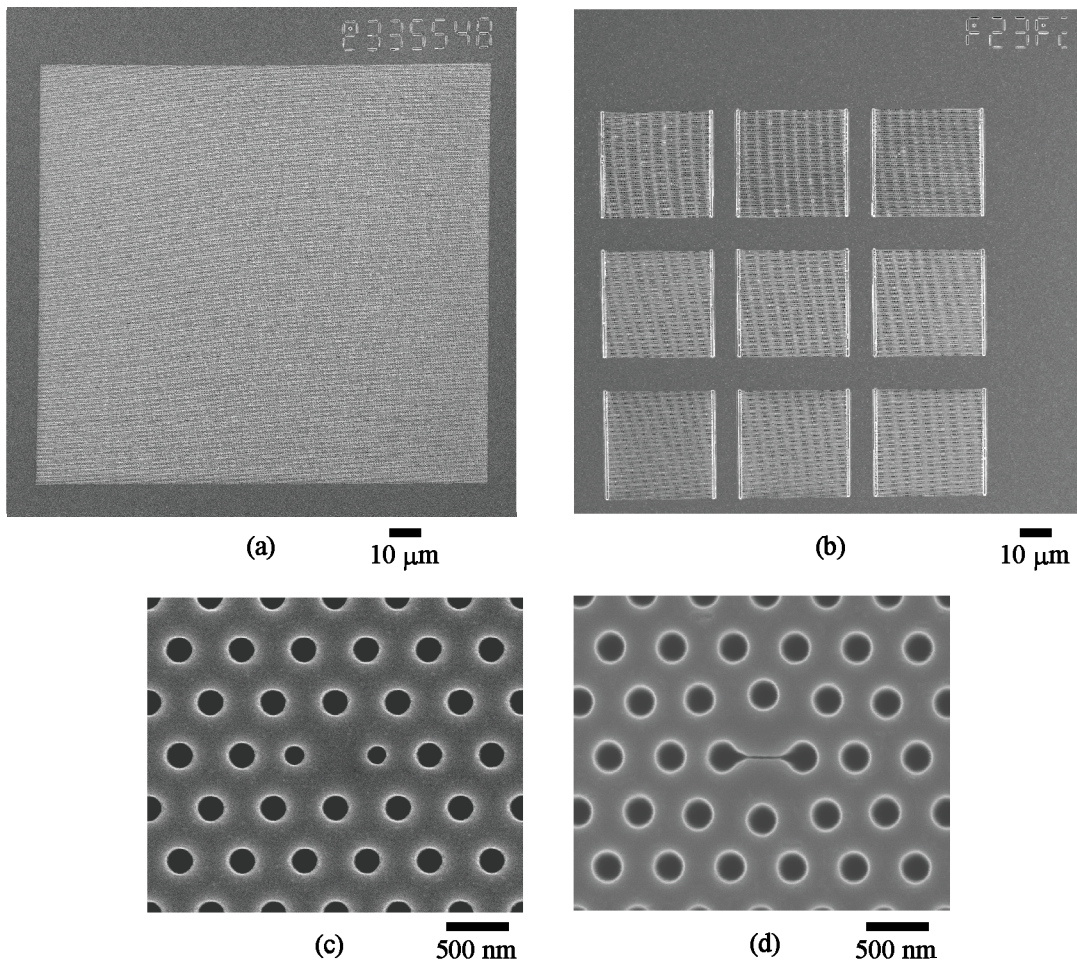
Fig. 3.11. SEM images of the fabricated device. (a) Bonding device. (b) Air bridge device. (c) Single nanolaser. (d) Single NS nanolaser.

(1) Immersion in methylene chloride for 20 min at 130 °C; substitution of acetone and methanol, three times in each.

(2) O_2 plasma ashing under the conditions given in Table 3.5 #4.

(3) Immersion in HF solution for 10 min at room temperature; rinsing in ultrapure water for 15 s + 1 min.

(4) Cleavage to divide each patterned area for disposability.

(5) Preparation of the TEOS solution: the solution was formed of 5000 μl TEOS, 8000 μl ultrapure water, and 10 μl HCl, which were poured into a vial and stirred for 20 min at 30 °C to perform the primary reaction.

(6) TEOS reaction: the wafer was immersed in the TEOS solution in the vial and heated for half a day at 100 °C without the cap. With the TEOS hydrolysis completed, the wafer was covered with a sprung silica layer.

(7) Immersion into water to remove the fragments of silica on the wafer surface.

Silica sol-gel produced from TEOS

The reaction for producing silica from TEOS and the experimental conditions used are given below. First, the TEOS molecule was hydrolyzed under an acid and heating, to produce silicon hydroxide and ethanol:

$$Si(OC_2H_5)_4 + 4\,H_2O \rightarrow Si(OH)_4 + 4\,C_2H_5OH \tag{3.1}$$
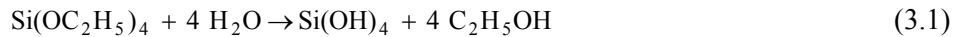
This reaction also proceeds at room temperature, but very slowly. Acid and base both act as catalysts, but in general, the presence of base shows greater catalytic activity because of the nucleophilic reaction of the hydroxide ion. Subsequently, the polycondensation of silicon hydroxide produces silicon dioxide:

$$n\,Si(OH)_4 \rightarrow n\,SiO_2 + 2n\,H_2O \tag{3.2}$$

This hydrolysis reaction formula shows the hydrolysis of all four silicon atom bonds. In practice, the progress of the reaction is affected by the ratio of TEOS to H_2O; the catalyst species also affects this progress. Additionally, the quality of the produced silica is altered by this ratio and the choice of catalyst species. We searched for the best conditions for each parameter for the silica embedding, by using HCl, CH_3COOH, NH_3, and H_2SO_4 as the catalyst species, and found that HCl was the best for forming silica with a high density.

Effect of the InP cladding layer on silica embedding

One of the essential points of difference from Section 3.2.5 was avoiding the etching of the

InP cladding layer, so that the silica was formed firmly. This process used ammonium sulfide solution and H_2SO_4 to etch the InP cladding layer. Variations in the process may be insufficient to remove the reaction products, but the high yield of the lasing of the fabricated device was confirmed. Therefore, we think that the negative effects caused by this change are almost negligible in this study.

Effect of alcohol

TEOS is hydrophobic. Therefore, a solution composed of TEOS and water is not miscible. To accelerate the reaction process, an amphiphilic molecule such as alcohol could be used. We tried adding methanol to the preparation solution but found that the yield of the fabricated silica in the holes decreased as the volume of methanol increased. This was thought to be caused by the breaking of the silica when the alcohol vaporized in the hydrolysis heating process. Thus, in fact, a less amphiphilic molecule was desired. After further tests, we found that using only the ethanol generated from the TEOS pre-reaction gave the best yield.

3.2.7 **Bonding**

Before bonding, the InP cladding layer was removed by HCl wet etching for 30 s under the conditions listed in Table 3.3. Following this, the device was left to rest for half a day to stabilize the surface chemical condition. The hydrophilic treatment by O_2 plasma was used for adhesion to polymerized PDMS. However, polymerized PDMS surface shows a poor compatibility in the bonding, so that the hydrophilic treatment was not used in this preparation, and the bonding by the polymerization was used. The bonding procedure was as follows:

(1) Preparation of the pre-polymerized PDMS, composed of the PDMS monomer SYLGARD184 (Dow Corning) and Silpot184 (Dow Corning) catalyst, with a ratio of 1:6.
(2) Churning of the compound liquid with a medicine spoon.
(3) Removal of air bubbles generated from the early polymerization reaction by deaeration with a pump for 1 h.
(4) Dipping of the surface of the active layer side of the wafer into the PDMS mixture. Sanding of the PDMS between the wafer and glass substrate.
(5) Pressing the wafer to uniformize the PDMS layer.
(6) Warming the PDMS with the wafer in an oven at 180 °C for 1 h for primary polymerization.
(7) Removal of unnecessary parts of the polymerized PDMS.

(8) Warming of the PDMS with the wafer in an oven at 180 °C for half a day for polymerization.

(9) Removal of the InP substrate by HCl wet etching for ~6 h, with all other conditions the same as those given in Table 3.3. Removal of any air bubbles during etching.

(10) Removal of the silica by buffered HF wet etching for 1 min; rinsing with pure water for 15 + 60 s.

(11) Oxidization of the wafer surface by heating in an oven for 1 h at 180 °C.

3.2.8 **Trimming**

When the device was immersed in the HCl solution and irradiated by pumping light, etching of the slab occurred and the λ of the nanolaser pumped should have blue shifted. Fig. 3.12 indicates the time evolution of the spectra during the etching. Fig. 3.12(a) shows this blue shift and highlights that the speed of the etching is controlled by the density of the HCl solution. The ratio of HCl:H$_2$O = 1:10^4 is best for λ trimming because faster etching generates the unwanted shift during the light alignment. The time evolution of the intensity during the etching was also measured and is shown in Fig. 3.12(b). This shows how, after 160×10^3 s in the HCl:H$_2$O = 1:10^4 solution, the initial intensity decreased significantly. Considering the measureable range of the intensity as a function of time, the trimming range that is practically accessible using this method is ~30 nm. We can then trim λ by post-processing. We trimmed the λ of the $3 \times 3 = 9$ nanolasers as shown in Fig. 3.13. In this process, attention had to be paid to the crosstalk of the
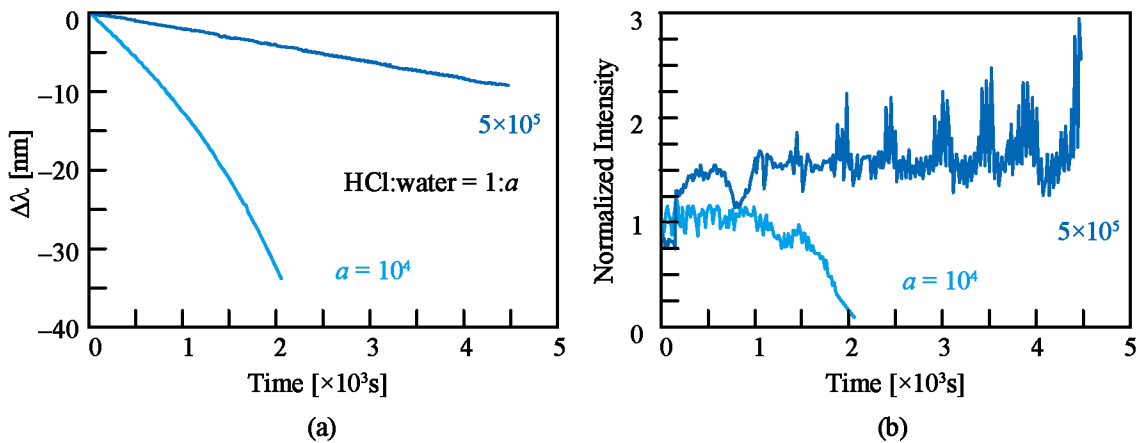
Fig. 3.12. Time evolution while the lasing nanolaser was immersed in HCl solution. (a) Spectral peak as a function of time. (b) Intensity as a function of time. The plot color indicates the density of HCl.
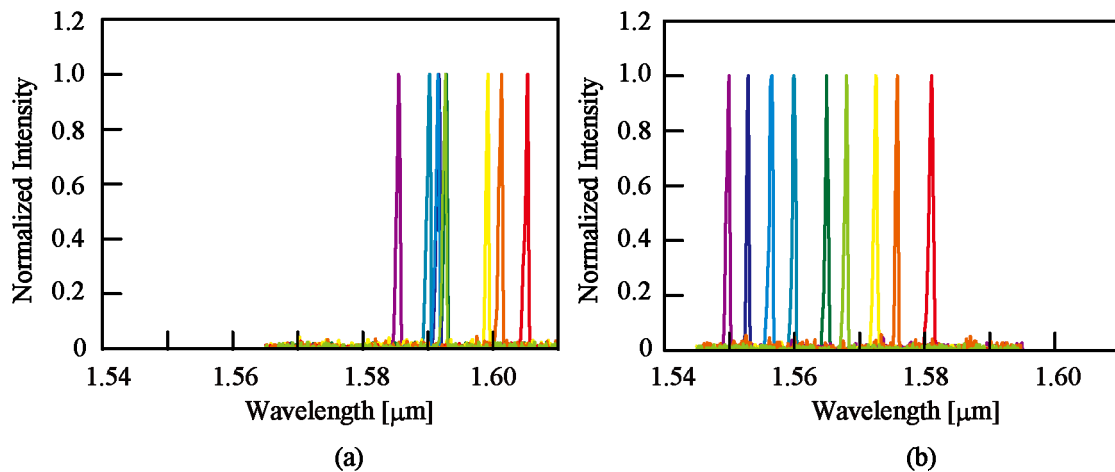
Fig. 3.13. Spectra of the alignment of λ in 9 nanolasers. (a) Before trimming. (b) After the sixth trimming process.

etching. In this experiment, we trimmed each nanolaser and measured the resultant λ repeatedly. Fig. 3.13(b) shows these data for λ after the sixth trimming process.

Reference

[3-1] S. Kita, K. Nozaki and T. Baba, "Refractive index sensing utilizing a cw photonic crystal nanolaser and its array configuration", *Opt. Express*, vol. 16, no. 11, pp. 8174-8180, 2008.

[3-2] S. Kita, K. Nozaki, S. Hachuda, H. Watanabe, Y. Saito, S. Otsuka, T. Nakada, Y. Arita, and T. Baba, "Photonic crystal point-shift nanolaser with and without nanoslots --- design, fabrication, lasing and sensing characteristics", *IEEE J. Sel. Top. Quantum Electron*, vol. 17, no. 6, pp. 1632–1647, 2011.

[3-3] S. Hachuda, S. Otsuka, S. Kita, T. Isono, M. Narimatsu, K. Watanabe, Y. Goshima and T. Baba, "Selective detection of sub-atto-molar streptavidin in 1013-fold impure sample using photonic crystal nanolaser sensors," *Opt. Express*, vol. 21, no. 10, pp. 12815–12821, 2013.

[3-4] K. Nozaki, S. Kita, Y. Arita and T. Baba, "Resonantly photopumped lasing and its switching behavior in a photonic crystal nanolaser", *Appl. Phys. Lett.*, vol. 92, no. 2, pp. 021501, 2008.

[3-5] S. Kita, S. Hachuda, K. Nozaki and T. Baba, "Nanoslot laser", *Appl. Phys. Lett.*, vol. 97, no. 16, pp. 161108, 2010.

[3-6]   S. Kita, S. Otsuka, S. Hachuda, T. Endo, Y. Imai, Y. Nishijima, H. Misawa and T. Baba, "Super-sensitivity in label-free protein sensing using nanoslot nanolaser", *Opt. Express*, vol. 19, no. 18, pp. 17683-17690, 2011.

[3-7]   S. Kita, S. Otsuka, S. Hachuda, T. Endo, Y. Imai, Y. Nishijima, H. Misawa and T. Baba, "Photonic crystal nanolaser bio-sensors", *IEICE Trans. Electron.*, vol. E95-C, no. 2, pp. 188-198, 2012.

[3-8]   K. Nozaki, S. Kita and T. Baba, "Room temperature continuous wave operation and controlled spontaneous emission in ultrasmall photonic crystal nanolaser", *Opt. Express*, vol. 15, no. 12, pp. 7506-7514, 2007.

[3-9]   M. Narimatsu, S. Kita, H. Abe, and T. Baba, "Enhancement of vertical emission in photonic crystal nanolasers," *Appl. Phys. Lett.,* vol. 100, no. 12, pp. 121117, 2012.

[3-10] W. F. Yeung, and A. R. Johnston, "Effect of temperature on optical fiber transmission", *Appl. Opt.*, vol. 17, no. 23, pp. 3703–3705, 1978.

[3-11] M. Kimoto, "Pore size control of mesoporous silicas from mixtures of sodium silicate and TEOS", *Technology research institute of Osaka prefecture report*, no. 22, 2008.

[3-12] K. Nozaki, "Ultimately-Small Semiconductor Photonic Crystal Lasers and Spontaneous Emission Control," *Doctoral thesis (Yokohama Nat'l Univ.)*, 2007.

[3-13] S. Kita, "Photonic Crystal Nanolaser Sensors" *Doctoral thesis (Yokohama Nat'l Univ.)*, 2012.

[3-14] T. Baba, "Photonic crystals and microdisk cavities based on GaInAsP-InP system," *IEEE J. Sel. Top. Quantum Electron.,* vol. 3, pp. 808-830, Jun 1997.

[3-15] H. Abe, M. Narimatsu, T. Watanabe, T. Furumoto, Y. Yokouchi, Y. Nishijima, S. Kita, A. Tomitaka, S. Ota, Y. Takemura and T. Baba, "Living-cell imaging using a photonic crystal nanolaser array," *Opt. Express*, vol. 23, no. 13, pp. 17056-17066, 2015.

Chapter 4
Fundamental operation

In this chapter, the fundamental characteristics of the fabricated devices and system developed for cell imaging are reported.

4．1　Fabricated devices

4．1．1　Laser characteristics

Figure 4.1 shows a schematic of the optical system used for the measurement of the fabricated PC nanolaser. For the measurement, the device chip was fixed, by glass plates on its side or set in a PDMS microchannel so that it could be immersed in liquid and photopumped from above with a 980-nm pulsed laser light (with 1-µs length and 10-kHz repetition) through a 50x objective lens. Emissions from the nanolaser were detected by the same lens, observed with an InGaAs infrared camera, and measured with an optical spectrum analyzer (OSA), Advantest Q8383 (0.2-nm spectral resolution), Agilent 86141b (wavelength absolute accuracy 0.5 nm), and a spectrometer, Roper SP2760-3 (spectral resolution 0.139 nm) with an InGaAs array detector, Roper OMA-V1024. The spot size of the pumping light was controlled by choosing the light fiber at the pumping laser output, ~3 or ~20µm. The ~3-µm size was used for the excitation of this particular device without NS, and the ~20-µm size used for the parallel
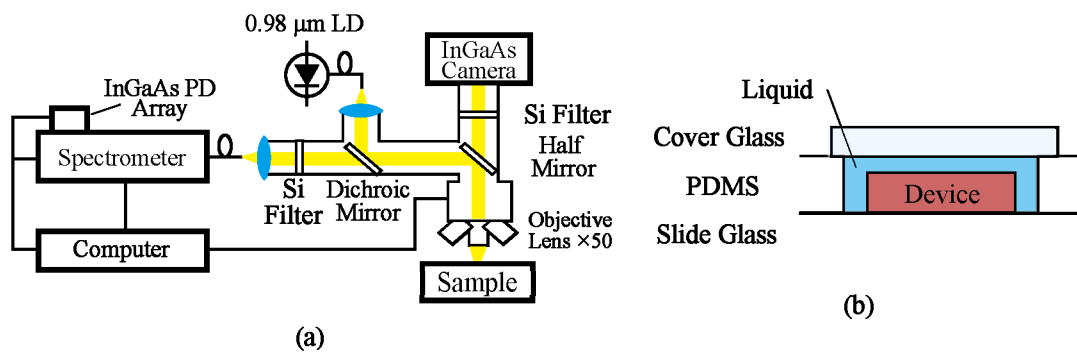
Fig. 4.1. Schematic of the measurement setup. (a) Optical system. (b) Sample environment.
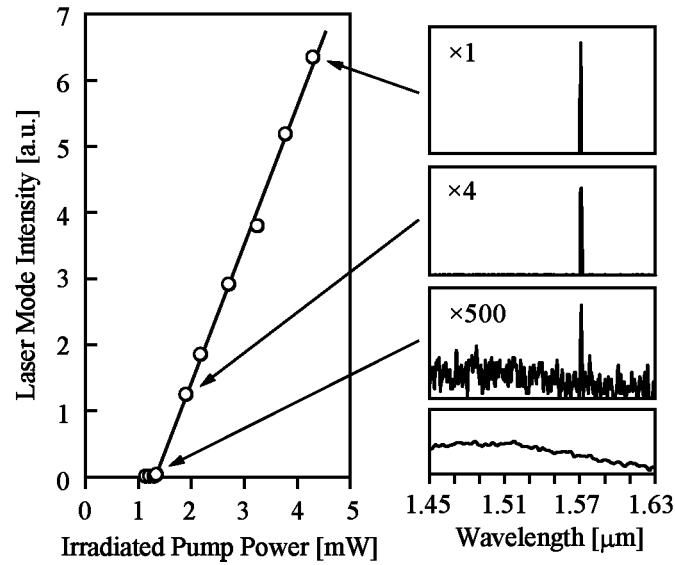
Fig. 4.2. Pulsed lasing characteristics of a single nanolaser formed on PDMS and immersed in water. Right lower panel shows the spontaneous emission spectrum of an unpatterned slab on PDMS, obtained by pumping harder with a larger pump spot. It indicates that the spontaneous emission peak was approximately 1.50 μm and that the noisy background in the second lowest panel arose from spontaneous emission. [4-1]

measurement and excitation of the NS device. The loss of pumping light between the pumping laser and the sample, and the loss of emission light between the sample and the spectral instrument was ~10 dB. The microscope system, Cascade Microtech Prober bench is containing a piezoelectric micrometer to control the stage. The computer control of the stage and spectral instruments enabled automatic optical axis adjustment and automatic measurements, programmable through LabVIEW software.

Figure 4.2 shows the characteristics of a single nanolaser. The intensity of the single mode peak is more than 30 dB (40 dB maximum), higher than the background spontaneous emission level, indicating laser emission occurred. The spectral width was typically 0.6 nm above the threshold, which is known to be caused by thermal chirping under pulsed pumping conditions.

First, we fabricated a 21 × 21 = 441 array with a ~5-μm pitch, and a 5 × 5 = 25 array with a ~2.5-μm pitch. Figure 4.3(a) shows the near-field patterns of laser emission from 441 nanolasers in water. The lasing of all devices was confirmed, and although the emission intensities were not uniform, they were sufficient to measure the laser spectrum in the OSA. For the lasing wavelength measurement, each nanolaser was pumped and the measurement repeated by scanning the pump position using the computer-controlled stage. We expected the wavelengths to converge to nine values, but each wavelength fluctuated owing to disorder in the fabrication,

60
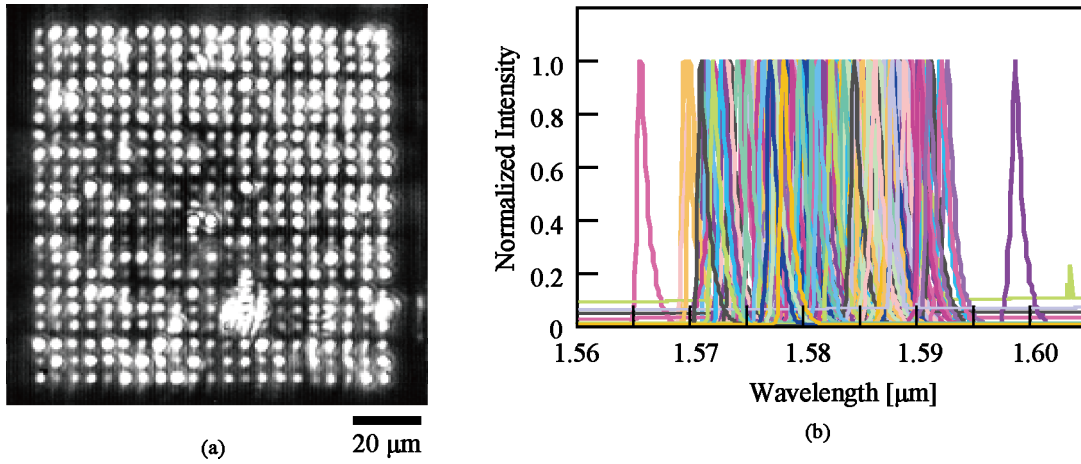
Fig. 4.3. Lasing of 441 nanolasers. (a) Near field pattern. (b) Spectra. [4-1]
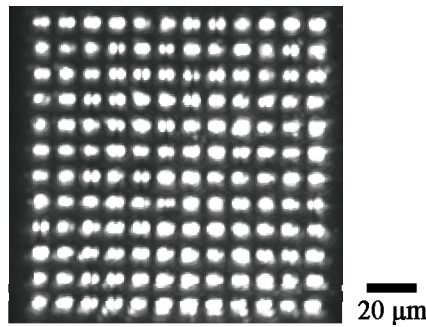
Fig. 4.4 Near field pattern of 121 nanolasers with NS. [4-1]

consequently they were distributed, almost continuously, in the range 1.57–1.59 μm, as shown in Fig. 4.3(b). We also fabricated a nanolaser array with NS. Figure 4.4 shows the lasing from the 11× 11 = 121 NS nanolaser array with a ~5-μm pitch, indicating 100% emission.

4. 1. 2 **Imaging characteristics**

In this study, the Δλ image was constructed offline after removing the attached medium, measuring the reference λ, and mapping Δλ at each position. As a test, we partially covered the device with a Zeon resist, ZEP520A, and an organic substance (which remained after culturing the cells) and obtained the Δλ image, as shown in Fig. 4.5. The resist and organic substance in the optical micrograph were clearly reconstructed in the Δλ image.
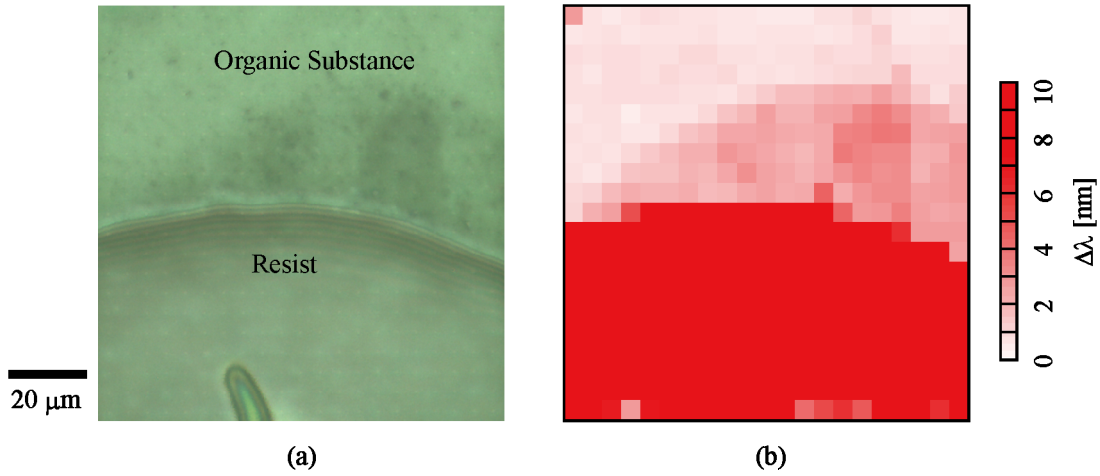
Fig. 4.5. Observation of resist pattern on a nanolaser array. (a) Optical micrograph of resist pattern and organic substance. (b) Δλ image. [4-1]

4.1.3 **Sensitivity**

Figure 4.6 shows all the lasing spectra with and without NS. Evidently, the NS narrowed the spectrum. Although the averaged full-width at half-maximum was wider than the resolution limit of the OSA used in both cases, that with NS was much closer to the resolution limit. Moreover, the uniformity of the spectral shape was markedly improved by NS, resulting in stability of the peak wavelength. Next, we calibrated the non-uniformity in Δn by evaluating, in advance, the sensitivity A of each nanolaser as shown in Fig. 4.7. For the evaluation, we measured the λ of the all the nanolasers in the sugar water of various concentrations, the refractive indices of which were measured independently with a refractometer.
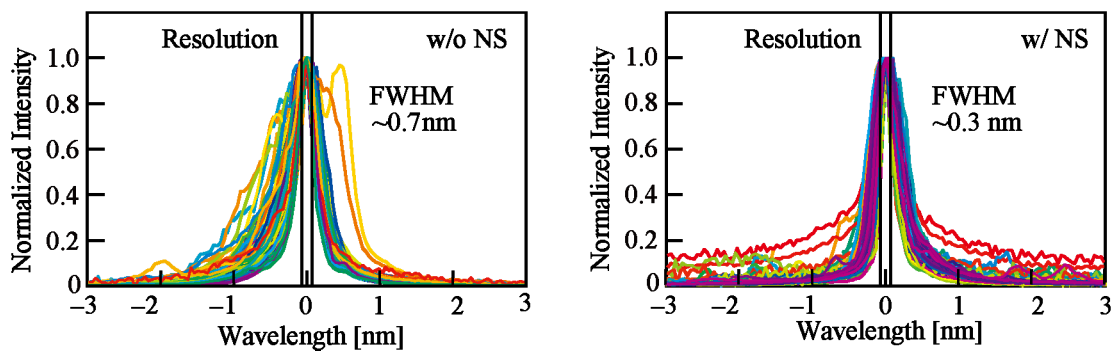
Fig. 4.6. Spectra of ~100 nanolasers for w/ and w/o NS. The line indicates the spectroscopic resolution. [4-1]
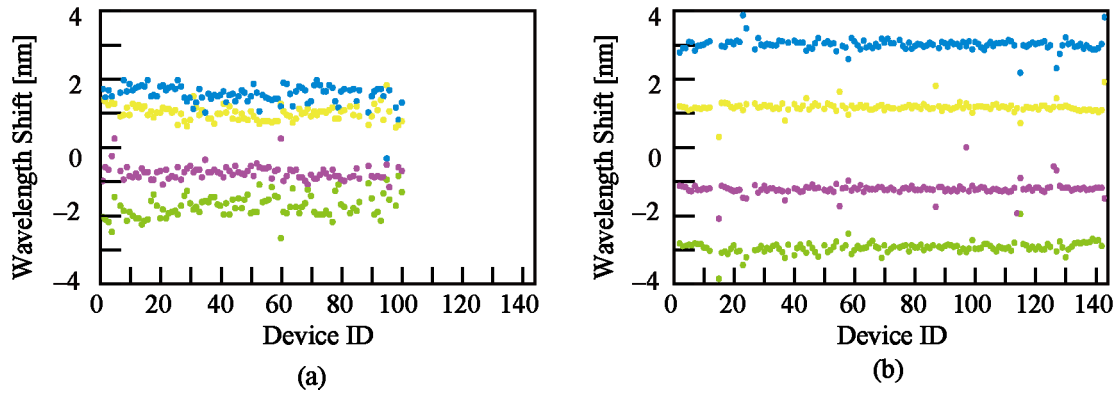
Fig. 4.7. Wavelength shift of the array with and without NS. Green, purple, yellow, and blue plots represent liquid indices of 1.33, 1.35, 1.37, and 1.39, respectively. (a) W/o NS. (b) W/ NS.
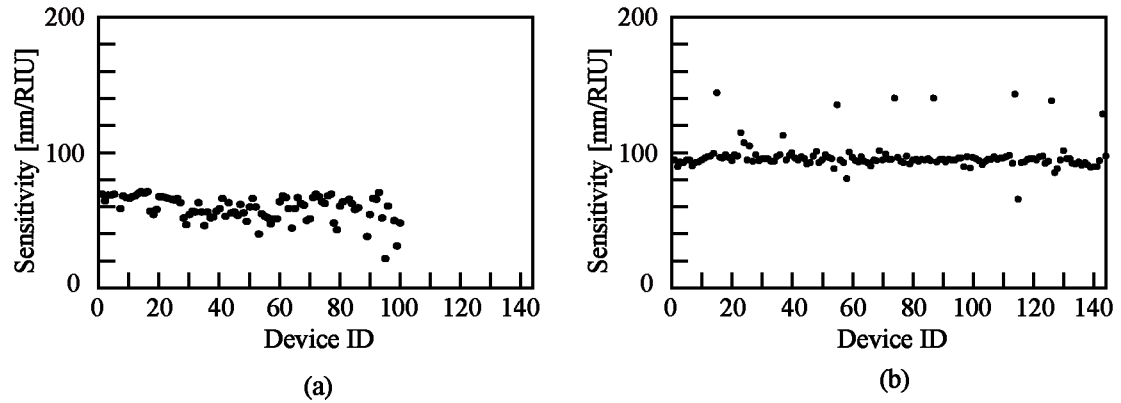
Fig. 4.8. Sensitivity of each device in the array with and without NS. Green, purple, yellow, and blue plots represent liquid indices of 1.33, 1.35, 1.37, and 1.39, respectively. (a) W/o NS. (b) W/ NS. [4-1]

A, as the liquid index, was obtained from $\Delta\lambda/\Delta n$ for all nanolasers, as shown in Fig. 4.8. Without the NS, A is distributed from 50 to 70 nm/RIU, neglecting the most scattered 10% of points. This indicates that a comparably large non-uniformity was included in the $\Delta\lambda$ image. In other words, the non-uniform image of the cells, exhibiting wavelength shifts from 1 to 2 nm, qualitatively showed some actual cell behavior, even though the image is not precise. With the NS, A was markedly stabilized in the range 95–102 nm/RIU. Some strongly scattered points were due to the mode hops observed in the NS. This might be because of the mode spacing being reduced by incorporating the NS and should be increased in future studies for further optimization. The averaged A values were 97 and 57 nm/RIU with and without the NS, respectively. The A values were smaller overall than the structure on the PDMS, whereas the reverse of the photonic crystal slab did not contribute to the sensing. The laser penetration became deeper in the PDMS and shallower in the liquid compared with an air-bridge device.

The higher average value of *A* with the NS was attributed to the stronger light localization inside the NS outside of the semiconductor.

4.1.4 **Accuracy**

Then, Δn was obtained from $\Delta\lambda/A$ for each nanolaser. The absolute accuracy of Δn, defined as the difference between Δn obtained in the above manner and the value directly measured by the refractometer, is shown in Fig. 4.9. The index resolution was evaluated from the deviation in the absolute accuracy. Without the NS, the resolution was in the order of 10^{-2} RIU. Such a large dispersion, even after calibration, is thought to be due to spectral broadening and wavelength instability. The NS reduced this scattering range to 2×10^{-3} RIU, neglecting some points caused by mode hops. The highest index resolution of 10^{-5} was evaluated for the individual nanolaser under a Continuous Wave (CW) pumping condition. Compared with this, TO chirping under pulsed conditions still required suppression, an issue for future study.

4.1.5 **Noise**

Considering the noise in proposed method, the limitations of accuracy, caused by the fluctuations in the spectrum discussed above, are most important. Without this limitation, the change without any target should appear as noise in the $\Delta\lambda$ signal. The oxidation of the nanolaser array itself, by pumping light irradiation or time evolution, results in a spectral blue-shift. In this study, this oxidation is prevented by applying preliminarily oxidation during the fabrication process, and compensated for by suppression, using the model oxidation characteristics derived from the average of time evolution characteristics in nanolasers without
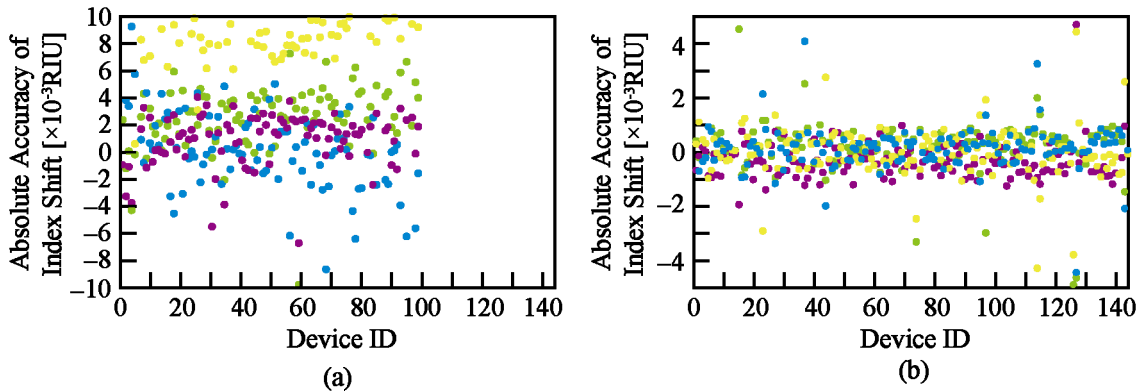
Fig. 4.9. Absolute accuracy of the array with and without NS. Green, purple, yellow, and blue plots represent liquid indices of 1.33, 1.35, 1.37, and 1.39, respectively. (a) W/o NS. (b) W/ NS. [4-1]

64

cell attachment. It is known that this oxidation is suppressed by the thin film formed on the nanolaser surface. Thus, we fabricated the nanolaser array with an oxide film formed using atomic layer deposition. However, ZrO_2 or SiO_2 films, confirmed as able to suppress oxidation, were not appropriate for cell attachment, so these films were not used in this study. In the future, the suppression of oxidation noise by a film conducive to cell attachment is expected. Additionally, the change in the culture fluids, necessary for cell observation, caused noise in Δn. An insufficient seal in the setup around the nanolaser device resulted in evaporation of the culture fluids. The evaporation gradually increased the concentration of the solution, and λ shifted to a long wavelength. In this study, the setup used for short-term observation contained this evaporation. Under these conditions, a red-shift appeared in the observation laser. Moreover, exchange of the solution or the injection of a reagent also resulted in noise due to the variations in the solution before and after exchange. This noise can be compensated for by suppression of the change during the 1st frame, just after the exchange.

4.2 **Imaging system**

In the proposed observation method, the measurement of a large amount of spectral data and the images generated resulted in a large amount of data processing. We introduced an automatic process to address this problem. The details of the imaging system developed are described below. In the measurement, the optical setup shown in Fig. 4.1 was used. As a premise, the observation requires the adjustment of the optical alignment, the measurement by a spectrometer, the data save, and the data processing. Initially, these processes were hand operated. A large amount of the data requires the automatization. The requirements for the automatic process are

- Automatization of measurements
- Automatization of an adjustment of the optical alignment
- Automatic data arrangement with the time and coordinate information
- Automatic mapping image generation
- On-line data processing
- High frame rate corresponding to real time observation

The total procedure needs a large number of spectral measurements more than 10,000 with a total time consumption of several hours, and many optical alignments and data arrangement are the same. Therefore, these works with hand operation are essentially difficult. The real time observation is usually conducted in other cell observation methods. A high frame rate is desired for the real time observation in this study. In this method, the frame time is limited
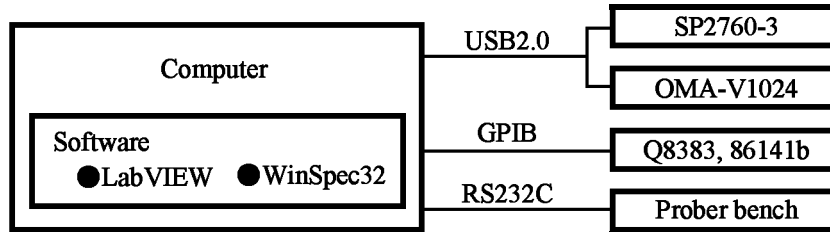
Fig. 4.10. Schematics of the automatic measurement setup.

by the spectral measurements for all nanolasers. The exclusion of hand operations in the measurement procedure is also effective in view of the frame rate. The on-line data processing is necessary to check the observed image. Ideally, an on-line display of the mapping image is desired. However, a complex data processing will decrease the frame rate.

4. 2. 1 **Setup**

We developed a communicating and programmable system. The controlled instruments and software employed were

- Piezoelectric micrometer controlling the coordinates of the microscope mirror stage
- OSA, the diffractive grating, and the array photo detector
- LabVIEW

Fig. 4.10 indicates the schematics of the automatic measurement system setup. Here, LabVIEW is a programming software controlling the measurement instruments. Winspec32 is the program specially communicating with SP2760-3 and OMA-V1024. The measurement instruments communicated via RS232C, GPIB, and USB2.0.LabVIEW supports a command transmission to the address of the instrument through GPIB or RS232C communication. This enables a command communication with Q8383, B86141 and piezoelectric micrometer of Prober bench. LabVIEW also treats the handle of another program, so that the communication with SP2760-3 and OMA-V1024 through the handle of WinSpec32 is possible. By using this setup, we developed element programs as driver controlling instruments, i.e. measurement of the spectrum, acquiring the measured data, setting the instrument's condition, moving the stage to an arbitrary coordinate, and getting the instrument's condition. Fig.4.11 shows an example of the developed element programs. In Fig. 4.11(a), the strings meaning command setting the condition of the OSA were sent to the address defined by "VISA Session". In Fig. 4.11(b), "WINX32Lib.ExpSetup" is the handle of WinSPEC32, and the invoke nodes send the
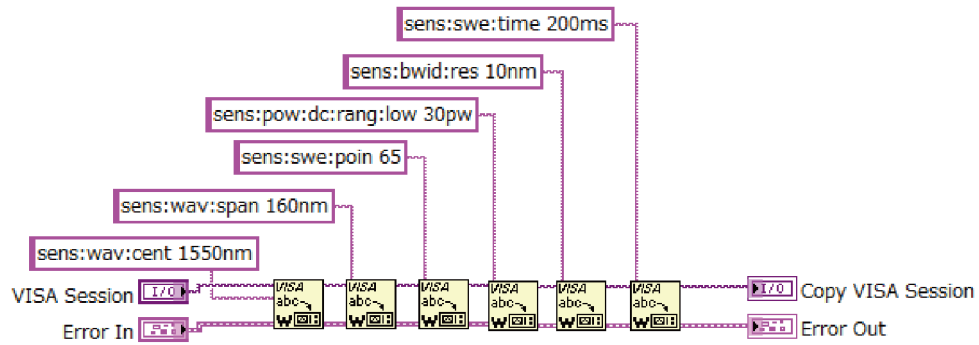
(a)
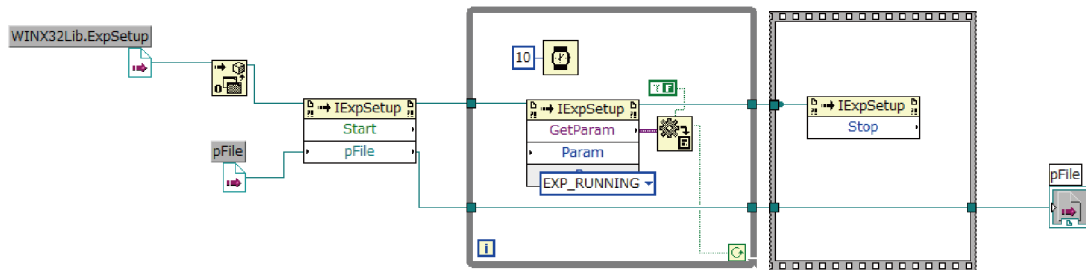
(b)

Fig. 4.11. Print screen of developed element LabVIEW programs. (a) Program setting the condition of 86141b. (b) Program commanding the measurement function to WinSPEC32.

"measurement", "wait" and "stop" command from left to right. We developed the total automatization program by a combination of such element programs.

4.2.2 **Data processing**

<u>Frame of total system</u>

We developed the total automatic measurement and data processing program composed of four parts. The reason for dividing into four parts was to use each partial part, in both on-line process and off-line processes. Initially, we tried to build an all on-line processing. However, because the format of Matlab was necessary to generate the images, and we must set the timing of taking the reference λ after the main measurement, which was also necessary to generate the images, the off-line process was finally employed.

Prepared four programs:

1. Output the spectra and coordinates for each nanolaser against the input information for the nanolaser array.

2. Measure repeatedly for the input coordinates and provide the spectra as outputs.

3. Data processing to obtain the continuous 2-dimentional (2D) λ data

4. Data processing to generates continuous Δλ or Δn image.

Fig. 4.12 shows the schematic of the on-line process and the output data of each program. Here, Program 1 and 2 are on-line processes, and Program 3 and 4 are off-line processes. In the automatic measurement, the pump light spot related to the position of each nanolaser was controlled. The coordinate for each nanolaser was initially unclear, mainly because of the tilted angle of the substrate holder. Program 1 was used to search the coordinates. Program1 was used to not only for the cell imaging but also for the measurement of the fundamental operation or reference λ. By repeating Program 1, the continuous observation was made possible. However, the repetition of the adjustment sequence decreases the frame rate. In Program 2, the spectrum for each coordinate obtained in Program 1 was measured repeatedly. In these programs, the measured spectra were arranged for the coordinate and frame of the continuous observation. In the off-line process, the program generated continuous mapping images from the measured
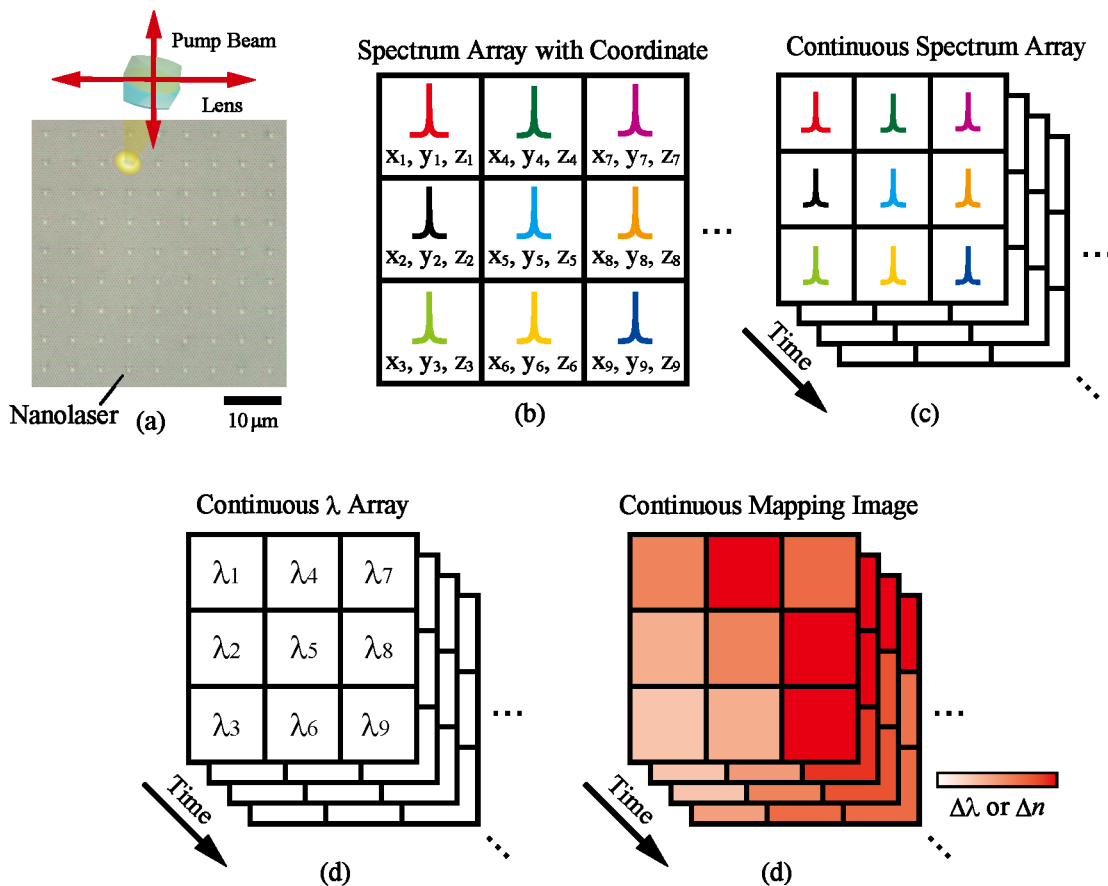
Fig. 4.12. Schematics of automatic programs. (a) Schematic of the measurement in on-line process. (b), (c), (d), (e) Schematics of the output data from program 1, 2, 3, or 4, respectively.

spectral data. Program 3 or 4 was developed with LabVIEW and Matlab, respectively. Here, LabVIEW was used for online data processing. The λ detection program can be diverted to the off-line process. Matlab was used to generate the mapping images with a completed template.

Program1

Parameters:

- Number of rows of nanolaser array: R
- Number of columns of nanolaser array: C
- Pitch between nanolasers in the vertical and horizon axes
- Row and column numbers at initially adjusted nanolaser in the array
- Computer address to save the output data files

Internal variables:

- 2-D coordinate data for x, y, and z axis: *2D-XYZ*. The row and column of 2-D data are corresponding to R and C, respectively.
- 2-D peak λ data of the measured spectra: *2D-λ*. The row and column of 2-D data are corresponding to R and C, respectively.

Content:

1. Set the condition of the spectroscope
2. Adjust of the optical alignment. Details are described below.
3. Save the spectrum with the row and column information
4. Save the peak λ of the measured spectrum to the corresponding element of *2D-λ*.
5. Save the adjusted coordinate to the corresponding element of *2D-XYZ*
6. Calculate the coordinate of the next nanolaser. Details are described below.
7. Move the optical alignment position according to the assumed coordinate
8. Adjust the optical alignment. Details are described below.
9. Save the spectrum with the row and column information
10. Save the peak λ of the measured spectrum to the corresponding element of *2D-λ*.
11. Save the adjusted coordinate to the corresponding element of *2D-XYZ*
12. Repeat procedure 7 – 12 for all rows and columns in nanolaser array
13. Output *2D-XYZ* and *2D-λ*

Procedure:

1. Input program parameters
2. Roughly adjust the optical alignment to an arbitrary nanolaser with hand operation
3. Start the program

Adjustment of the optical alignment:

1. Measure the spectrum

2. Read the peak intensity of the spectrum

3. Move the optical alignment for each axis with a pitch of 0.25 μm to x and y axis or 0.2 μm to z axis.

4. Measure the spectrum

5. Read the peak intensity of the spectrum

6. Continue 3 – 5 until the maximum extreme value appears for each axis. But the max moving distance was set at 1 μm to deal with the case of no emission.

7. Return the spectrum and coordinate with the maximum intensity.

Calculation of the coordinate of the unmeasured nanolaser:

The target coordinate was calculated by Eq. (4.1) for each axis.

$$x(\text{target}) = \frac{\displaystyle\sum_{n=1}^{\text{Max } n} \frac{x(n) + (Column(\text{target}) - Column(n))\, Pitch_x}{\sqrt{(Row(\text{target}) - Row(n))^2 + (Column(\text{target}) - Column(n))^2}}}{\displaystyle\sum_{n=1}^{\text{Max } n} \frac{1}{\sqrt{(Row(\text{target}) - Row(n))^2 + (Column(\text{target}) - Column(n))^2}}} \quad (4.1)$$

Where Max n is the number of already measured data. n is the ID of the already measured data. The target coordinate was calculated from the inverse of the distance.

<u>Program2</u>

Parameters:

● Computer address to save the output data files

● Address of the input file of *2D-XYZ*

Internal variables:

● 2-D coordinate data for x, y, and z axis: *2D-XYZ*. The row and column of 2-D data is corresponding to the nanolaser array.

● Displayed nanolasers number

● Frame number of frames in the continuous observation: *Frame number*.

● on/off state of "pause"

● *2-D λ data*. This dimension is corresponding to the nanolasers number, and *Frame number*.

● on/off state of "periodic alignment to the memorized coordinate"

● Standard period of "periodic alignment to the memorized coordinate"

● Coordinate of the optical alignment adjusted for the optical microscope

Content:

1. Set *2D-XYZ*

2. Set the condition of the spectroscope

3. Move one of the coordinate element in *2D-XYZ*

4. Measure the spectrum

5. Save the spectrum with the information of row, column, *Frame*

6. Save the peak λ to the corresponding element of *2-D λ data*

7. If the "state of the pause" is on, wait until this state becomes off.

8. Update the display of the measured spectrum and continuous λ plots at the nanolaser of "displayed nanolasers number" in the array. Here, the display of the spectrum reflects the saved spectrum data. The display of the continuous λ plots reflects *2-D λ data*.

9. If SP2760-3 and OMA-V1024 were used, reset the count function of the subwindow in WinSPEC32 to make the performance stable.

10. If the "state of "periodic alignment to the memorized coordinate" is on and the time interval over the "standard period of alignment to the memorized coordinate", move the alignment position according to "Coordinate of the optical alignment adjusted for the optical microscope". Wait for the fixed period to save the optical micrograph. These procedures are necessary to compensate for the color aberration between near infra-red and visible light.

11. Repeat 3 − 10 for each coordinate of *2D-XYZ*.

12. Repeat 11 with the increase of *Frame number* until the command of program stop

Procedure:

1. Input the address of the coordinate data file

2. Input parameters

3. Start the program

4. During the repeated operation, control "pause state", "state of periodic alignment to the memorized coordinate", "Number of the attend nanolaser", and *2D-XYZ*.

5. In the repeated operation, along with the timing of adjusting the optical alignment to visible light, acquire the optical micrograph.

6. Stop the program

Data processing support in measurement program:

To smoothen the measurement, we developed data processing functions displayed in the graphical user interface of LabVIEW. The display of the measured spectrum and the continuous peak λ plots were used to check the change in targets. Pause action was used not to obstruct the procedure of the exchanging the culture fluid or the injection of reagent in cell observations. The coordinate data *2D-XYZ* was set so as to compensate for optical misalignment appearing during the observation. To check the optical micrograph periodically, the function that moves

the optical alignment position to the memorized coordinate which was set under the visible illumination condition was developed. Here, we prepared two programs with and without the function of displaying the continuous λ plots: if we use that with the function, the frame rate decreases with the increase of the frame number.

<u>Program3</u>

Parameters:

- Computer address to save the output data files
- File address for measured spectra
- File address for initial λs data
- File address for the spectrum with dark condition

Internal variables:

- *2-D λ.* This dimension corresponds to the number of nanolasers, and the number of the frames in the continuous observation.
- *2-D past λs*. This dimension corresponds to the number of nanolasers and the number of peak λ in the spectrum.
- *2-D derivative of λ with time*. This dimension corresponds to the number of nanolasers and the number of peak λ in the spectrum.

Content:

1. Save the initial λs data to the *2-D past λs*.
2. Save '0' to all element of 2-*D derivative of λ with time*.
3. Pickup the λs peak from the measured spectrum with the corresponding nanolaser frame number
4. Identify each peak λs to be the one for the corresponding nanolaser or noise. Details are described below.
5. Save λ of the corresponding element of *2-D λ*
6. Repeat 3 − 5 for each nanolaser in the array
7. Repeat 6 for each frame in the continuous observation.
8. Output *2-D λ*

Procedure:

1. Input the address of "measured spectra files", "spectrum with dark conditions", "initial λs data"
2. Start the program

Identification of λ:

First, the dark spectrum data were subtracted from the row data, and the peak λs were detected by using the threshold and a second order derivative from five plots. Peak λs, as

detected from the spectrum, have several possible sources, i.e., the spectrum of the target nanolaser, the spectrum of the non-target nanolaser, noise above the threshold, unintended multimode emissions, or mode hopping. Therefore, if the peak corresponds to the nanolaser must be identified. In this study, the target nanolaser was identified by comparing *2-D past λ* with the previously measured λs at the same position. The λs data generated by Program 1 was used as the initial *2-D past λ*. The identification procedure are as follows:

1. The absolute difference between the past λ and measured peak λ is less than 1 nm
2. Return λ nearest to the estimated λ among λs satisfying the condition of Procedure 1, considering the derivative of λ with time.

2-D past λ. and *2-D derivative of λ with time* were renewed for each identification. When the measured λ corresponding to past λ is absent, *2-D past λ* holds the same value. Peak λ in this case was treated as noise. The standard in Procedure 1 should be changed by each frame-rate, but 1 nm is effective for temporal frame rates. When the experiment contained an instantaneously large Δn, for example, when the solution was exchanged to another one with different n, the noise data was saved as an alternative past λ. Then, the continuous λ of the nanolaser can be continued after the large Δn.

Program4
Content:

1. Input the 2-D λ. This dimension is corresponds to the number of nanolasers and the number of frames in the continuous observation.
2. Input the *A* for each nanolaser in the array
3. Input the reference λ for each nanolaser in the array
4. Calculating of $\Delta\lambda$ from the subtract of reference λ from λ
5. Calculating Δn form the dividing $\Delta\lambda$ by *A*
6. Generating continuous mapping images of $\Delta\lambda$ or Δn

Procedure:

1. Input 2-D λ data generated by Program3, reference λs data, and *A*s data.
2. Start the program

Here, the magnitude of $\Delta\lambda$ or Δn in the mapping image was displayed with colors. In the Δn image, the color bar was designed as a gradation showing different accuracy of the refractive index resolution.

4.2.3 **Performance**

<u>Use in the cell observation</u>

Compared with the hand operation, this program was effective in the cell observation experiments. This imaging system developed enables the continuous observation using a large scale integrated nanolaser array. However, this system still remained a room for improvement. In the repeatedly measurement of Program 2, the mismatch of the optical alignment appeared along with the time evolution. In this setup, the hand operation with numerous adjustments looking at the image of the lasing emission taken via the InGaAs camera for a 0.5− 1.0 h was necessary. To solve this situation, we tried to introduce the automatic adjustment sequence for a period. But this trial did not reach to the actual use. The measurement with the generating the mapping image has also been undeveloped. This is mainly because the reference λ was measured after the removal of the cell. This problem may be solved by obtaining the reference λ before the cell attachment. However, in the test experiment, an intended shift was appeared in the signals. In the off-line process, the isolated action of nanolasers was not complete, resulting in the instability of the emission, the mismatch in the optical alignment, and the mode hopping. In this thesis, the procedure for such operation was described in Chap. 5. Time required for such procedure depends on the scale of the device and experimental period over a day. As a conclusion, we succeeded in the automatization of the core elements in the experiment, but still needed a number of hand operation assistants.

<u>Frame rate</u>

As discussed above, the frame-rate for continuous observation was determined by an automatic measurement system and spectroscopic characteristics. The amount of time required to spectroscopically observe all the nanolasers in automatic measurement Program 2 is proportional to the frame-rate. Simultaneous measurement and small-scale integration decreases this number, but it can occur only once. Therefore, this single measurement time is determined by exposure time in the detector, and the time required for data communication and saving. Here, we used the OSA or the combination of the diffractive grating and the array photo detector in the measurement. The array photo detector can measure the intensity for each λ simultaneously, so that the single measurement time becomes faster. In the OSA, the single measurement time was 15 s with the high-scence1 mode. In the array photo detector, the exposure time was 0.5 s with nanolasers that had a temporally lasing intensity, and 0.1 s for those with superior lasing intensity. The single measurement time was 1.2 s and 0.8 s for the temporal and superior lasers, respectively. From this it can be seen that the proposed method has a potential sub-second frame-rate, and may be applied to a second-order frame-rate. The observation area and the

density of the imaging pixels is the trade-off to the frame-rate.

Reference

[4-1] H. Abe, M. Narimatsu, T. Watanabe, T. Furumoto, Y. Yokouchi, Y. Nishijima, S. Kita, A. Tomitaka, S. Ota, Y. Takemura and T. Baba, "Living-cell imaging using a photonic crystal nanolaser array," *Opt. Express*, vol. 23, no. 13, pp. 17056-17066, 2015.

[4-2] K. Nozaki, S. Kita and T. Baba, "Room temperature continuous wave operation and controlled spontaneous emission in ultrasmall photonic crystal nanolaser", *Opt. Express*, vol. 15, no. 12, pp. 7506-7514, 2007.

[4-3] S. Kita, K. Nozaki and T. Baba, "Refractive index sensing utilizing a cw photonic crystal nanolaser and its array configuration", *Opt. Express*, vol. 16, no. 11, pp. 8174-8180, 2008.

[4-4] S. Kita, K. Nozaki, S. Hachuda, H. Watanabe, Y. Saito, S. Otsuka, T. Nakada, Y. Arita, and T. Baba, "Photonic crystal point-shift nanolaser with and without nanoslots --- design, fabrication, lasing and sensing characteristics", *IEEE J. Sel. Top. Quantum Electron*, vol. 17, no. 6, pp. 1632–1647, 2011.

[4-5] S. Hachuda, S. Otsuka, S. Kita, T. Isono, M. Narimatsu, K. Watanabe, Y. Goshima and T. Baba, "Selective detection of sub-atto-molar streptavidin in 1013-fold impure sample using photonic crystal nanolaser sensors," *Opt. Express*, vol. 21, no. 10, pp. 12815–12821, 2013.

[4-6] K. Nozaki, S. Kita, Y. Arita and T. Baba, "Resonantly photopumped lasing and its switching behavior in a photonic crystal nanolaser", *Appl. Phys. Lett.*, vol. 92, no. 2, pp. 021501, 2008.

[4-7] S. Kita, S. Hachuda, K. Nozaki and T. Baba, "Nanoslot laser", *Appl. Phys. Lett.*, vol. 97, no. 16, pp. 161108, 2010.

[4-8] S. Kita, S. Otsuka, S. Hachuda, T. Endo, Y. Imai, Y. Nishijima, H. Misawa and T. Baba, "Super-sensitivity in label-free protein sensing using nanoslot nanolaser", *Opt. Express*, vol. 19, no. 18, pp. 17683-17690, 2011.

[4-9] S. Kita, S. Otsuka, S. Hachuda, T. Endo, Y. Imai, Y. Nishijima, H. Misawa and T. Baba, "Photonic crystal nanolaser bio-sensors", *IEICE Trans. Electron.*, vol. E95-C, no. 2, pp. 188-198, 2012.

[4-10] M. Nomura, S. Iwamoto, K. Watanabe, N. Kumagai, Y. Nakata, S. Ishida, and Y. Arakawa, "Room temperature continuous-wave lasing in photonic crystal nanocavity", *opt. Express*, vol. 14, no. 13, pp. 6308-6315, 2006.

[4-11] O. Painter, R.K. Lee, A. Scherer, A. Yariv, J.D. O'Brien, and P. D. Dapkus, "Two-dimensional photonic band-gap defect mode laser", *Science*, vol. 284, pp. 1819–1821, 1999.

[4-12] H. Altug and J. Vučković, "Photonic crystal nanocavity array laser," *Opt. Express*, vol. 13, no. 22, pp. 8819–8828, 2005.

[4-13] T. Watanabe, H. Abe, Y. Nishijima and T. Baba, "Array integration of thousands of photonic crystal nanolasers," *Appl. Phys. Lett.*, vol. 104, no. 12, pp. 121108, 2014.

Chapter 5
Cell imaging

To demonstrate the proposed cell observation method, we attempted to observe an actual cell. We administered a reagent to promote chemical reactions in a cell and observed cell reactions before, during, and after the administration.

5.1 **Method**

5.1.1 **Overview**

The measurement procedure is shown in Fig. 5.1. First, we prepared a PC nanolaser array. HeLa cells were attached to a substrate in a culture dish. Then, using the measurement system described in Chapter 4, the positions of the PC nanolasers for each wavelength λ were confirmed by the pumped light spot from a single-mode laser diode (LD), as shown in Fig. 5.1(c). The multimode LD was used for simultaneous measurement. The spectra of the overall nanolaser array were repeatedly measured. Furthermore, a reagent that introduces a cellular change was injected. The cellular reaction to the reagent was also observed by repeated measurement. The control experiment without reagent showed evidence of the reaction. We measured individual values of λ again after the experiment. The reference λ was measured after the injecting the specific reagent after removal of cells. The reference λ was also measured for the condition when the cells became detached during the experiment.

Ideally, the absolute value of n can be acquired from λ. However, culture fluid contains various foreign substances such as proteins, amino acids, and glucose. The presence of these extracellular contaminants may produce an additional Δn and cause noise in the measurement of n. Because such additional attachment is thought to be due to strong physical adsorption, the $\Delta \lambda$ due to the additional attachment is assumed to be fixed value. In addition, because the cells are surrounded with culture fluid, the calculation of the relative n from the culture fluid is useful. Therefore, we calculated $\Delta \lambda$ for each nanolaser according to the Δn induced by the cell attachment. Then, the envisioned measurement conditions were categorized for the cases without cells, with cells, and with cells showing some changes.
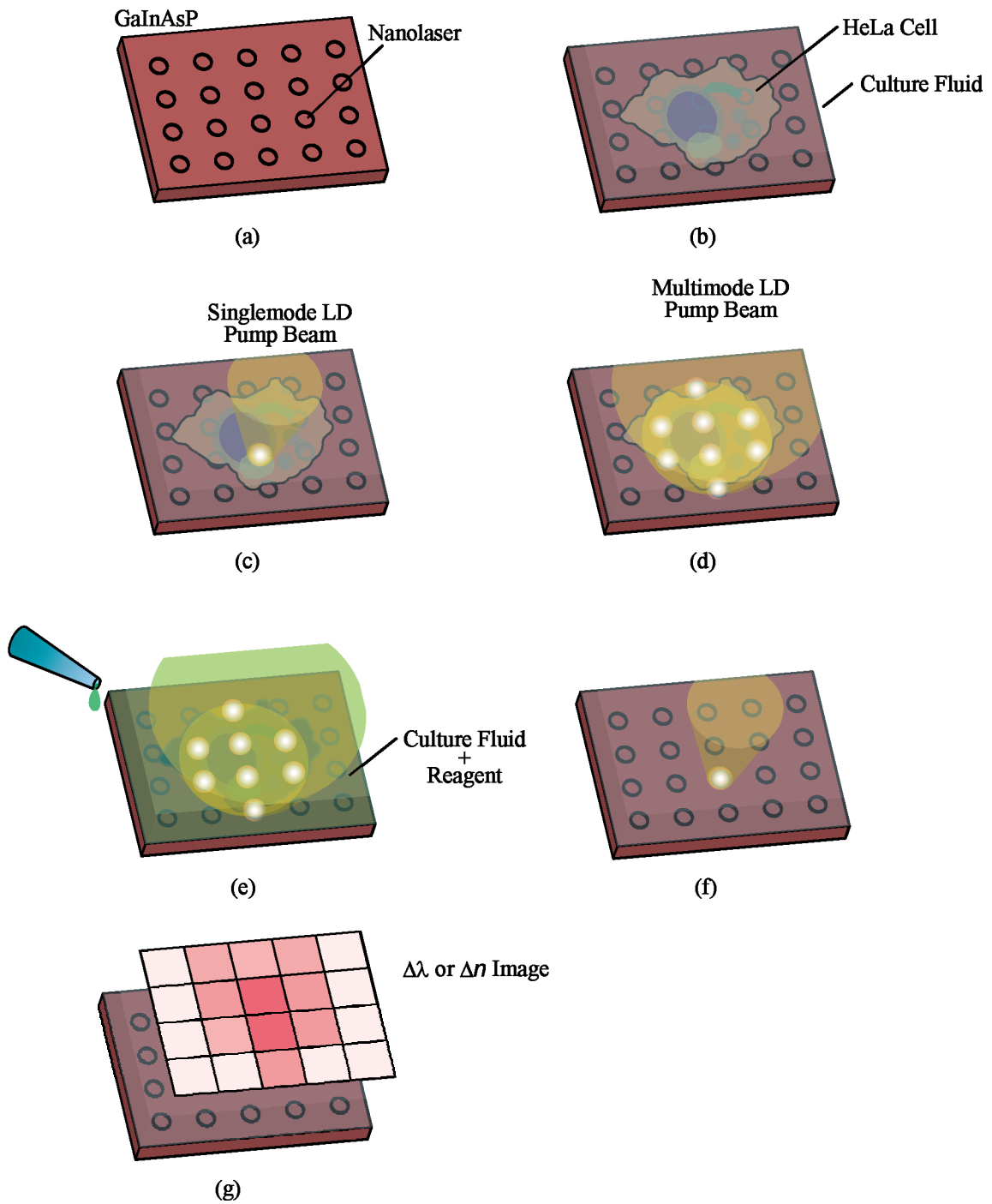
Fig. 5.1 Cell imaging procedure: (a) preparation of device, (b) attachment of HeLa cells, (c) individual measurement single-mode LD pumping, (d) parallel measurement by multimode LD pumping, (e) measurement in reagent environment, (f) measurement of reference λ after removal of cells, and (g) mapping of $\Delta\lambda$ and Δn.

5. 1. 2 **Preparation**

5. 1. 2. 1 **Procedure**

The procedure for attachment of the cells onto a GaInAsP substrate is described as follows:

(1) The fabricated device surface was hydrophilically treated by ICP O_2 plasma. The conditions of the treatment were basically the same as those described in Chap. 4: the bias power was 0 W, the ICP power was 200 W, the gas flow rate was 30 sccm, and the time was 1 min.

(2) The device was set into the culturing case.

(3) The device was immersed in 70% ethanol for 5 min.

(4) The device was immersed in phosphate-buffered saline.

(5) The device was placed into a vessel filled with a culture fluid that included human cervical carcinoma line (HeLa) cells.

(6) Incubation was performed overnight at 37°C with 5% CO_2 to culture cells on the devices for 20–26 h.

Fabricated device were, Because PDMS is hydrophobic and interferes with cellular attachment, the hydrophilic treatment to the nanolaser array device was done. the . The devices were washed with ethanol to eliminate bacteria, and phosphate-buffered saline to modify its surface for cellular culturing. The device was y placed into a vessel filled with Dulbecco's modified Eagle's medium (DMEM) (Gibco) supplemented with 10% fetal bovine serum (FBS) (Gibco) and 1% penicillin streptomycin (Gibco). The density of HeLa cells in the culture fluids was 2×10^5 cell/ml. Here, the structure of the vessel is a empty cylinder in which an area is 1.9 cm^2, and 500 μl of culture fluid was placed in it. By the incubation, HeLa cells were attached on the device. After incubation, the device chips and the incubator fluid were placed in the measurement setup.

Because CO_2 was not fed into the setup during the experiment, the activity of the cells was maintained for only several hours by the change of culture fluid's pH. For a longer observation period, we also used another Leibovitz's L-15 medium (Gibco), which suppresses the CO_2 deficiency. The detail of the measurement setup was described in Sec. 5.1.3.

Figure 5.2 shows the HeLa cells attached on the GaInAsP substrate and PC structure. A healthy cultured epithelial cell shows a generally flattened shape. Many experiments involving these samples cells attached flatly. This suggests strong attachment and low cytotoxicity of the
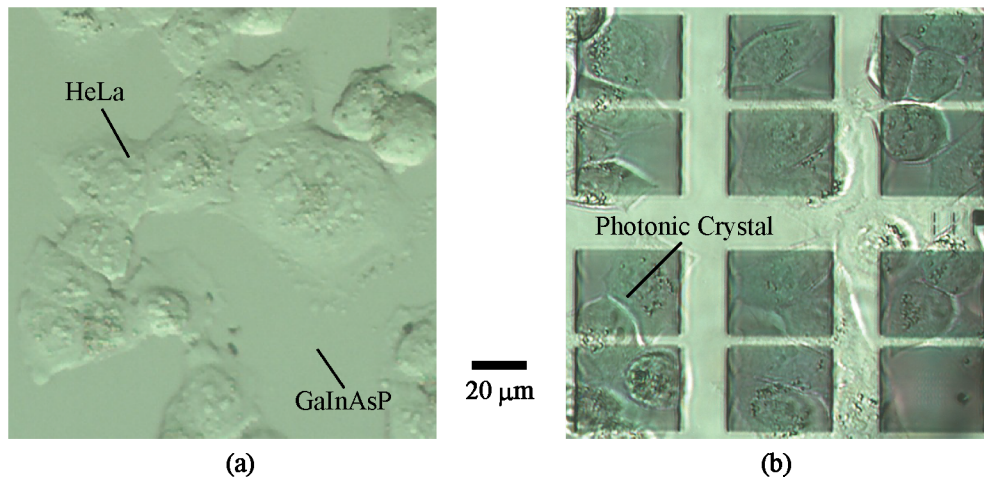
Fig. 5.2 Optical micrographs of HeLa cells attached on substrates: (a) attachment on the GaInAsP substrate, and (b) attachment on the PC pattern.

nanolaser material (GaInAsP) and PC structure.

5. 1. 2. 2 **Cell**

The cells used in this study were HeLa cells. HeLa cells are derived from human cervical carcinoma cells. They are the world's first successful long-term, human-derived cell culture and are widely used in testing and research. Long-term cell culture is impossible without cancer cells because such culture requires the preparation of cells obtained from living tissues for each experiment. Such preparation induces a change of state in the cells and makes the experiment unstable. Except for cells such as embryonic stem cells, the present cell lines are limited to cancer cells. This is because of the issues with deoxyribonucleic acid (DNA) replication. Telomeres in chromosomes progressively were shorten with cell division, which limits the long-term cell culture of normal cells. Cancer cells have DNA abnormalities that allow unlimited cell division. HeLa cells are widely used in human cell experiments. In this study, HeLa cells were used to overcome the limitation of short culturing periods. We used HeLa cells, which are characterized by a high nuclear to cytoplasm ratio.

5. 1. 3 **Setup**

In cellular experiments, the requirements for the measurement environment surrounding the nanolaser array are as follows:

- Filling with culture fluids

- Thermal control

- pH control

- Suppression of evaporation

- Changeability of the solution

A culture fluid environment is necessary for cell culturing and the maintenance of cellular health. We used a flow channel filled with the culture fluid used for incubation. Thermal and pH control are also required for cell culture. However, the introduction of a basic pH control system using DMEM and CO_2 gas in the measurement setup requires additional steps. Thus, we used DMEM for short-term observation and L-15 for long-term observation. In the case of DMEM, the environment is impracticable for cell culturing; thus, the experiment time was limited to less than a few hours. In the case of L-15, CO_2 control is not required, but a strict seal is needed for evaporation suppression and maintenance of the amount of culture fluid for pH buffering. In any case, a seal is required for stable measurement. The solution around the nanolaser array needs to be changed to allow for the injection of reagent or the exchange of culture fluid. This was solved by development of the flow channel and fixing of the nanolaser substrate.

Figure 5.3 shows a schematic of the flow channel for short-term observation. The device is sandwiched between two glass substrates, and these substrates are fixed by a slide glass. The glass substrate slightly higher than the device forms the flow channel. Fig. 5.3(b) shows the top view of the device. The glass substrates are angled to hold the device in position for solution flow. The solution is injected from the larger space between the glass substrates and it flows in a single direction by capillary action. Here, flow channel height on the device is maintained to decrease the optical absorption of water. Although the solution is not sealed to prevent evaporation, the small contact area between the solution and surrounding air restricts the influence of evaporation.

Figure 5.4 shows a schematic of the flow channel for long-term observation. The flow channel system is composed of glass, silicone, and PDMS. These parts are bonded by silicone resin or the adhesion of PDMS. The device is set in the hexagonal space shown in Fig. 5.4(d). When liquid is injected into the hole in Fig. 5.4(e), capillary action moves it to the hole in Fig. 5.4(c). The caps of these holes, as shown in Figs. 5.4(f) and (g), are set to suppress evaporation of the liquid. The space in Fig. 5.4(b) allows several culture fluids to be held for long culturing times. The temperature of the system is maintained by a temperature-controlled stage. The pH is maintained by using L-15 culture without CO_2 gas. We confirmed cell culturing using this system for a week, which is evidence of the non-toxicity of this method and system. Fig. 5.5
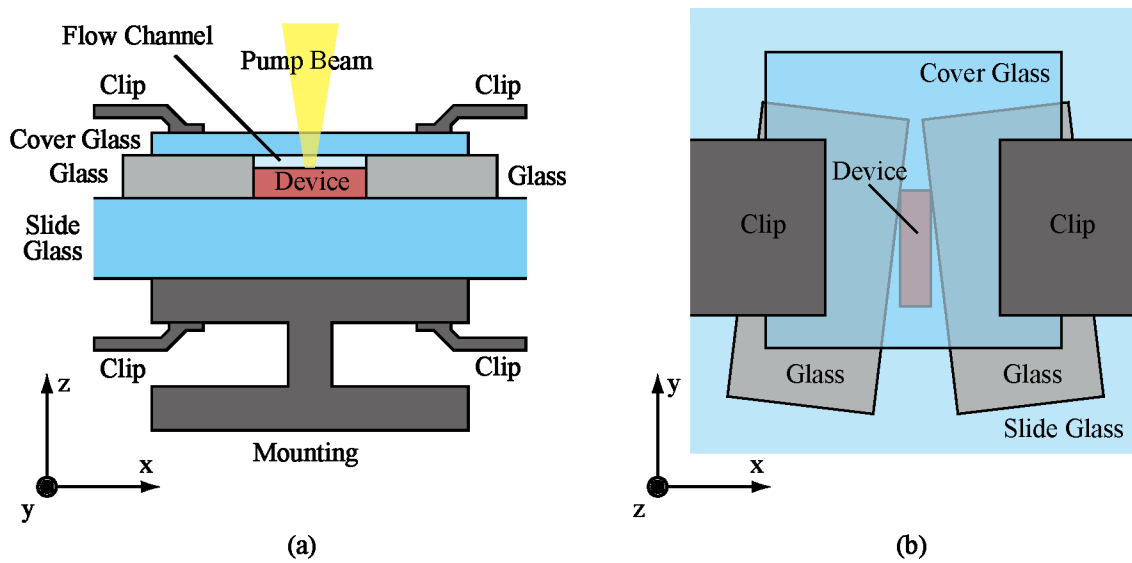
Fig. 5.3 Schematic of environment around device substrate for short-term observation: (a) side view and (b) top view.
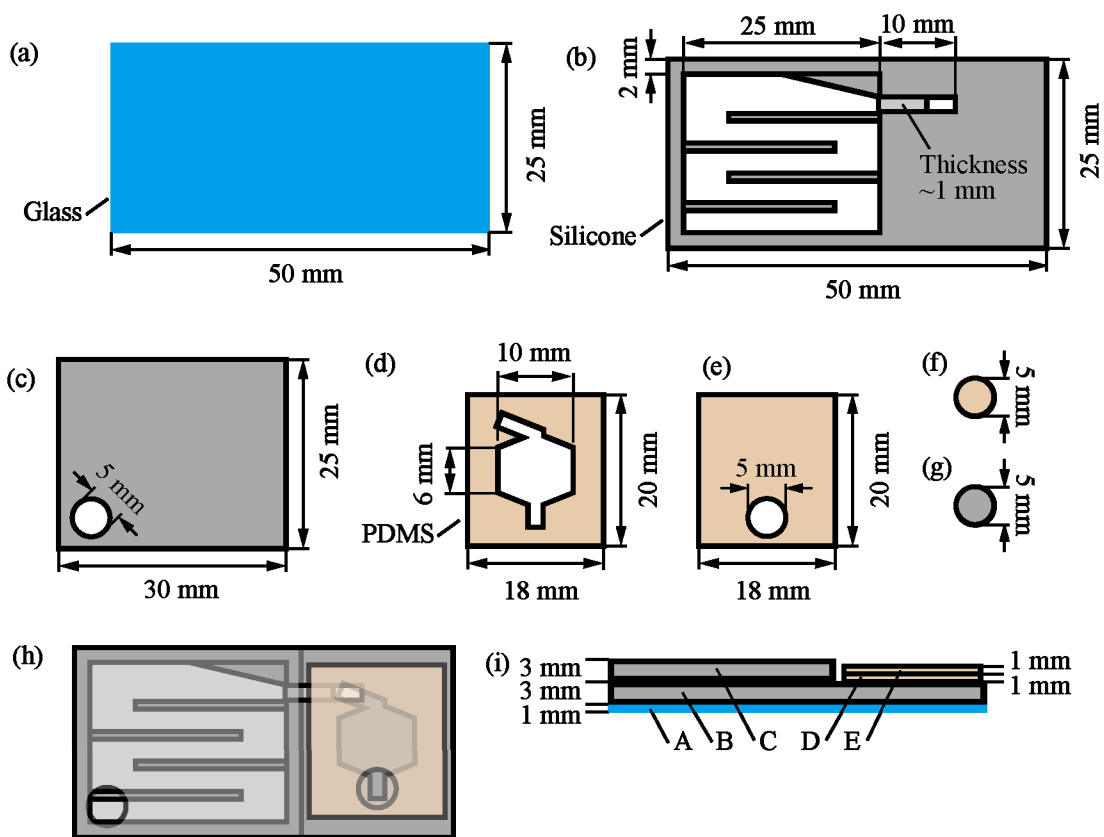
Fig. 5.4 Schematic of environment around device for long-term observation: (a)–(g) parts of system, and (h), (i) top and side views of integrated system, respectively.
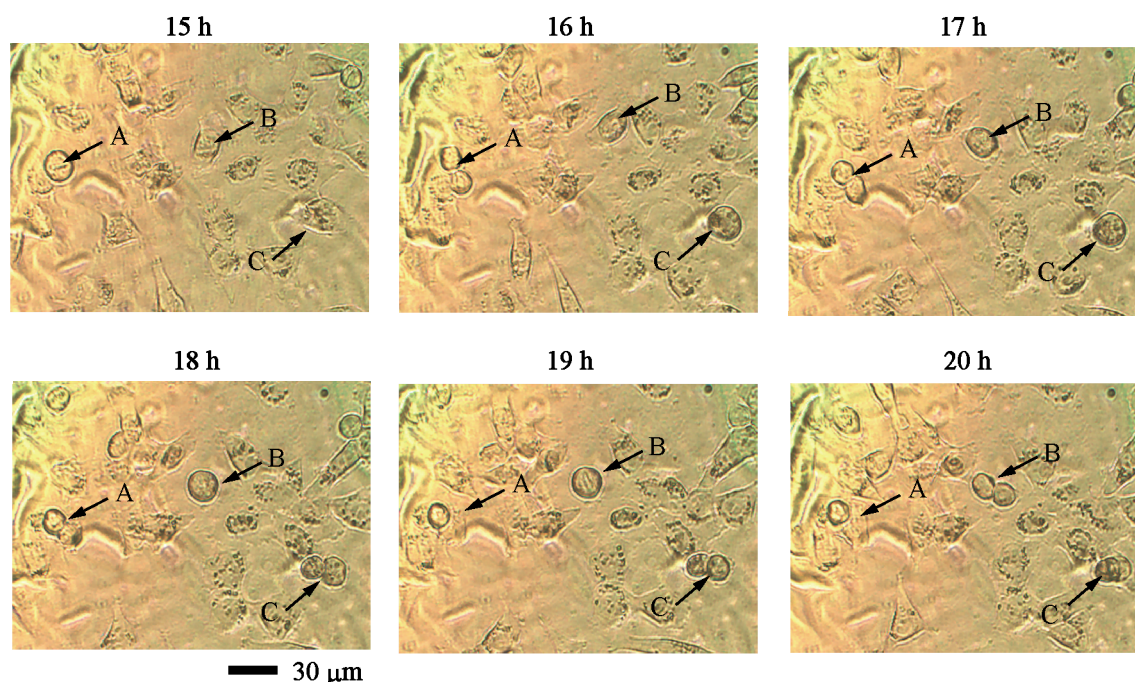
Fig. 5.5 Optical micrographs of HeLa cell culturing using setup for long-term observation.

shows continuous images of HeLa cells using the setup for long-term observation. Cells A, B, and C show cell division, and thus these images prove an appropriate environment for cell culturing.

5. 1. 4　**Lasing in nanolasers**

We measured the spectrum of each nanolaser using the measurement system described in Chap. 4 for optical alignment and the affirmation of λ. The obtained stage coordinates were used in the after the continuous measurement. The obtained λ data were used for the identification of each nanolaser from the measured spectra. In the measurement, an automatic programmable system was used. In the case without a NS nanolaser, a single-mode LD (with a spot size of ~3 μm) was used for individual measurement. In the case with an NS nanolaser, a multi-mode LD (spot size ~20 μm) was used. The measured 2-D λ data were also used as the reference λ in the tracking of λ for each nanolaser. The procedure time was ~1 h in the case of the 21 × 21 = 441 array.

5.1.5 **Tracking of wavelengths**

We tracked the λ of each nanolaser to observe continuous cellular activity. The spectra were measured repeatedly. Here, we measured nanolaser arrays one by one, or $3 \times 3 = 9$ nanolasers simultaneously for each section. Simultaneous measurement improves the frame rate of the continuous observation. Fig. 5.6(a) shows the 6×6 nanolaser array with HeLa cells. Fig. 5.6(c) illustrates the observation of the entire 6×6 nanolaser array by a combination of 3×3 used. This measurement was made using the automatic program, but some exceptional hand-operated processes were also necessary in the experiment. In the long-term measurement, disturbance of the optical alignment occurred. Therefore, we adjusted the alignment once every few hours. The measurement system shown in Figs. 5.4(a) and (b) requires an exchange of culture fluid corresponding to the evaporation of solution or pH buffer, respectively. The exchange of solution was also required during the observation of cellular reaction to reagents.

(a) (b)

(c)
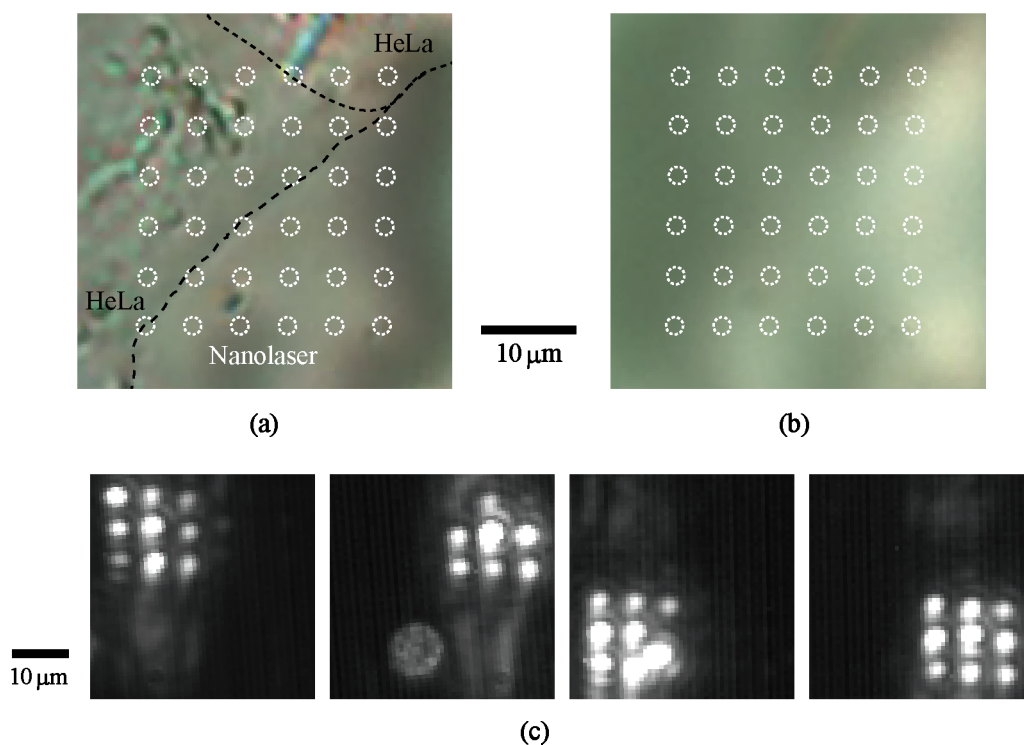
Fig. 5.6 Simultaneous measurement. (a), (b) Optical micrograph with and without cells.
(c) Near field patterns of emission from 9 nanolasers for each position.

5.1.6 **Cell reaction**

In order to observe cell reaction to reagents, we considered the appropriate reagent and cellular phenomenon for the primary cell observation. The tools used in dealing with reagents are micropipettes (capacities of 1–10, 10–100, and 100–1000 μl), tube, electronic balance (minimum measurement unit 0.0001 g), stirrer, and homothermal case. The considered reagents are described below.

Nocodazole

This reagent inhibits cellular microtubules. The microtubule known as tubulin is a kind of cytoskeleton that determines the shape of the cell. In the field of cell biology, nocodazole is used to synchronize cell cycles among cells. The cell cycle consists of the M phase, which is the period of cell division, the interphase G1 phase, in which the cells grow, the S-phase, in which the DNA is replicated, and the G2 phase, in which the preparation for cell division occurs. Because the microtubule mechanism is operant in cell division, the inhibition of microtubules by nocodazole stops the cell cycle at the M phase. Then, when nocodazole is removed, the phase of all the cells becomes the same (i.e., synchronized). In cell biology, it is known that microtubules are inhibited immediately after the administration of nocodazole. For synchronization of the cell cycle, a nocodazole concentration of 5−30 μM is used. In the case of injection with higher concentrations, cells cannot maintain their shape and ultimately shrink. Intercellular adhesions are broken by the shrinkage, and cells are removed from the attached surface.

Figure 5.7 shows the shrinking of HeLa cells from injection of a high concentration of nocodazole. The shrinking was first observed 12 min after injection. After 30 min, the majority of the HeLa cells showed shrinkage. In this experiment, the nocodazole solution was made from nocodazole powder intended for use in cell biology (Wako, Ltd.) and dimethyl sulfoxide (DMSO) (Wako, Ltd.) which can resolves nocodazole and is used for concentration adjustment of the culture fluid. This reaction involves a change in cellular shape and can be confirmed on optical micrographs. The scale of the cell change is easily observed with μm-order spatial resolution. Removal of the cells causes a large Δn and shows the $\Delta \lambda$ for the attachment of the cells. Based on the simplicity of the observation scale, nocodazole was considered appropriate for the primary experiment. Colchicine, similar agent, also inhibits microtubules but is highly toxicity.
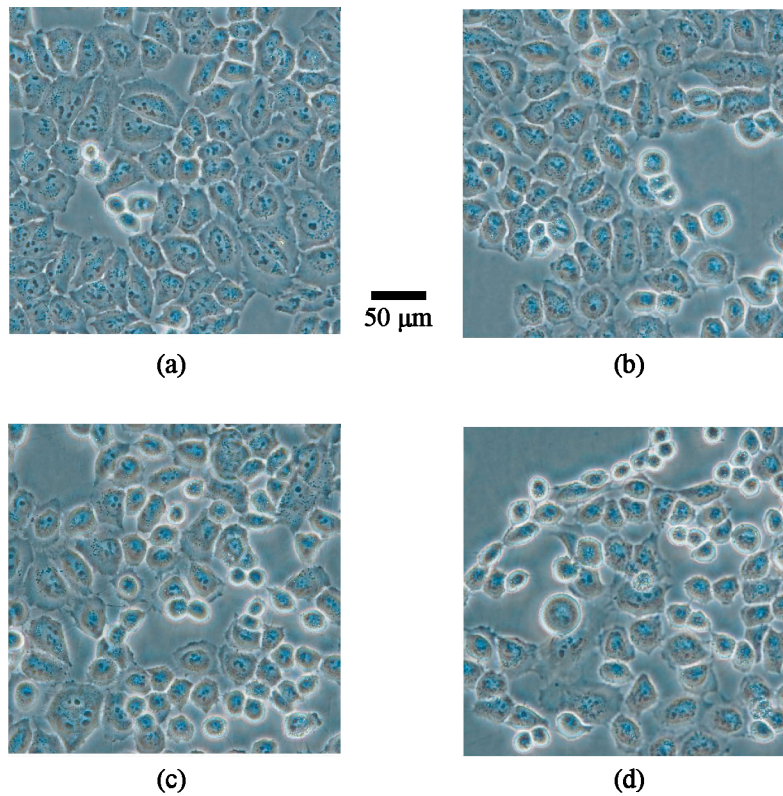
Fig. 5.7 Optical micrographs of reaction to nocodazole in HeLa cell at (a) 5, (b) 12, (c) 20, and (d) 30 min after injection. The concentration of nocodazole was 3 mM.
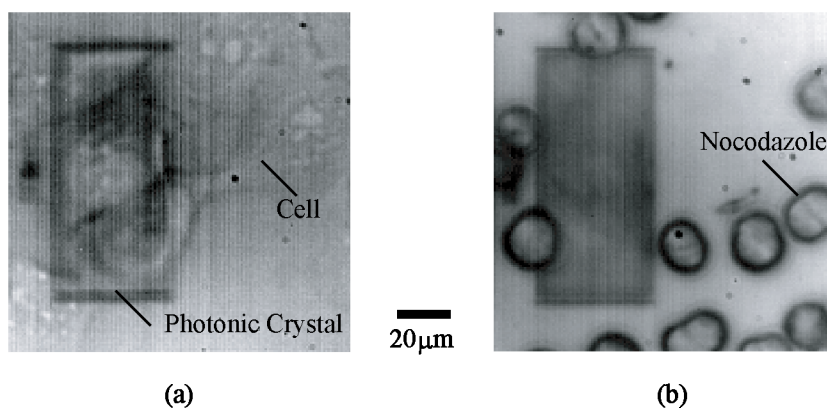
Fig. 5.8 InGaAs micrographs of the product from nocodazole: (a) before injection of nocodazole. and (b) after injection of 3.3 mM nocodazole at 10ºC.

Thus, we used nocodazole. When using high concentrations of nocodazole, the resolvability and melting point of DMSO must be considered. The melting point of DMSO is about 18°C, so

an aggregate of nocodazole may appear when the experiment temperature is low, as shown in Fig. 5.8. This makes the cellular reaction unstable. Furthermore, the shape of the resulting aggregate is similar to the cells, which becomes problematic in an experiment. Therefore, we maintained the temperature above 25°C and prepared a solution with a high of DMSO concentration (i.e.,., DMSO, 1 ml and nocodazole, 1.0 mg) to make a 3.3-mM solution. As result, the generation of aggregate was suppressed. However, the influence of the high concentration of DMSO may have emerged.

Actinomycin D

This reagent inhibits ribonucleic acid (RNA) polymerase in the cell nucleus. The cell nucleus contains DNA, which stores design information for proteins and RNA. RNA is transcribed with DNA acting as a template. RNA polymerase is the enzyme that transcribes RNA from DNA. Thus, when RNA polymerase is inhibited, protein synthesis is also inhibited. Thus, actinomycin D binds to the enzyme in the cell nucleus and inhibits various cell functions. Because HeLa cells have large nuclei, this may facilitate the observation of cell reactions. Actinomycin D is suitable in the primary experiment for the observation of organelle variations. In the experiment, actinomycin D was diluted with culture fluid and injected at 1 ng/µl. In biology experiments, it is known that the reaction is saturated for 2–3 hours at this concentration.

We considered that the cellular changes induced by these two reagents as appropriate for our observation; hence, the other techniques that we did not use are described below:

(1) Dehydration by ethanol

(2) Macro-autophagy

(3) Photo toxicity

(4) Apoptosis by hydrogen peroxide

In ethanol dehydration, cellular moisture is drawn to the outside by osmotic pressure. This method requires accurate adjustment of ethanol concentrations. Moreover, the reaction occurs too quickly, and changes of solution require manually-operated optical alignment. Therefore, this reaction is not suitable for the primary experiment.

Macro-autophagy appears when a cell reaches a starvation state or accumulates abnormal proteins. The abnormal proteins and part of the cell itself are enclosed in a phospholipid membrane called liposome. This liposomal membrane binds with a lysosome, which has a degradative function. The internal protein in liposome is decomposed into amino acids and

peptides. The size of liposome is approximately 1 μm, and direct observation is considered possible. However, it is difficult to confirm a starvation state. Therefore, this reaction was not used.

As for phototoxicity, we tried irradiation using a blue–violet (DSP-5205A) or UV pulse laser (excimer laser, 193–351 nm, 107–1010 W/cm^2, 10–20 ns). However, affirmation of variation in the cell was also difficult. Moreover, if the apoptosis would arise, it cannot be distinguished from a natural removal of the cell. Thus, this reaction was not suitable for the primary experiment.

Finally, it is known that apoptosis occurs when cells are injected with hydrogen peroxide. However, injection in a sealed condition causes the generation of air bubbles, which makes observation impossible.

5. 1. 7 **Reference wavelength**

After the tracking of wavelengths, the cells were dissociated with trypsin. Once the cells were removed, the devices were washed with culture fluids containing FBS and once again placed into the measurement system with only culture fluid. The λ of each nanolaser was measured and used as the reference λ to obtain Δλ. In the removal process, trypsin is a reagent that hydrolyzes the protein in the cell membrane. Its proteolysis is most efficient at 37°C, but in such conditions, trypsin affects the GaInAsP slab, resulting in a change in reference λ. Thus, in this process, the device chip was dipped into a trypsin-filled tube at room temperature and shaken for 5 min. Washing with FBS chemically suppresses the function of trypsin. Thus, in the case where cells were removed during the tracking of λ, the reference λ was measured after the exchange of culture fluid.

5. 1. 8 **Offline data processing**

Here, we describe the method of calculation from the measured spectra to the 2-D Δλ image. We used same the automatic systems that are described in Chap. 4, unless otherwise stated. At some instances, handling was done manually. The procedure was as follows.

(1) Calculate λ from the measured spectra and identify nanolaser positions automatically.

(2) Find correspondence between defects in the λ data and mismatches in the automatic identification.

(3) Calculate Δλ from the reference λ.

(4) Convert from Δλ to Δ*n*.

(5) Create a mapping corresponding to the nanolaser array position.

The calculation of λ from the measured spectra was based on searching for the peak λ in the spectrum and identifying the relationship between the peak λ and nanolaser position by comparing with past λ data and considering its time derivative. In this process, the λ data measured before the tracking of λ was used as the original data for identifying the relationship. Spectral measurements sometimes fail because of the instability of emissions or an optical alignment error. The obtained data for a 2-D continuous λ may contain such defects, so we compensated by using the average value of the surrounding nanolasers. Such defects or mismatches in optical alignment may also cause mismatches in the automatic identification. These mismatches were identified by extraordinary wavelength hopping or periodic data defects. We then checked the optical alignment, compensated the nanolaser position in the 2-D λ data, and corrected the initial 2-D λ data, which were used in the identification of nanolaser positions. We also tried wavelength tracing using various timings to suppress the influence of instability in the lasing.

The Δλ data were calculated using the reference λ that was measured after the removal of cells. The conversion from Δλ to Δn was calculated from a preliminary measurement of A. We measured A for each nanolaser to suppress distortion from the nonuniformity in A. The mapping was done corresponding to the measurement positions and identification using λ.

5.2 Wavelength-based image

Figure 5.9 shows optical micrographs of the attached HeLa cells and corresponding Δλ images both with and without cells for four different samples (A–D). Here, the setup for short-term observation was used. Single-LD excitation was used in the wavelength tracking. The condition of the device used was a 21 × 21 nanolaser array on an integrated scale, 5-μm pitch, cavity without NS, and bonding structure. These micrographs show flatly attached cells. Some similarities between the micrographs and Δλ images were observed. For example, sample A shows two cells attached separately. The Δλ image shows a similar shape, but the distribution within the cells was slightly nonuniform and did not correspond to the organelle distribution; the nonuniformity was greater than 1 nm in the Δλ image. Such nonuniformity is more evident in other samples. Sample B shows a complicated image including cell-to-cell adhesion. The round cells show smaller redshifts in the Δλ image. Such round shapes indicate weak attachment. Cell-to-cell adhesion also influences the cell-to-device attachment. Samples C and D show more nonuniform patterns. The cells with cell-to-cell adhesion show more nonuniform distribution than those without. Because the evanescent field of the nanolasers can only detect behaviors
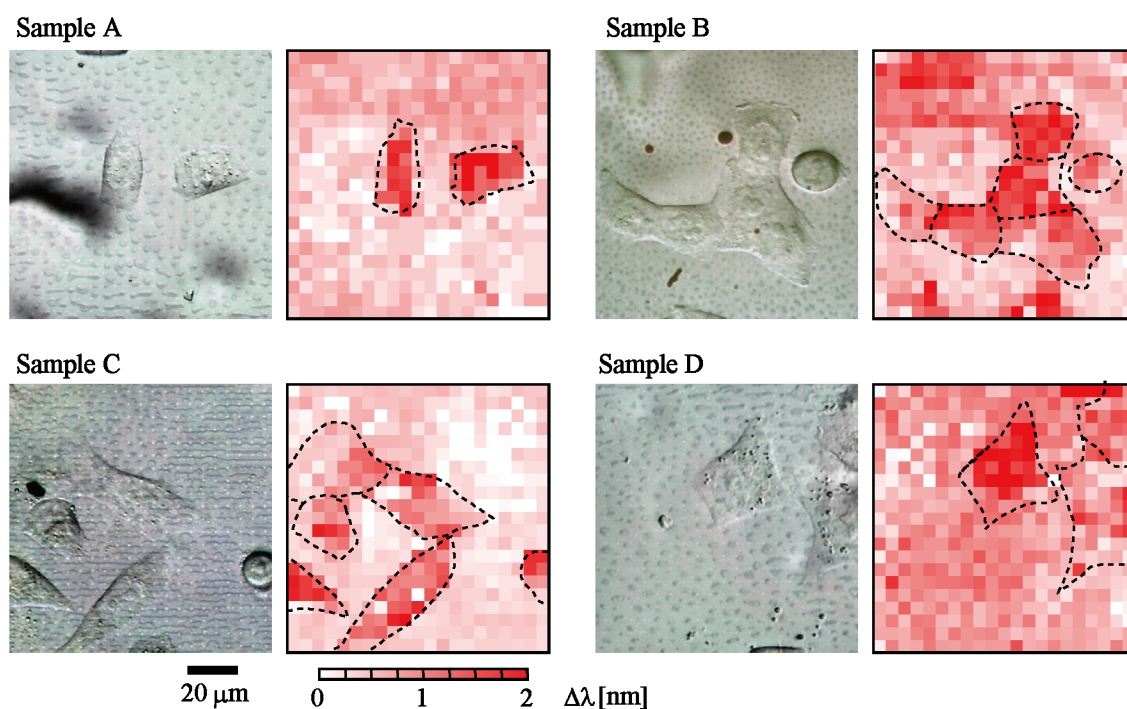
Fig. 5.9 Observation of HeLa cells attached on a nanolaser array and snapshots for samples A–D. Left and right panels for each sample show optical micrographs and $\Delta\lambda$ images, respectively. Dashed lines depict the cell boundaries. [5-4]

within their penetration depth from the device surface into the fluid and cells (~120 nm), the $\Delta\lambda$ image might reflect the attachment condition determined by the footing of the cells.

Figure 5.10 shows the time evolution of the $\Delta\lambda$ image. Here, the setup for short-term observation was used. Single-LD excitation was used during wavelength tracking, and the DMEM was exchanged repeatedly during the measurement to compensate for the evaporation of volatile elements. The condition of the device used was a 21×21 nanolaser array on an integrated scale, 5-μm pitch, cavity without NS, and bonding structure. When the culture fluid was exchanged, all λs showed a constant shift owing to slight changes in the concentration and temperature of the fluid. This shift was neglected. As observed, the redshift pattern gradually changes during the 150-min measurement. Three cells, A, B, and C, show different changes: small changes, spreading of the pattern, and an increase in redshift, respectively. Referring to the discussion for Fig. 5.9, it is reasonable to believe that the larger change is mainly due to a local change in the attachment condition of the cells.
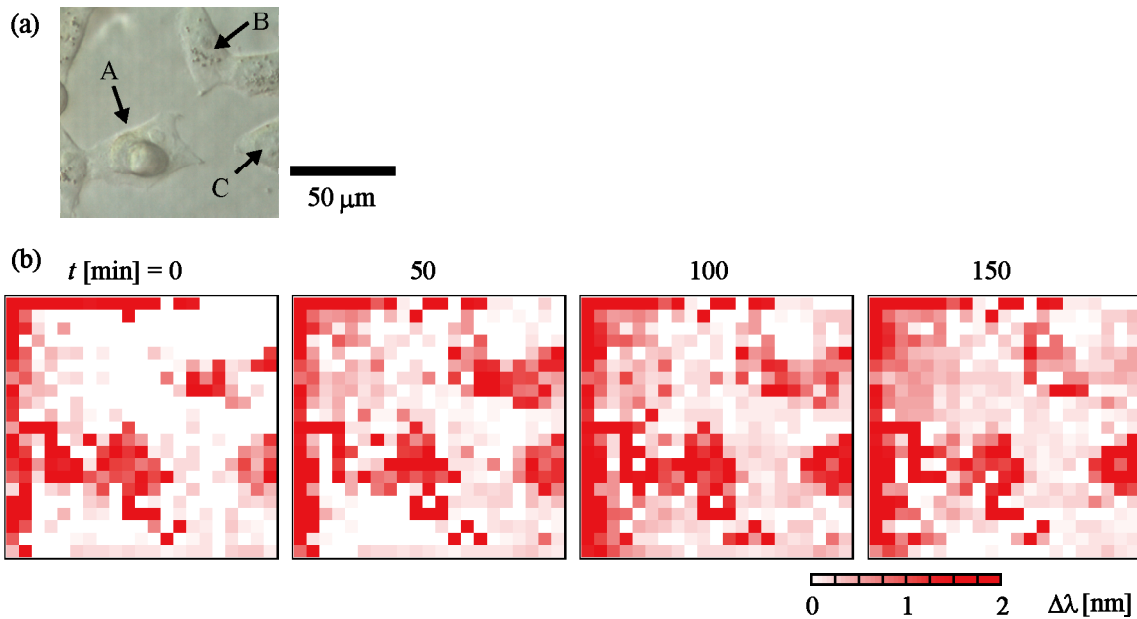
Fig. 5.10 Continuous observation of HeLa cells attached on a nanolaser array: (a) optical micrograph, and (b) continuous $\Delta\lambda$ image. [5-4]

5. 3 Cell reaction

Figure 5.11 shows optical micrographs and near-field lasing patterns in the observation of cell reactions. These optical micrographs show that the entire surfaces of the samples were covered with cells. Here, the setup for short-term observation and the multimode-LD excitation were used in the tracking measurement. The condition of the device used was a 5×5 nanolaser array on an integrated scale, 2.5-μm pitch, cavity without NS, and air bridge structure. A 0.41-mM nocodazole and 0.80-μM actinomycin D solution was injected. In this experiment, the optical alignment was manually adjusted. Comparing the samples before and after the injection of nocodazole, the cell changed from being in a flattened state to a shrunken state. The image after the injection of actinomycin D is an InGaAs camera image instead of an optical micrograph. This shows cellular adhesion similar to that before the injection.

Figure 5.12 shows the tracking of $\Delta\lambda$ for each nanolaser without compensating for the injection and evaporation of reagent. Here, the nanolaser array was not treated with the wavelength control process, so that this plot contains an error from the overlap of spectra, and identification using the λ of each nanolaser was impossible. This shows the continuous variation of each nanolaser. Before the reagent was injected, λ was stable to less than ±1 nm, taking into account cell variations and structured nonuniformity. This is evidence that the behavior of cells,
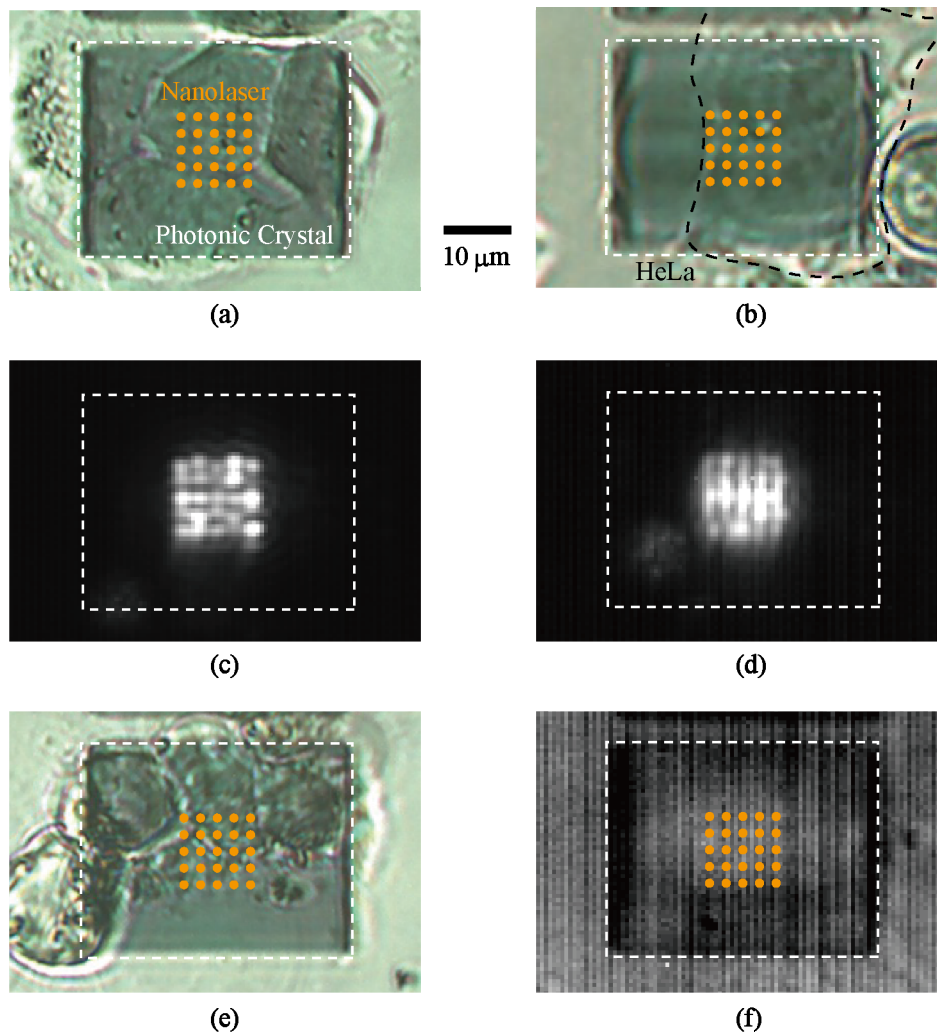
Fig. 5.11 Optical micrographs and near-field patterns of cell reactions to reagents: (a),(b) before the injection of reagents, (c), (d) lasing pattern during the experiment, and (e), (f) after the experiment. The left and right panels show the experiments with nocodazole and actinomycin D, respectively. The concentrations of nocodazole and actinomycin D are 0.41 mM and 1 ng/ml, respectively.

thermal shifts, and evaporation are almost negligible in such a short measurement. With the injection of nocodazole, as shown in Fig. 5.12(a), the condition of λ varied corresponding to the injection of reagent. After the injection, most of the λ redshifted immediately due to a change in the liquidity index.

However, the shift amounts are different between devices. This difference might be due to the nonuniform attachment strength of the cells. Subsequently, λ quickly blueshifted within ~500 s and finally became stable. This blueshift is generally larger when the immediate redshift
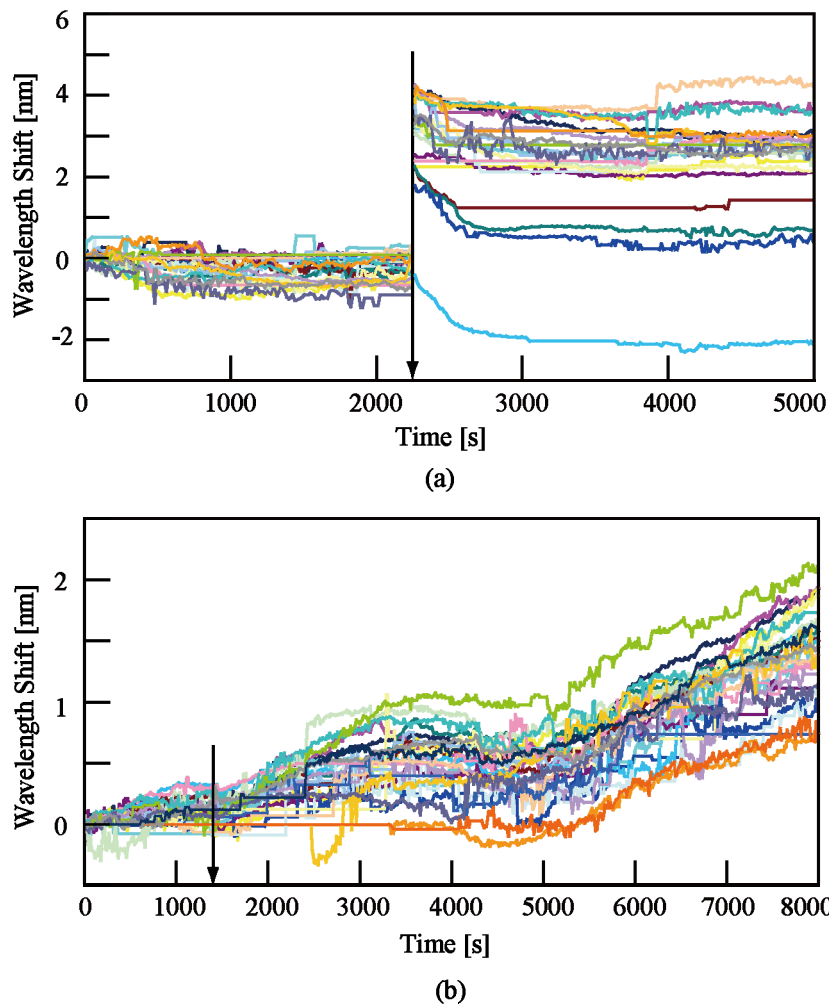
Fig. 5.12 Nanolaser spectral shifts for two reagents: (a) nocodazole and (b) actinomycin D. Reagent injection times are indicated by arrows. [5-4]

is larger, although some exceptional cases were also observed. Therefore, we consider that this blueshift arises from a pure reaction of the cells against nocodazole. Nocodazole is known to bind to tubulin within several seconds [5-2] and make microtubules rapidly depolymerized [5-3]. When the actinomycin D was injected, λ did not show an immediate change because the solution had an index similar to that of the culture fluid. Then, λ redshifted within ~3500 s and became stable, followed by a second redshift at $t = 5000$ s. The first shifts were nonuniform between devices, whereas the second ones have almost the same slope. This suggests that first shifts were mainly due to the reactions in the cells, whereas the second ones were due only to the evaporation of volatile elements. As a result, we successfully observed the cellular reaction against the injection of the reagent. We thought that such observation can be applied to cell screening cells. By considering the sensing depth, the variation around the cellular membrane

should make large $\Delta\lambda$. This also indicates that this method is suitable for the observation of the proteins around the cellular membrane. It is known that such proteins around the membrane play an important role in the interaction with extracellular environment.

5．4　Conversion to index-based image

Figure 5.13 shows the HeLa cells before and after continuous observation. Samples A and B indicate cell movement or desorption. Here, the setup for long-term observation was used. Single-LD excitation was used during the wavelength tracking. The condition of the device used was an 11 × 9 or 11 × 11 nanolaser array on an integrated scale, 5-μm pitch, cavity with NS, and bonding structure. Fig. 5.14 indicates the time evolution of the image, which partially corresponds to the cellular behaviors in the optical micrograph. Here, the gradation of the color bar corresponds to the absolute accuracy of the refractive index. When the color scale was changed in sample A, we realized that the cell on the left side moved more frequently than the one on the right. Because the lamellipodium on the left side moved out of the observation frame, such frequent movement might reflect the activity of the cell. Sample B shows an Δn image for cells that were finally desorbed from the device. The Δn image disappeared gradually from the lower to the upper side of the cell image. This temporal change must be due to a chain reaction of the local adhesion. Such variations were not observed in the resolution before an improvement of $\sim 10^{-2}$ (refractive index resolution (RIU). The observation of these minute Δn values was enabled by the improvement.

5．5　High frame-rate

Figure 5.15(a) shows the optical micrograph of the HeLa cells attached on the nanolaser array. This displays the cellular attachment all over the nanolaser array. Here, the setup for long-term observation and the multimode-LD excitation was used in tracking λ. The integration scale of the used device was a 3 × 3 array with a 4.5-μm pitch. The nanolaser without NS, after the post-λ trimming, and the air bridge structure was used. Fig. 5.15(b) shows an example of the spectra measured in the tracking procedure. The spectral peaks were aligned with spacings sufficient for the spectral identification. We then measured the spectra of nine nanolasers simultaneously, with a frame time of 2.3 – 2.8 s. Fig. 5.15(c) shows the continuous trace of λ for each nanolaser. Here, the nanolaser array with a spectral pitch of 2.5 nm was used. This shows that almost of λ were separated but some were overlapping in spectra. This frequency of the overlap is sufficiently low to identify by the automatic program. From this result, we succeeded in the improvement of the frame rate by the λ trimming. To get more image pixels, maintaining

Sample A
0 h   10 h

Sample B
0 h   10 h

HeLa

20 μm   20 μm
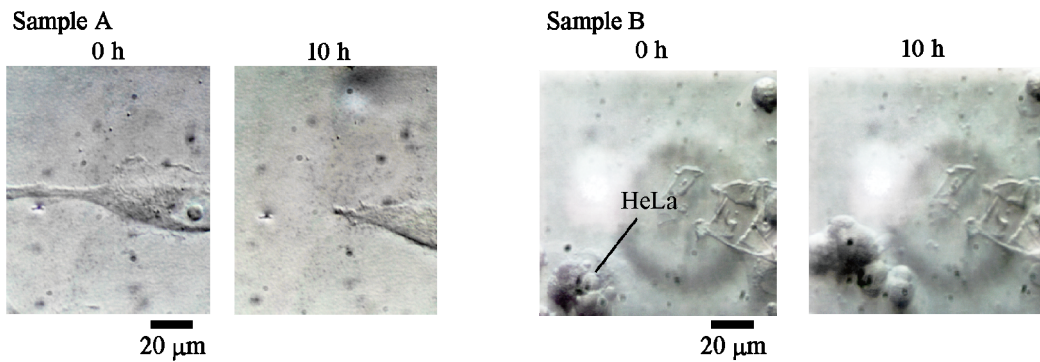
Fig. 5.13 Optical micrograph of index-based imaging. Panels present the before- and after-measurement images for each sample. Samples A and B show moving cells and cells finally desorbed, respectively. [5-4]

Sample A
0 h   4 h   8 h   10 h

0   20   40 Δn [×10⁻³RIU]

Sample B
0 h   4 h   8 h   10 h

0   10   20   30 Δn [×10⁻³RIU]
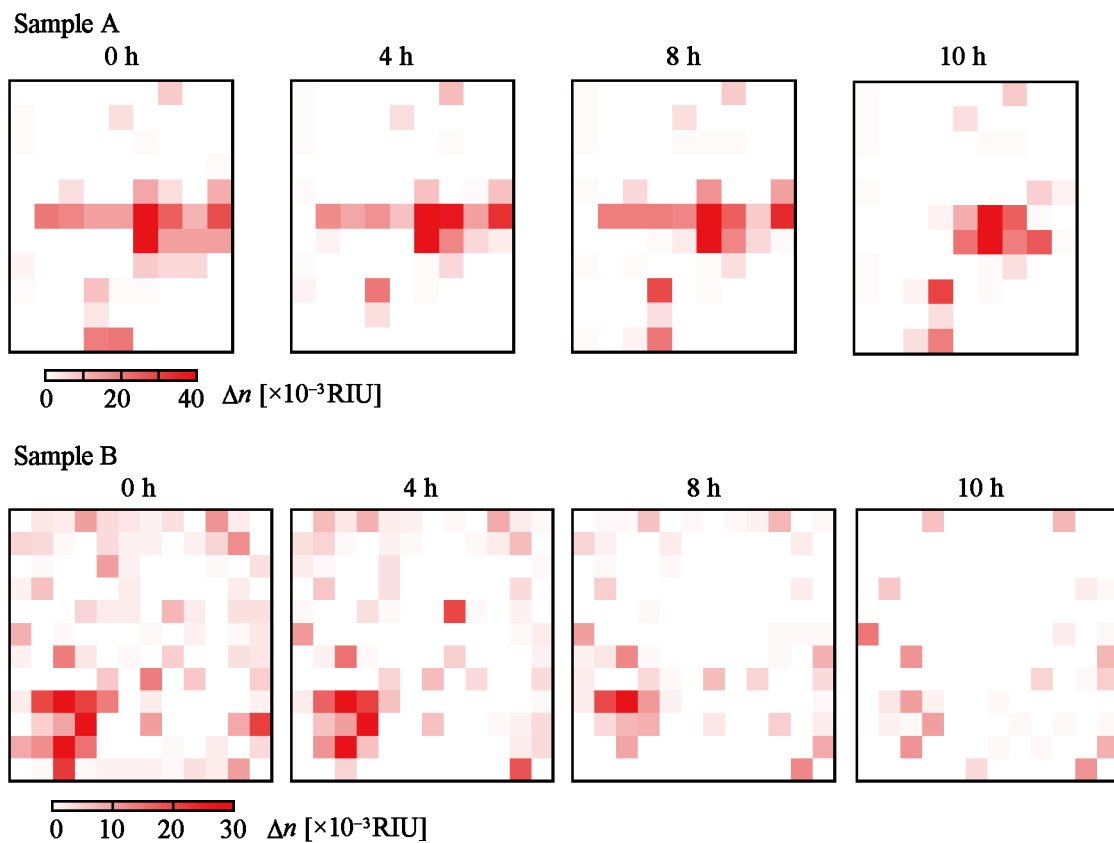
Fig. 5.14 Time evolution of HeLa cells observed in the NS nanolaser array. Samples A and B correspond to Fig. 5.13. [5-4]
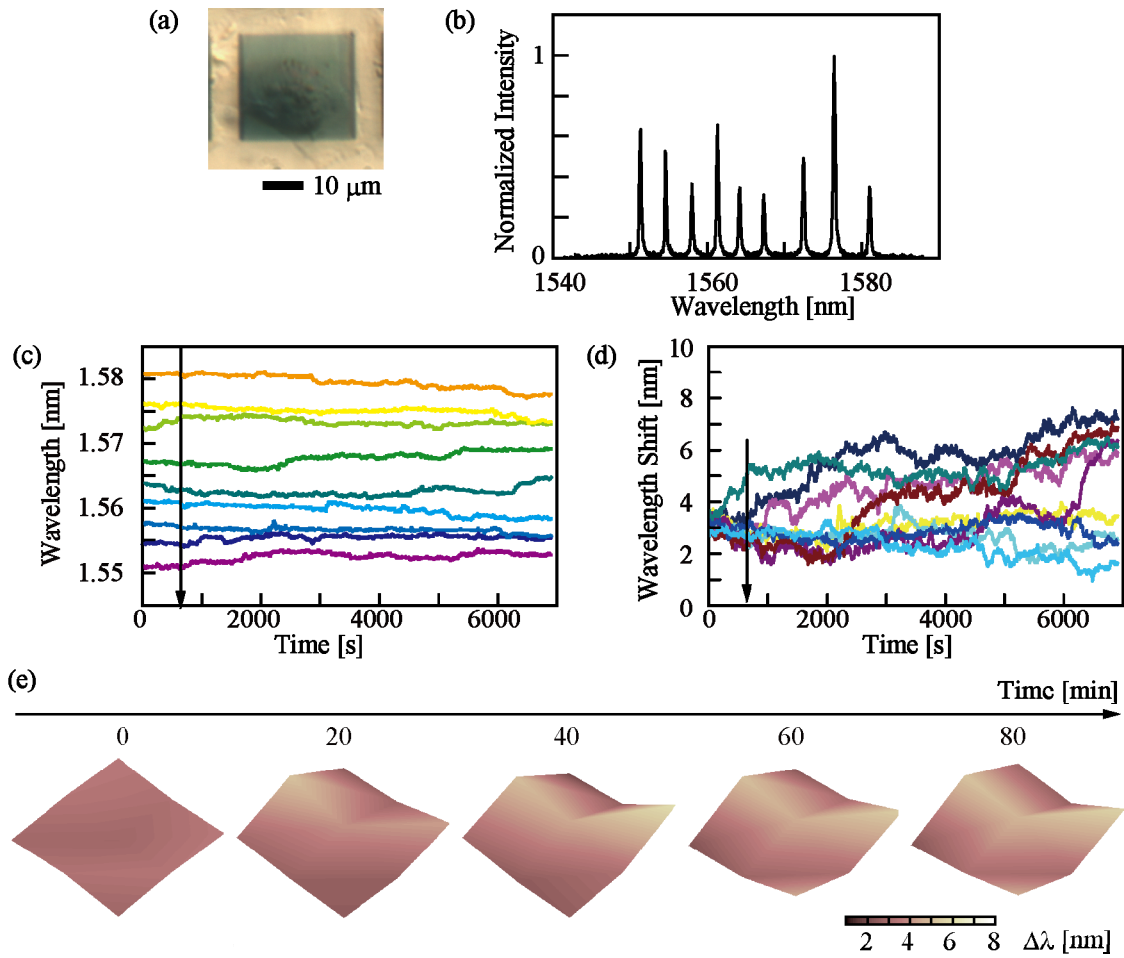
Fig. 5.15 Cell observation with high frame rate: (a) HeLa cells attached on nanolaser array, (b) spectrum measured in tracking, (c), (d) time evolution of λ and Δλ, respectively, and (e) 3-D contour map of (d). Arrows indicate the injection of actinomycin D (1 ng/ml).

the standard spacing of 2.5 nm in the spectrum, a wider spectral bandwidth of the material emission is necessary. In GaInAsP, the bandwidth is <200 nm, so that the number of pixels will be limited to <80. To realize a more pixels with a high frame rate, the introduction of a parallel measurement such as that using a bundle optical fiber instead of the single optical fiber and multi spectroscope will be required. The Δλ was calculated from the reference λ, as shown in Fig. 5.15(d). This shows the time evolution of the redshift caused by actinomycin D. Compared with Section 5.3 showing the reaction of the same reagent, the behaviors of the red shifts were not uniform among the nanolasers. This might reflect the individual specificity between cells and/or the widening of the pitch between nanolasers. This result also shows larger Δλ (several nm) than other cell observation results (< ~ 2 nm). To know the reason of this large shift, we checked the variation of the sensing property after the trimming process. Fig. 5.16(a) shows
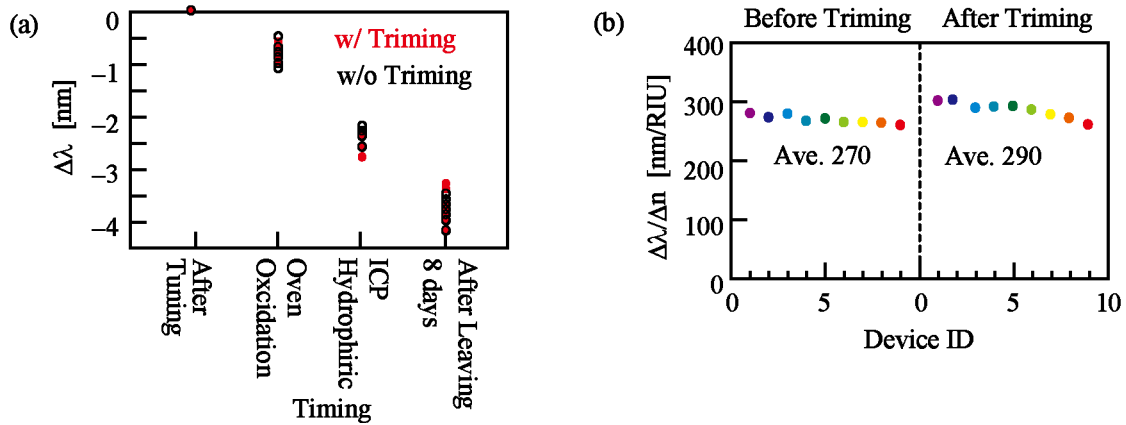
Fig. 5.16 The variation in lasing characteristics by λ trimming. (a) Aging variation during the preparation. (b) Sensitivity between before and after λ trimming. The color of the plots indicates same designing nanolaser in the same chip.

the spectral shifts during the preparation process of nanolasers. Fig. 5.16(b) shows the comparison of A between before and after the trimming. They show a diffence of only less than 10% in A. These variations were sufficiently small to compare the results. Thus, we consider this large shift to be reflected from the other physical variations such as the removal of the protein from the device surface. We observed the details of this redshift and calculated the continuous mapping images, as shown in Fig. 5.15(e). In this experiment, because of the extension of the exposure time in the spectral detection in the photodetector array, the result indicates a lower frame rate than the ideal one of second order. However, the frame rate was still sufficient to observe the details of the redshift reflecting the reagent. Such detailed observation was thought to be applicable to cell screening.

5.6 **Discussion**

The Δλ images for the resist coating and cultured HeLa cells corresponded roughly to those observed in the optical micrographs. Next, we converted the Δλ images to Δn images by introducing a nanoslot into each nanolaser. We demonstrated a $12 \times 12 = 144$ array with a 100% yield and improved the index resolution to ~2×10^{-3} RIU, which was a five-fold improvement over that without the NS. Cell images thus obtained mainly reflected the attachment condition of the cells on the nanolaser, which is usually difficult to observe in an optical micrograph. Further investigation of the correspondence between the image and actual cellular behavior is expected in future studies.

For an image sensor, three constraints must be cleared for progress to continue. The first

constraint is the spatial resolution determined by the nanolaser pitch. Without an NS, the laser mode was distributed over a ~2-μm diameter area, which determined the minimum pitch. This is not sufficiently small for the observation of detailed cellular behaviors but may be applicable to some macroscopic observations. The second constraint is the readout time of all λ values: at present, the readout time of one frame is more than 10 min for large arrays (over 100). An optical system allowing parallel pumping and readout may be a solution for this. Another alternative would be to focus on a smaller array with parallel pumping and readout, allowing the capture of rough cell images at a video frame rate. It would be helpful if the index resolution could be further improved or if the image could detect delicate behaviors such as the emission of secretory proteins. Thus, the third constraint is the index resolution, which is currently limited to ~1×10^{-2} RIU without a nanoslot. For higher index resolutions, the nanoslot must be incorporated, although it would result in a larger modal area and lower spatial resolution. However, the resolution is still limited to ~2×10^{-3} RIU, for which further optimization of the cavity structure, laser mode, and fabrication process are necessary.

References

[5-1]   I. H. Goldverg, M. Rabinowitz, and E. Reichi, "Basis of actinomycin action, I. DNA binding and inhibition of RNA-polymerase synthetic reactions by actionomycin," *E. Biochemistry*, vol. 48, pp. 2094–2101, 1962.

[5-2]   J. Head, L. L.-Y. Lee, D. J. Field, and J. C. Lee, "Equilibrium and rapid kinetic studies on nocodazole-tubulin interaction" *J. Biol. Chem.*, vol. 260 , no. 20, pp. 11060-11066, 1985.

[5-3]   T. L. Karr, D. Kristofferson, and D. L. Purich, "Mechanism of microtubule depolymerization" *J. Biol. Chem.*, vol. 255, no. 18, pp. 8560-8566, 1980.

[5-4]   H. Abe, M. Narimatsu, T. Watanabe, T. Furumoto, Y. Yokouchi, Y. Nishijima, S. Kita, A. Tomitaka, S. Ota, Y. Takemura and T. Baba, "Living-cell imaging using a photonic crystal nanolaser array," *Opt. Express*, vol. 23, no. 13, pp. 17056-17066, 2015.

Chapter 6
Conclusion

In this study, we propose and demonstrate a novel cell imaging method using a photonic crystal nanolaser array. We developed and improved the device, system, and imaging performance and demonstrated its functionality.

First, we proposed the principle of the particular imaging method that has a high throughput owing to the label-free sensing mechanism, minute spatial resolution of $< 1\mu m^2$, high resolution of the refractive index, sufficient signal intensity for low penetration into cells, and a fast measurement frame rate. By including these features, we expected to find solutions to the problems encountered with existing methods. With due consideration of the factors limiting imaging performance, we adopted the key technologies required to improve this method, aiming toward practical cell imaging.

We fabricated the nanolaser array using the GaInAsP/InP wafer process. In this process, the resistant pattern, formed by EB lithography, is transferred to the GaInAsP layer, and any unnecessary layers are removed. We developed this process for a large area device by bonding the GaInAsP layer to a glass substrate, thereby solving the problem of fragility of previous air-bridge structures. The observation area was improved from 25 μm^2 to >100 μm^2, which enabled the examination of a whole human cell. We were able to control the PC hole diameter, enabling the selection of a resonant mode and suppression of the coupling between nanolasers; this enabled the independent operation of the nanolaser and worked as the imaging pixel. We developed a method to control the wavelength of the nanolaser. In this method, the wavelength was designed in the ~90-nm range using the diameter of the holes that formed the H0 cavities. Moreover, we introduced a nanoslot structure in the cavity of the nanolaser array to improve the refractive index resolution. We also developed the post-process by trimming the wavelength of an arbitrary nanolaser in the array. During this process, the nanolaser array was put in a dilute HCl solution and pumped by irradiation with pumping light. We aligned the wavelength of the nanolaser array with a pitch of 2.5 nm by a post-trimming process, which enables the observation with a second order frame rate.

We confirmed the fundamental property of the fabricated device. We measured and observed the laser's sensing and imaging properties. The nanolaser array lased with a 100% emission

yield. We demonstrated the imaging results by the observation of the test pattern. In the test experiment, the boundary of the wavelength shift and a droplet on the nanolaser array matched. We also demonstrated the acquisition of the refractive index shift using the wavelength shift and sensitivity. Compensation for the non-uniformity of the sensitivity of an array suppresses the distortion in the acquired index shift. The practical sensitivity was averaged to 97 nm/RIU in the NS nanolaser and 57 nm/ RIU in the simple nanolaser. The absolute accuracy of the refractive index resolution was ~2.0 × 10^{-3} RIU in the NS nanolaser and ~ 10^{-2} RIU in the simple nanolaser. Moreover, we developed an imaging system that automates the measurement of a large-scale integrated nanolaser array and associated data processing.

To demonstrate the cell imaging, a procedure was developed. We prepared the device as follows: HeLa cells were attached to the surface of the device, the device was then attached to the measurement system, the wavelength of each nanolaser was repeatedly measured, the reagents were injected to the culture solution to induce cell reaction, the cells were then removed with trypsin, each nanolaser measured again for the reference wavelength, and the wavelength shift corresponding to the nanolaser position mapped. We successfully acquired images of the wavelength shift that matched the shape of the cells. The acquired image and its time evolution is thought to reflect the conditions of the cell and cell attachment. We also demonstrated the acquisition of a refractive index shift image and video using the NS nanolaser array. The image, with a refractive index resolution of 10^{-4} RIU, shows the vibration in the index signal, i.e., the frequency of which may reflect the cell condition. We attempted to observe cell reaction at a high frame-rate using the nanolaser array with wavelengths aligned by the post-trimming process. The time evolution of ~2 s/frame showed minute dynamic information associated with cell reaction.

Following these studies, we intend to propose and develop a novel method with a label-free, high-spatial resolution, high intensity signal, and an index resolution sufficient to observe cell conditions and demonstrate cell imaging. However, the resolution is still limited to ~2.0 × 10^{-3} RIU, so the further optimization of the cavity structure, laser mode, and fabrication process are necessary. In future, the contribution to cell imaging technology is expected to develop with further improvements in spatial and refractive index resolution.

Acknowledgements

Publication list

Journal papers

Full papers

[1] H. Abe, M. Narimatsu, T. Watanabe, T. Furumoto, Y. Yokouchi, Y. Nishijima, S. Kita, A. Tomitaka, S. Ota, Y. Takemura and T. Baba, "Living-cell imaging using a photonic crystal nanolaser array," *Opt. Express*, vol. 23, no. 13, pp. 17056-17066, 2015.

Letters

[1] T. Watanabe, H. Abe, Y. Nishijima and T. Baba, "Array integration of thousands of photonic crystal nanolasers", *Appl. Phys. Lett.*, vol. 104, no. 12, pp. 121108, 2014.

[2] M. Narimatsu, S. Kita, H. Abe and T. Baba,"Enhancement of vertical emission in photonic crystal nanolasers," *Appl. Phys. Lett.*, vol. 100, no. 12, pp. 121117, 2012.

International conferences

[1] T. Baba, S. Kita, H. Abe, S. Hachuda, M. Narimatsu, S. Otsuka and K. Nozaki, "Photonic crystal nanolasers with nanoslot structure for sensing applications", *SPIE Optics and Photonics*, San Diego, no. 8095-30, 2011 (Invited Paper).

[2] H. Abe, M. Narimatsu, S. Kita, A. Tomitaka, Y. Takemura and T. Baba, "Live cell imaging using photonic crystal nanolaser array", *Int. Conf. Miniaturized Sys. Chem. Life Sciences (micro-TAS)*, Seattle, pp. 1433-1435, 2011.

[3] H. Abe, T. Furumoto, M. Narimatsu, S. Kita, K. Nakamura, Y. Takemura and T. Baba, "Cell imaging using large-scale photonic crystal nanolaser array", *IUMRS-Conf. Electron. Mat.*, Yokohama, no. B-9-O25-009, 2012.

[4] M. Narimatsu, S. Kita, H. Abe and T. Baba, "Greatly enhanced vertical emission in photonic crystal nanolasers", *IUMRS-Conf. Electron. Mat.*, Yokohama, no. B-9-O25-011, 2012.

[5] H. Abe, T. Furumoto, M. Narimatsu, S. Kita, K. Nakamura, Y. Takemura and T. Baba, "Direct live cell imaging using large-scale nanolaser array", *IEEE Sensors,* Taipei, no. 1565,

2012.

[6] <u>H. Abe</u>, M. Narimatsu, S. Kita, K. Nakamura, S. Ota, Y. Takemura, and T. Baba, "Label-free imaging of live cell using large-scale photonic crystal nanolaser array", *SPIE Photonics West,* San Francisco, no. 8594-4, 2013.

[7] <u>H. Abe</u>, T. Watanabe, Y. Nishijima, S. Ota, Y. Takemura and T. Baba, "Photonic crystal nanolaser array for the observation of time evolution in live cells", *Conf. Laser & Electro-Opt. Pacific Rim and Optoelectronic & Commun. Conf. / Photonics Switching,* Kyoto, no. TuJ2-4, 2013.

[8] T. Watanabe, <u>H. Abe</u>, T. Watanabe, Y. Nishijima and T. Baba, "Over one thousand large-scale array integration of photonic crystal nanolasers", *Conf. Laser & Electro-Opt. Pacific Rim and Optoelectronic & Commun. Conf. / Photonics Switching,* Kyoto, no. ThI1-1, 2013.

Domestic conferences

[1] <u>阿部紘士</u>, 成松道正, 北翔太, 冨高あさひ, 竹村泰司, 馬場俊彦, "フォトニック結晶ナノレーザアレイによる細胞マッピングの点数増加", 応用物理学会秋季講演会,15a-ZW-19 2010.

[2] <u>阿部紘士</u>, 北翔太, 横内康之, 冨高あさひ, 竹村泰司, 馬場俊彦, "フォトニック結晶ナノレーザアレイによる細胞のリアルタイムマッピングの提案", 応用物理学会春季講演会, 19a-ZD-4 2010.

[3] <u>阿部紘士</u>, 北翔太, 馬場俊彦, "フォトニック結晶ナノレーザの波長チャーピングを利用した波長スイーパ", 応用物理学会秋季講演会, 8p-B-10 2009.

[4] 成松道正, <u>阿部紘士</u>, 北翔太, 冨高あさひ, 竹村泰治, 馬場俊彦, "細胞直接観察のための多波長フォトニック結晶ナノレーザアレイ", 応用物理学会秋季講演会, 16p-J-11 2010.

[5] 馬場俊彦, 北翔太, 羽中田祥司, 大塚翔太, <u>阿部紘士</u>, 成松道正, "フォトニック結晶ナノレーザを用いたバイオセンシング", 電子情報通信学会総合大会, no. CI-1-10, 2011 (招待講演).

[6] 成松道正, <u>阿部紘士</u>, 北翔太, 冨高あさひ, 初貝晋典, 竹村泰司, 馬場俊彦, "フォトニック結晶ナノレーザアレイによる細胞観察の試薬による違い", 応用物理学会春季講演会, no. 25a-CB-3, 2011.

[7] <u>阿部紘士</u>, 成松道正, 北翔太, 初貝晋典, 冨高あさひ, 竹村泰司, 馬場俊彦, "細胞観察用フォトニック結晶ナノレーザアレイの大規模化", 応用物理学会春季講演会, no. 25p-KA-4, 2011.

[8] 馬場俊彦, 北翔太, 羽中田祥司, 大塚翔太, <u>阿部紘士</u>, 成松道正, "フォトニック結

晶ナノレーザ---究極のナノスロット構造とその応用”, 応用物理学会春季講演会, no. 26p-BN-8, 2011 (招待講演).

[9]　成松道正, 北翔太, 阿部紘士, 馬場俊彦, “フォトニック結晶ナノレーザの放射パターン制御”, 応用物理学会春季講演会, no. 16a-E5-3, 2012.

[10]　阿部紘士, 古本哲久, 成松道正, 北翔太, 中村洸介, 竹村泰司, 馬場俊彦, “細胞観察に向けたフォトニック結晶ナノレーザアレイの大面積化”, 応用物理学会春季講演会, 2012.

[11]　阿部紘士, 古本哲久, 成松道正, 北翔太, 中村洸介, 竹村泰司, 馬場俊彦, “フォトニック結晶ナノレーザアレイによる細胞イメージングの広範囲化”, 応用物理学会春季講演会, no. 17a-F8-2, 2012.

[12]　渡邊敬介, 北翔太, 岡村直柔, 阿部紘士, 磯野俊成, 馬場俊彦, “フォトニック結晶ナノレーザの吸着電荷による発振波長シフトの検証”, 応用物理学会秋季講演会, no. 12a-H3-11, 2012.

[13]　阿部紘士, 成松道正, 北翔太, 中村洸介, 大多哲史, 竹村泰司, 馬場俊彦, “大規模フォトニック結晶ナノレーザアレイを用いた細胞観察像と細胞定着状態の関係”, 応用物理学会秋季講演会, no. 12p-H3-9, 2012.

[14]　渡部工, 阿部紘士, 西島喜明, 馬場俊彦, “1000 個を越えるフォトニック結晶ナノレーザの大規模アレイ集積”, 応用物理学会春季講演会, no. 28p-C1-14, 2013.

[15]　阿部紘士, 渡部工, 大多哲史, 竹村泰司, 馬場俊彦, “フォトニック結晶ナノレーザアレイを用いた細胞の経過観察”, 応用物理学会春季講演会, no. 29a-G17-7, 2013.

[16]　渡部工, 阿部紘士, 西島喜明, 馬場俊彦, "1000 個を越えるフォトニック結晶ナノレーザの大規模アレイ集積 (II) -発振特性とさらなる大規模化", 応用物理学会秋季講演会, no. 18p-A3-6, 2013.

[17]　渡部工, 阿部紘士, 西島喜明, 馬場俊彦, “1 万個以上のフォトニック結晶ナノレーザアレイ集積”, 応用物理学会春季講演会, no. 17a-PA1-11, 2014.

[18]　阿部紘士, 馬場俊彦, “フォトニック結晶ナノレーザアレイを用いた 2 次元センサの屈折率分解能の改善”, 応用物理学会春季講演会, no. 18a-E16-8, 2014.

[19]　阿部紘士, 大多哲史, 竹村泰司, 馬場俊彦, “フォトニック結晶ナノレーザアレイを用いた細胞の移動に伴う接着分布の観察”, 応用物理学会秋季講演会, no. 19a-A2-5, 2014.

[20]　馬場俊彦, 羽中田祥司, 渡部工, 高橋大智, 古田裕樹, 渡邊敬介, 阿部紘士, 岸洋次, 酒本真衣, 北翔太, “GaInAsP 半導体デバイスを用いたバイオセンシング／イメージング”, 電子情報通信学会光エレクトロニクス研究会, 2015 (招待講演).

[21]　阿部紘士, 大多哲史, 竹村泰司, 馬場俊彦, "発振波長を整列させたフォトニック結晶ナノレーザアレイによる細胞イメージング速度の改善", 応用物理学会秋季講演会, no. 15p-2B-11, 2015.